

INVERTED ORGANIC ELECTRONIC AND OPTOELECTRONIC DEVICES

By

CEPHAS E. SMALL

A DISSERTATION PRESENTED TO THE GRADUATE SCHOOL
OF THE UNIVERSITY OF FLORIDA IN PARTIAL FULFILLMENT
OF THE REQUIREMENTS FOR THE DEGREE OF
DOCTOR OF PHILOSOPHY

UNIVERSITY OF FLORIDA

2012

© 2012 Cephas E. Small

To my parents

ACKNOWLEDGMENTS

First of all, I give all praise to my Lord and Savior, Jesus Christ, who has guided my life and has continually opened doors of opportunity for me to walk through. I continue to put Him first and look forward to the new things that He will do in my life.

There are a number of people who I must thank for their contributions to my graduate studies and to this dissertation work. It starts with my PhD advisor, Dr. Franky So. From the very beginning, Dr. So showed a willingness and a desire to have me join his research group. When I joined the group in 2006, I was this energetic, enthusiastic graduate student that knew nothing about organic electronics. Believing that I could be successful, Dr. So set high expectations for my work and was patient with me throughout the entire process. He has showed me, through his own example, the level of hard work, focus, and dedication that it takes to contribute to the research work at a high level. I have become a better researcher and am better equipped to have success in the next stage in my career as a result of his guidance. Although my years working with him has been very challenging, I am grateful for everything he has taught me. I would also like to thank Dr. Norton, Dr. Pearton, Dr. Xue, and Dr. Rinzler for serving on my committee and providing feedback concerning my research.

I would also like to acknowledge several of the past and present members of Dr. So's research group: Dr. Kaushik Roy Choudury, Dr. Jegadesan Subbiah, Dr. DoYoung Kim, Dr. Stephen Tsang, Dr. Leo Cheung, Dr. Neetu Chopra, Dr. Jaewon Lee, Dr. Dong Woo Song, Dr. Galileo Sarasqueta, Alok Gupta, Frederick Steffy, Mikail Shaikh, Nikhil Bhandari, Pieter De Somer, Verena Giese, Song Chen, Michael Hartel, Jesse Manders, Tzung Han Lai, Sujin Baek, Lordania Constantinou, and Eric Klump. I thank these wonderful people for not only contributing to my research work, but also serving as an

extended family that has contributed to my growth and development. In addition, I thank Dr. Mikhail Noginov, Dr. Carl Bonner, Dr. Suely Black, and the rest of the faculty and staff at Norfolk State University's Center for Materials Research. I thank them for giving me the opportunity to conduct basic research for the first time. It was at NSU that I discovered my passion for research and science.

Lastly, I thank my family, who has continuously supported me in my academic endeavors and has helped me to stay grounded in my faith. Their love was all the motivation I would need to finish what I started.

TABLE OF CONTENTS

	<u>page</u>
ACKNOWLEDGMENTS.....	4
LIST OF TABLES.....	8
LIST OF FIGURES.....	9
ABSTRACT	13
CHAPTER	
1 INTRODUCTION	15
1.1 Organic Semiconductors.....	15
1.1.1 Classes of Organic Semiconductors.....	15
1.1.2 Advantages and Disadvantages	16
1.2 Charge Transport and Injection in Organic Semiconductors.....	18
1.2.1 Charge Transport	18
1.2.2 Charge Injection	19
1.3 Inverted Organic Electronic Devices	20
1.3.1 Organic Light-Emitting Diodes (OLEDs)	20
1.3.2 Organic Photovoltaics (OPVs)	21
1.4 Dissertation Outline.....	22
2 ELECTRON ACCEPTING INTERLAYERS AS SELECTIVE p-CONTACTS FOR INVERTED ORGANIC ELECTRONIC DEVICES	27
2.1 Introductory Remarks.....	27
2.2 Experimental Details	31
2.2.1 Device Fabrication.....	31
2.2.2 Device Characterization	32
2.3 Results and Discussions.....	34
2.3.1 J-V Characterization	34
2.3.2 DI-SCLC Transient Measurement	35
2.3.3 MoO ₃ -doped NPB Injection Layer For Improved Hole Injection	36
2.4 Concluding Remarks.....	39
3 INTRODUCTION TO ORGANIC PHOTOVOLTAIC CELLS	50
3.1 Overview and History.....	50
3.2 Principles of Operation.....	53
3.3 Photovoltaic Cell Characterization	54
3.3.1 Current-Voltage Measurement	55
3.3.2 Spectral Response Measurement	55

3.4 Progress in Organic Photovoltaic Cell Performance	57
3.4.1 Novel Conjugated Polymers for OPVs.....	58
3.4.2 Inverted Device Geometry.....	60
4 HIGH EFFICIENCY INVERTED POLYMER PHOTOVOLTAIC CELLS.....	67
4.1 Introductory Remarks.....	67
4.2 Experimental Details	70
4.2.1 Device Fabrication.....	70
4.2.2 Device Characterization	71
4.3 Results and Discussions.....	71
4.3.1 ZnO-PVP Nanocomposite Film Characterization	71
4.3.2 Inverted Polymer Photovoltaic Cell with ZnO-PVP Nanocomposite ETL	74
4.3 Concluding Remarks.....	78
5 LOSS MECHANISMS IN THICK-FILM LOW-BANDAP POLYMER SOLAR CELLS	89
5.1 Introductory Remarks.....	89
5.2 Experimental Details	92
5.2.1 Device Fabrication.....	92
5.2.2 Device Characterization	93
5.3 Results and Discussions.....	93
5.3.1 PDTG-TPD:PC ₇₁ BM Solar Cell Performance	93
5.3.2 Loss Mechanisms in Thick-Film PDTG-TPD:PC ₇₁ BM Solar Cells	97
5.4 Concluding Remarks.....	106
6 CONCLUSIONS	120
LIST OF REFERENCES	122
BIOGRAPHICAL SKETCH.....	136

LIST OF TABLES

<u>Table</u>		<u>page</u>
4-1	Average solar cell performance for inverted PDTG-TPD:PC ₇₁ BM devices with 5, 10, 20, or 30-minute UV-ozone treated ZnO-PVP composite ETLs under initial AM 1.5G solar illumination.....	79
5-1	Averaged solar cell performance for inverted PDTG-TPD:PC ₇₁ BM devices with various active layer thickness under initial AM 1.5G solar illumination.....	107
5-2	Averaged solar cell performance for inverted P3HT:PC ₆₁ BM devices with various active layer thickness under initial AM 1.5G solar illumination.....	107

LIST OF FIGURES

<u>Figure</u>		<u>page</u>
1-1	Number of scientific publications contributing to the topics "organic photovoltaics" and "organic light emitting diodes".	24
1-2	Large-scale roll-to-roll manufacturing process for flexible organic electronic devices.	24
1-3	Schematic energy diagram of a metal-organic semiconductor interface with an interface dipole formed at the interface.	25
1-4	Commercially available products based high-resolution OLED display technology.	25
1-5	Comparison between a bottom-emitting and top-emitting OLED with a conventional or inverted structure.....	26
2-1	Molecular structure of electron acceptors and conducting polymers used as injection layers in conventional OLEDs.	41
2-2	Energy level diagram at the NPB/HAT-CN/Au interface.	42
2-3	Schematic cross-section view of NPB single-carrier devices fabricated in this study.....	43
2-4	An ideal DI-SCLC transient current response for a trap-free organic semiconductor.	43
2-5	Current density and injection efficiency vs. electric field for conventional and inverted NPB hole-only devices using MoO ₃ or HAT-CN as HIL.	44
2-6	DI-current density transients measured at various applied voltages using MoO ₃ as HIL.....	45
2-7	DI-current density transients measured at various applied voltages using HAT-CN as HIL.....	46
2-8	Injection efficiency, η , extracted from DI-SCLC transient current measurements vs. electric field for normal and inverted NPB single-carrier devices with either MoO ₃ or HAT-CN as injection layer.....	47
2-9	Hole mobility (μ_{DI}) as a function of electric field ($F^{1/2}$) for normal and inverted NPB hole-only devices with either MoO ₃ or HAT-CN injection layer.....	47

2-10	Current density and injection efficiency plots for conventional NPB hole-only devices with either a neat MoO ₃ or MoO ₃ -doped NPB HIL of varying doping concentration (1, 5, 10 mol%).....	48
2-11	Current density vs. applied electric field for MoO ₃ -doped and HAT-CN-doped NPB single-carrier devices.	49
2-12	Current density vs. electric field for normal NPB single-carrier devices with either ITO or Au anode.	49
3-1	Schematic illustrations for various solution processing methods used in the fabrication of large-scale and laboratory-scale polymer photovoltaic cells.	62
3-2	Schematic diagram illustrating an organic donor-acceptor heterojunction, as well as the bilayer and bulk heterojunction concepts.	62
3-3	Typical J-V characteristics for a photovoltaic cell tested in the dark (J_D) and under illumination (J_L).	63
3-4	Chemical structure for standard electron donor and acceptor materials used in the fabrication of organic photovoltaic cells.	64
3-5	Schematic illustration showing the molecular orbital hybridization for a donor-acceptor (D-A) copolymer and the resulting reduction in the effective bandgap.	65
3-6	Chemical structure for state-of-the-art donor-acceptor copolymers used for high efficiency polymer photovoltaic cells.	65
3-7	Normal vs. inverted device architectures for organic photovoltaic cells.	66
4-1	The normal and inverted device geometries for P3HT:PCBM solar cells.	79
4-2	An illustration of the process and the six processing steps employed during fabrication of the R2R coated modules.	80
4-3	AFM image (measuring $5 \times 5 \mu\text{m}^2$) of a knife-over-edge coated ZnO nanoparticle film used in the fabrication of large-scale R2R-processed modules.	80
4-4	Tapping mode AFM images for as-prepared and 10-min UV-ozone treated ZnO-PVP nanocomposite films.	81
4-5	Tapping-mode AFM phase images for ZnO-PVP nanocomposite films before and after UV-ozone treatment (5 μm scale size).	82
4-6	X-ray photoemission spectra (XPS) for the as-prepared and 10-minute UV-ozone treated ZnO-PVP nanocomposite films.	83

4-7	UV-visible-NIR transmission spectra for the as-prepared and 10-minute UV-ozone treated ZnO-PVP nanocomposite films.....	84
4-8	Photo <i>J-V</i> characteristics for inverted PDTG-TPD:PC ₇₁ BM solar cells highlighting the effect of prolonged light soaking on device performance under AM 1.5G solar illumination at 100 mW cm ⁻²	84
4-9	Photo <i>J-V</i> characteristics and EQE spectra for inverted PDTG-TPD:PC ₇₁ BM solar cells with UV-ozone treated ZnO-PVP nanocomposite ETL for various treatment times.....	85
4-10	Dark <i>J-V</i> characteristics for inverted PDTG-TPD:PC ₇₁ BM solar cells with UV-ozone treated ZnO-PVP nanocomposite ETL measured as-is and after being light soaked using either a 600 nm or 350 nm band-pass filter.	86
4-11	Certified <i>I-V</i> characteristics for an inverted PDTG-TPD:PC ₇₁ BM solar cell with 10-minute UV-ozone treated ZnO-PVP nanocomposite ETL. The device was certified by NEWPORT Corporation.	87
4-12	Solar cell parameters versus time for encapsulated inverted PDTG-TPD:PC ₇₁ BM with as-prepared and 10-minute UV-ozone treated ZnO-PVP nanocomposite ETLs.....	88
5-1	Device structure for PDTG-TPD:PC ₇₁ BM solar cells, P3HT:PC ₆₁ BM solar cells, and corresponding single-carrier devices studied in this work.....	108
5-2	Photo <i>J-V</i> characteristics and EQE spectra for inverted PDTG-TPD:PC ₇₁ BM solar cells with increasing active layer thickness.	109
5-3	Photo <i>J-V</i> characteristics and EQE spectra for inverted P3HT:PC ₆₁ BM solar cells with increasing active layer thickness.....	110
5-4	Average fill factor and EQE versus active layer thickness for PDTG-TPD:PC ₇₁ BM and P3HT:PC ₆₁ BM solar cells.	111
5-5	Current density times active layer thickness ($J \times L$) versus electric field curves for PDTG-TPD:PC ₇₁ BM hole-only devices with 100 nm and 409 nm-thick layers.....	112
5-6	Field-dependent EQE spectra for PDTG-TPD:PC ₇₁ BM solar cells with increasing active layer thickness.	113
5-7	Normalized photocurrent density (J_L) as a function of internal electric field for inverted PDTG-TPD:PC ₇₁ BM solar cells with increasing active layer thickness.	114
5-8	UV-Vis-NIR spectra and fraction of photons absorbed vs. active layer thickness for PDTG-TPD:PC ₇₁ BM and P3HT:PC ₆₁ BM solar cells.	115

5-9	Normalized J_{ph} - V_{eff} curves for under 100 mW cm ⁻² illumination for the devices studied.....	116
5-10	Light intensity dependence of the photocurrent and fill factor for 105 nm-thick and 409 m-thick PDTG-TPD:PC ₇₁ BM solar cells.....	117
5-11	Calculated number of photons absorbed in the PDTG-TPD:PC ₇₁ BM layer under AM1.5G illumination and photocurrent loss as a function of layer thickness.	118
5-12	The critical active layer thickness corresponding to the onset of SCL photocurrent (L_c) in low bandgap polymer solar cells versus bandgap of the polymer.....	119

Abstract of Dissertation Presented to the Graduate School
of the University of Florida in Partial Fulfillment of the
Requirements for the Degree of Doctor of Philosophy

INVERTED ORGANIC ELECTRONIC AND OPTOELECTRONIC DEVICES

By

Cephas E. Small

December 2012

Chair: Franky So

Major: Materials Science and Engineering

The research and development of organic electronics for commercial application has received much attention due to the unique properties of organic semiconductors and the potential for low-cost high-throughput manufacturing. For improved large-scale processing compatibility and enhanced device stability, an inverted geometry has been employed for devices such as organic light emitting diodes and organic photovoltaic cells. These improvements are attributed to the added flexibility to incorporate more air-stable materials into the inverted device geometry. However, early work on organic electronic devices with an inverted geometry typically showed reduced device performance compared to devices with a conventional structure.

In the case of organic light emitting diodes, inverted devices typically show high operating voltages due to insufficient carrier injection. Here, a method for enhancing hole injection in inverted organic electronic devices is presented. By incorporating an electron accepting interlayer into the inverted device, a substantial enhancement in hole injection efficiency was observed as compared to conventional devices. Through a detailed carrier injection study, it is determined that the injection efficiency

enhancements in the inverted devices are due to enhanced charge transfer at the electron acceptor/organic semiconductor interface.

A similar situation is observed for organic photovoltaic cells, in which devices with an inverted geometry show limited carrier extraction in early studies. In this work, enhanced carrier extraction is demonstrated for inverted polymer solar cells using a surface-modified ZnO-polymer composite electron-transporting layer. The insulating polymer in the composite layer inhibited aggregation of the ZnO nanoparticles, while the surface-modification of the composite interlayer improved the electronic coupling with the photoactive layer. As a result, inverted polymer solar cells with power conversion efficiencies of over 8% were obtained. To further study carrier extraction in inverted polymer solar cells, the active layer thickness dependence of the efficiency was investigated. For devices with active layer thickness < 200 nm, power conversion efficiencies over 8% was obtained. This result is important for demonstrating improved large-scale processing compatibility. Above 200 nm, significant reduction in cell efficiency were observed. A detailed study of the loss processes that contributed to the reduction in efficiency for thick-film devices are presented.

CHAPTER 1 INTRODUCTION

1.1 Organic Semiconductors

Although research focused on the use of organic semiconductors for electronic and optoelectronic application started as a mere academic curiosity, today low-cost commercially-viable technology based on these novel materials have become a reality. Rapid progress in the field of organic electronics and optoelectronics is in large part due to significant research contributions from academia, research laboratories and industry. As an example, the number of scientific publications contributing to the subjects 'organic photovoltaic cells' and 'organic light emitting diodes' by year, which is displayed in Figure 1-1, clearly highlights the significant increase in contributions for these research areas per year. Initially, the interest in organic electronics and optoelectronics was aimed at studying conjugated molecules that exhibited interesting electrical and optical properties. Development of these novel organic semiconductors has continued to be a core focus of the research. This chapter will introduce the reader to organic semiconductors: the different classes of these materials, their properties, and the use of these materials in optoelectronic devices. Lastly, the research scope for this dissertation will be presented.

1.1.1 Classes of Organic Semiconductors

Organic semiconductors can be categorized into two classes: small molecular-weight molecules and conjugated polymers. Small molecules are discrete units with several to a few hundred atoms. Consequently, the molecular weight for these materials are well-defined. Organic small-molecules are typically processed at high vacuum by thermal evaporation/sublimation for thin-film fabrication. By controlling the substrate

heating temperature during processing, amorphous, polycrystalline, and single-crystal small molecule thin films can be produced. Due to their ease of processing and the diverse electrical and optical properties of these materials, organic small molecules have been used as hole-transporting, electron transporting, and photoactive materials in organic thin-film transistors (OTFTs), organic light-emitting diodes (OLEDs) and organic photovoltaics (OPVs).

In contrast to organic small molecules, conjugated polymers have a molecular structure consisting of long chains of repeat units called monomers. The molecular weights for conjugated polymers are typically very large and vary from polymer to polymer. These materials are processed from solution using various processing methods such as spin coating, drop casting, or ink-jet printing. The use of solution processing permits the control of numerous processing conditions that impact the thin-film morphology, such as the choice of solvent and annealing conditions. However, the solution processing of organic layer stacks can be difficult due to the requirement of orthogonal solvents for the organic layers. Controlling the morphology of solution-processed polymer films and developing novel solution-processing procedures for fabricating organic layer stacks is still a subject of ongoing research and is critical for various device applications.

1.1.2 Advantages and Disadvantages

Organic semiconductors, due to their intrinsic properties, has many advantages that are suitable for electronic and optoelectronic applications. For one, organic semiconductors have a low material cost and can be processed using low-cost fabrication methods. For example, high vacuum thermal evaporation of small molecules is a simple process that is more energy efficient than processing methods using for thin-

film inorganic semiconductors, such as sputtering and plasma-enhanced chemical vapor deposition (PECVD). The cost for fabrication is reduced even further when solution processing methods are employed. These low-cost fabrication methods are compatible with large-scale roll-to-roll (R2R) manufacturing on rigid or flexible substrates, allowing organic-based devices to be produced at high throughput. Figure 1-2 shows the large-scale manufacture of flexible organic electronics produced by different parties. Another key advantage to organic semiconductors is the ability to tailor the properties of these material through intelligent chemical modification. This has lead to increased charge carrier mobility in OTFTs, efficient color tuning OLEDs, and enhanced light harvesting in OPVs.

Interestingly, the intrinsic properties of organic semiconductors also introduce a number of disadvantages that hinder the performance of electronic and optoelectronic devices. These materials have much lower carrier mobilities and intrinsic carrier concentrations compared to inorganic semiconductors. Consequently, the device performance of organic electronic and optoelectronic devices becomes limited by the low electrical conductivity of organic semiconductors. Another issue is the inability to obtain high purity levels in organic materials. As a result, a high trap density due to impurities and structural defects is common for organic semiconductors. Lastly, organic materials degrade in ambient condition due to oxidation and exposure to moisture. To produce devices with enhanced stability and lifetime, it becomes necessary to design suitable encapsulation technology. This adds additional complexity to the fabrication of organic electronic devices.

1.2 Charge Transport and Injection in Organic Semiconductors

1.2.1 Charge Transport

The transport of electrons and holes in organic solids can be described by three different models based on either a microscopic or macroscopic view of charge conduction. In the microscopic view, charge carrier hop between adjacent molecules to facilitate charge transport. In this hopping model, the charge hopping rate k is a function of the reorganization energy (λ) and the electron coupling factor (V_{ab})¹. If λ and V_{ab} are known, the diffusion coefficient (D) can be calculated as

$$D = a^2 \cdot k \quad (1-1)$$

where a is the hopping distance. The carrier mobility can then be estimated from the Einstein relation:

$$\mu = \frac{qD}{k_B T} \quad (1-2)$$

where q is electron charge, k_B is the Boltzmann constant, and T is the absolute temperature.

In the macroscopic view, charge conduction occurs by drift via an external field along disordered hopping sites in the organic semiconductor. For this charge transport model, first proposed by Poole and Frenkel, the field-dependent carrier mobility is given as

$$\mu = \mu_0 \exp(\beta_{PF} \sqrt{F}) \quad (1-3)$$

where $\beta_{PF} = (q^3 / \pi \epsilon)^{1/2}$ is the Poole-Frenkel slope, μ_0 is the zero field mobility, F is the electric field, and ϵ is the dielectric constant. The Poole-Frenkel model has been widely used to experimentally determine carrier mobilities in organic semiconductors and is

employed in Chapter 2 to quantify carrier mobility for the hole transporting materials studied in that work.

Another charge transport model worth mentioning is the Gaussian disorder model (GDM), which assumes that the transport energy states in the organic semiconductor have a Gaussian distribution. Since the charge hopping in this model is field-assisted and thermally activated in the disordered system, the carrier mobility is a function of electric field, temperature, and energetic and positional disorder². The energetic disorder can be conceptualized as the width of the Gaussian distribution, while the positional disorder is the geometric randomness caused by structural defects³.

1.2.2 Charge Injection

Figure 1-3 shows the energy diagram for a metal-organic semiconductor interface based on the Mott-Schottky model⁴. When an organic semiconductor is in contact with a metal, an energy barrier is formed at the organic semiconductor-metal interface. The energy barriers for electron and hole injection (ϕ_e , ϕ_h) are determined by the electron affinity (A_e), the ionization potential (I_p), and the vacuum level shift due to the formation of an interface dipole (Δ):

$$\phi_e = \Phi_m - A_e - \Delta \quad (1-4)$$

$$\phi_h = I_p - \Phi_m + \Delta \quad (1-5)$$

where Φ_m is the metal work function. Reducing the electron and hole energy barriers to carrier injection is critically important to the efficient operation of OLEDs. However, this can be a challenge since the work function of the metal electrode typically does not match the transport level of interest for the organic semiconductor. Novel approaches for reducing the energy barrier include introducing interlayers between the metal and

the organic semiconductor to modify the interface energetics, or introducing electron accepting/donating atoms or molecules into the organic semiconductor to dope the interface. These approaches will be expounded upon in Chapter 2.

1.3 Inverted Organic Electronic Devices

1.3.1 Organic Light-Emitting Diodes (OLEDs)

The first demonstration of electroluminescence from an organic heterojunction was observed in the work by Tang and coworkers in 1987⁵. Since that discovery, OLEDs have become a commercially viable technology for lighting and display applications.

OLEDs have the following advantages for these applications: area-emission, high electron to photon conversion efficiency, wide viewing angle, low operating voltage, fast switching, vivid colors, light weight, small thickness, color tunability, and dimmability⁶.

Examples of commercial products based on OLED technology is shown in Figure 1-4. Simply put, an OLED is an electroluminescent device in which the emitting and carrier transporting layers are organic semiconductors. Most polymer LEDs consist of a single light-emitting layer, while OLEDs based on small molecules contain a stack of organic thin films. In either case, the organic layer(s) are sandwiched between two electrodes. When a bias is applied to the electrodes, carriers are injected into the emitting layer and recombine to form an exciton (electron-hole pair). Light is emitted from this photoactive layer when the exciton undergoes radiative decay to the ground state. To efficiently produce light, efficient OLEDs require balanced carrier injection and transport. As a result, conventional OLEDs are designed to ensure efficient carrier injection and balanced charge transport. These devices consist of the following: (i) injection layers, which ensure efficient carrier injection to the organic layers; (ii) electron and hole transport layers, which selectively transports the injected charge carriers to the emitting

layers; (iii) blocking layers, which confine carriers and excitons in the emitting layer; and (iv) an emitting layer⁷⁻¹⁰. Figure 1-5 provides a schematic diagram showing the conventional geometry for a bottom-emitting and top-emitting OLED.

In addition to enhancing the performance of OLEDs by optimizing carrier injection and transport, a developing trend in OLED research is to employ an inverted geometry for the device. An example of the inverted device geometry for a top-emitting OLED is shown in Figure 1-5. The inverted device geometry greatly improves the device stability and eliminates the need for expensive encapsulation technologies. In this geometry, the air-stable high work function anode is moved to the top of the device and is coupled with an air-stable hole injection layer. For the bottom cathode, air-stable electron injection/transporting materials such as n-type metal oxides and novel polyfluorenes provide efficient electron injection from an indium tin oxide (ITO) electrode¹¹⁻¹⁵. In addition to enhanced stability, the inverted device geometry is preferential for active matrix display applications since low cost display driver circuits are based on n-channel a-Si TFT technology⁶. The main problem with inverted OLED devices is their high drive voltage compared to conventional OLEDs due to inefficient carrier injection⁶.

1.3.2 Organic Photovoltaics (OPVs)

In contrast to the rapid progress observed in OLED development, progress in organic photovoltaics (OPVs) has been somewhat slower. Despite the record efficiencies being reported in the literature for laboratory-scale photovoltaic cells, much research efforts are still required before the technology will be commercially viable. The main priorities for OPV research include increasing the device efficiency, extending the device lifetime to over 10 years, and developing a greater expertise in the manufacturing of large-scale roll-to-roll (R2R) processed devices. Consequently,

researchers worldwide have attempted to enhance cell efficiency through employing novel material design and device concepts. Furthermore, improving device stability by developing more effective encapsulation technology and investigating the issues involved in manufacturing large-scale OPV modules have become a focus of the work. Interestingly, employing an inverted device geometry for OPV cells has lead to enhanced cell efficiency, increased device stability, and improved R2R processing compatibility. A more detailed introduction to organic photovoltaic cells will be provided in Chapter 4.

1.4 Dissertation Outline

There are two main topics presented in this dissertation. First, a method for enhancing carrier injection in inverted organic electronic devices is presented. This result is of critical importance for OLEDs, since reducing the drive voltage of inverted devices is required for display applications. In the second, the factors affecting carrier extraction are determined for inverted polymer photovoltaic cells. In Chapter 1, the reader is presented a general introduction to organic electronics. This chapter describes the properties of organic semiconductors, discusses models used to describe charge carrier transport and injection in these materials, and highlights the motivation behind using the inverted device geometry for organic electronic devices. In Chapter 2, a detailed study of carrier injection in inverted organic electronic devices using electron accepting interlayers is presented. In addition to demonstrating ohmic hole injection in inverted devices, the origin of this enhanced hole injection is experimentally investigated.

The subsequent chapters of this dissertation focuses on inverted organic photovoltaic cells. Chapter 3 provides an introduction to organic photovoltaics,

describing the history, operating principles, and experimental methods used to characterize photovoltaic cells. Furthermore, recent process in this research field is discussed, including the use of the inverted device geometry. In Chapter 4, high efficiency inverted polymer photovoltaic cells are demonstrated. By incorporating a ZnO-polymer composite film as the electron transporting layer, enhanced charge collection is observed in the devices. Using the same device geometry, the thickness dependence of the efficiency is investigated in Chapter 5. The loss processes responsible for limited device performance in inverted polymer solar cells with thick active layer are investigated. A theoretical model designed to help explain the role that space-charge effects play in increasing photocurrent loss is presented. Finally, Chapter 6 summarizes the results of this work and provides a brief outlook on future work.

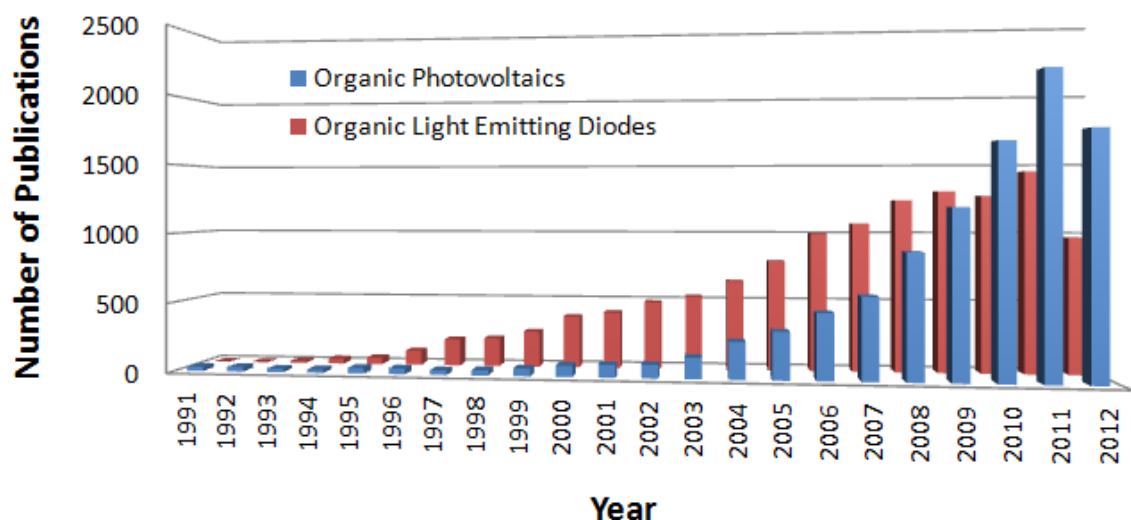


Figure 1-1. Number of scientific publications contributing to the topics "organic photovoltaics" and "organic light emitting diodes". Search done through ISI, Web of Science database.

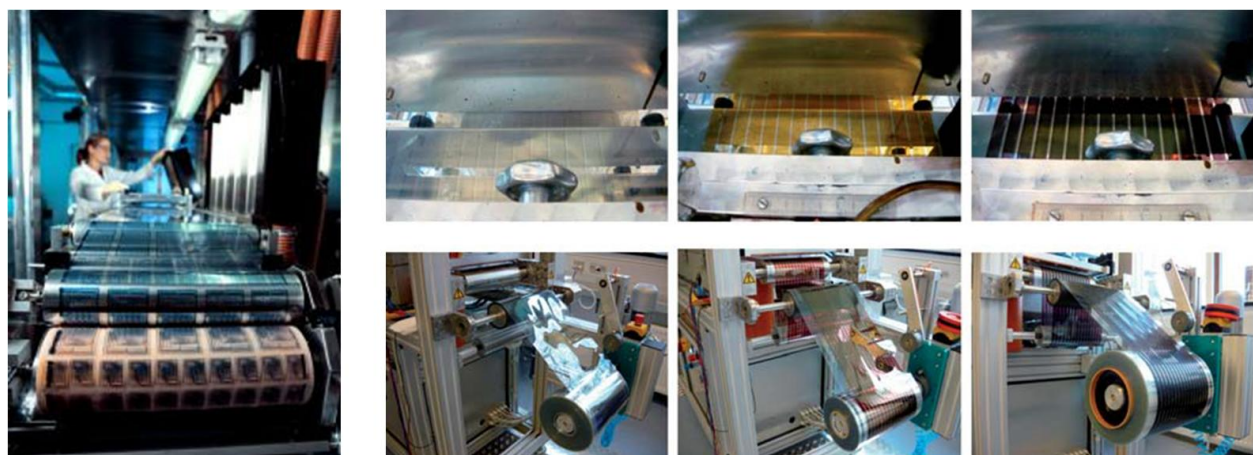


Figure 1-2. Large-scale roll-to-roll manufacturing process for flexible organic electronic devices^{16,17}.

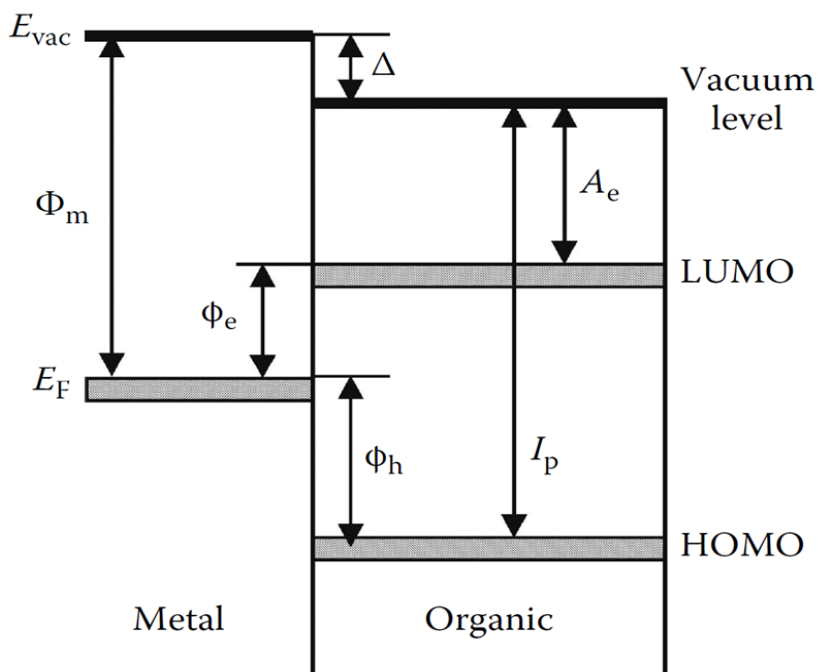


Figure 1-3. Schematic energy diagram of a metal-organic semiconductor interface with an interface dipole formed at the interface¹.



Figure 1-4. Commercially available products based high-resolution OLED display technology¹⁸.

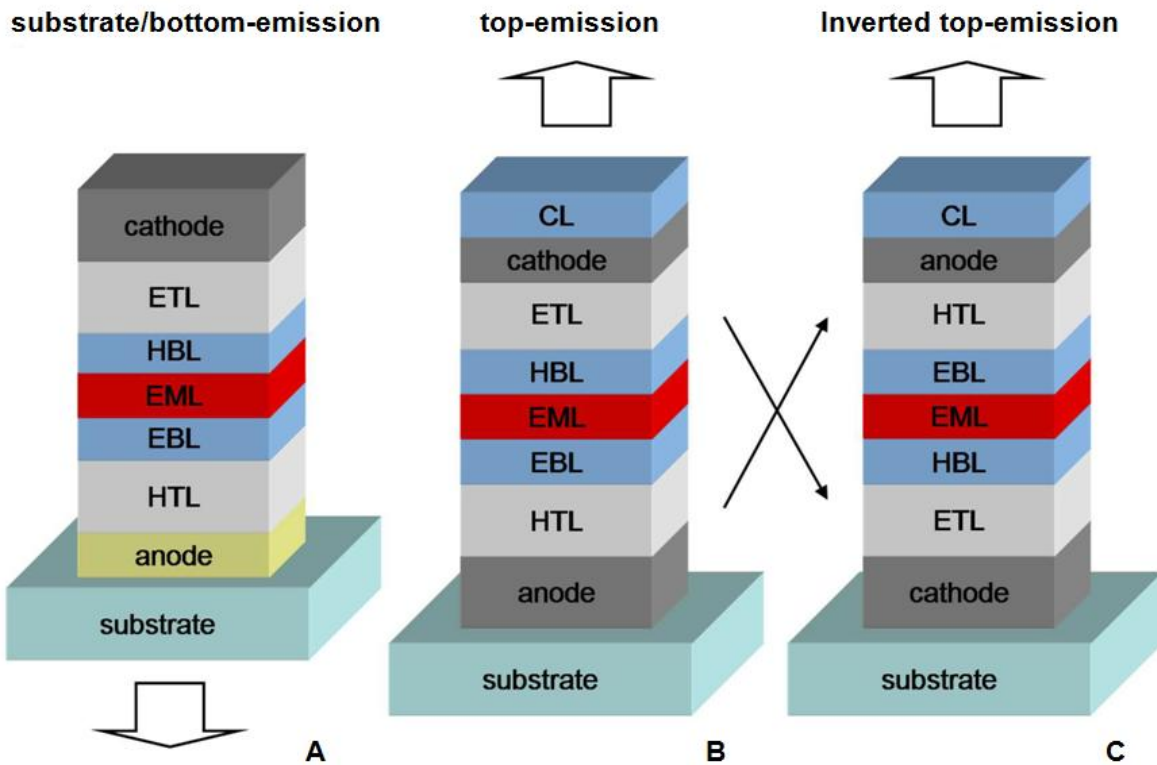


Figure 1-5. Comparison between a bottom-emitting and top-emitting OLED with a conventional or inverted structure. A) Bottom-emitting OLED with a conventional structure. B) Top-emitting OLED with a conventional structure. C) Top-emitting OLED with an inverted structure. HTL = hole transport layer, EBL = electron blocking layer, EML = emission layer, HBL = hole blocking layer, ETL = electron transport layer, CL = capping layer⁶.

CHAPTER 2

ELECTRON ACCEPTING INTERLAYERS AS SELECTIVE P-CONTACTS FOR INVERTED ORGANIC ELECTRONIC DEVICES

2.1 Introductory Remarks

Research aimed at optimizing the performance of organic light-emitting diodes (OLEDs) has received much attention in recent years due to the enormous potential of the technology in flat panel display and solid state lighting applications¹⁹. A key requirement to demonstrating OLEDs with efficient operation is to optimize carrier injection from the electrodes to the active emitting layer^{20,21}. As discussed in Chapter 1, this requirement is due to the low intrinsic carrier concentration of organic semiconductors and thus the need to reduce the device operating voltage. Optimizing carrier injection is not a simple task, especially since OLEDs utilize wide band-gap materials whose energy levels do not match the work-function of the electrodes. The work function mismatch is especially a problem for hole injection because the work function of transparent electrodes such as indium tin oxide (ITO) is less than 5.0 eV while the highest occupied molecular orbital (HOMO) energies of wide band-gap hole transporting materials commonly used in OLEDs are typically 5.5 eV or higher, resulting in low hole injection efficiencies.

To overcome this limitation, interlayers are often incorporated into the device to enhance hole injection. Figure 2-1 shows the molecular structure for materials commonly used as hole injection layers in conventional OLEDs. In general, these materials can be grouped into two categories. One class of materials used for the hole injecting interlayer is conducting polymers, such as poly(3,4-ethylene-dioxythiophene) poly(styrenesulfonate) (PEDOT:PSS)²²⁻²⁴. Although the use of PEDOT:PSS as a hole injection layer (HIL) has been quite popular in small-molecule and polymer OLED

research, its work-function of 5.0 eV is not adequate to provide optimum hole injection into wide band-gap materials with a deep HOMO energy²⁵. Another class of materials used as interlayer is strong electron acceptors. These materials can facilitate enhanced hole injection in OLEDs²⁶. Unlike conducting polymer HILs, electron accepting interlayers modify the energy levels of the anode and wide band-gap hole transporting materials when inserted between these two layers. Previously reported ultraviolet photoemission spectroscopy (UPS) results showed that the electron accepting interlayer was responsible for both the large vacuum level shift in the anode, whether indium tin oxide (ITO) or Au, and the observed band-bending in the HOMO level of the hole-transporting layer²⁷⁻³⁰. As an illustration, Figure 2-2 shows the schematic energy level alignment of the Au/HAT-CN/NPB interface based on *in situ* ultraviolet photoemission spectroscopy (UPS) measurements. The strong band-bending of the hole-transporting layer's HOMO level is indicative that the Fermi level moves down and pins at a certain position as typical for *p*-doping. The use of electron acceptors for controlled *p*-doping in amorphous hole-transporting materials employed in high efficiency OLEDs has been well studied³¹⁻³⁷. For example, strong *p*-type doping has also been observed when MoO₃ was used as a dopant in hole transporters with a deep HOMO level³⁶. Due to their ability to modify the energy levels of the anode and the wide band-gap hole transporting layers, these electron acceptors can serve as efficient hole injectors for wide band-gap materials with a deep HOMO level.

Despite the use of conducting polymers or electron acceptors as interlayers for improved carrier injection in organic devices, truly ohmic hole injection has rarely been reported. When the hole injection contact is ohmic, the carrier transport is limited by the

bulk of the materials rather than the injection contact. As a result of the ohmic injection, the carrier transport is space-charge limited³². The determination between bulk-limited versus injection-limited transport is made by calculating the carrier injection efficiency, which is the ratio between the measured steady-state current density of the device and the theoretical space-charge-limited current density given by the Mott-Gurney Law³⁸. Even for conventional bottom-injection contact hole-only devices with PEDOT:PSS as an interlayer, injection-limited transport and low injection efficiency values ranging from 30 to 60% have been reported²⁵. Additional studies featuring MoO₃ as an electron accepting interlayers have reported even lower injection efficiencies for similar single-carrier devices³⁹. Recently, two novel approaches have been demonstrated for achieving ohmic hole injection in OLEDs. One approach is to utilize a composite HIL consisting of a mixture of conducting polymers with different work functions and graphene for ohmic hole injection in flexible OLEDs⁴⁰. The other approach for achieving ohmic hole injection consists of using electron accepting interlayers in OLEDs with an inverted architecture, with a substantial enhancement in current density being observed in the device when the bottom hole injection contact using PEDOT:PSS interlayer is replaced by a top hole injection contact using MoO₃ interlayer⁴¹. In these inverted devices, the electron accepting interlayer is deposited on top of the hole transporting layer to form the top hole injection contact. Using this approach, optimized hole injection into wide band-gap materials can be achieved. However, the origin of this enhancement is not understood.

The mechanism of enhanced hole injection in inverted organic devices with different electron accepting interlayers is investigated in this chapter. The results

presented here suggest a generalized behavior of the electron acceptors MoO₃ and HAT-CN to provide enhanced hole injection in devices with an inverted architecture. A widely used amorphous hole transporting material *N,N'*-di(naphthalene-1-yl)-*N,N'*-diphenyl-benzidine (NPB), was used for this study⁴²⁻⁴⁴. Current-voltage (*J-V*) and space-charge-limited dark injection (DI-SCLC) transient measurements were used to characterize the hole injection efficiency in the normal and inverted single-carrier devices. It was found that HAT-CN was a superior hole injector compared with MoO₃ as a hole injection interlayer used in both normal and inverted devices. Furthermore, inverted devices with a top hole injection contact showed a higher injection efficiency compared to the normal devices with a bottom injection contact. For inverted devices with top-contact HAT-CN interlayer truly ohmic hole injection was demonstrated, with an injection efficiency close to 100% being obtained. These results suggest that a better charge transfer at the electron acceptor/NPB interface is formed in the inverted device architecture. In this work, the term ‘charge transfer’ refers to the transfer of electrons from the HOMO of NPB to the lowest unoccupied molecular orbital (LUMO) of the electron acceptor as discussed in previous photoemission spectroscopy results for MoO₃ and HAT-CN²⁷⁻³⁰. To further support our charge transfer model, we fabricated normal NPB single-carrier devices that consisted of either a neat MoO₃ HIL or a MoO₃-doped NPB injection layer. Not only did we observe enhanced hole injection for devices with a MoO₃-doped NPB injection layer, but we also found that the injection efficiency can be tuned by increasing the MoO₃ doping concentration. Lastly, to understand why HAT-CN was the better hole injector compared to MoO₃, we fabricated hole-only devices with a *p*-doped NPB interlayer using both electron acceptors as dopants. The

doping effect obtained using a fixed doping concentration of HAT-CN or MoO₃ in NPB allowed us to characterize the degree of charge transfer between the electron acceptors and NPB. Since stronger p-type doping was observed when HAT-CN was used as the dopant compared with MoO₃, we confirmed that HAT-CN provides more efficient charge transfer with NPB compared to MoO₃.

2.2 Experimental Details

2.2.1 Device Fabrication

Hole-only devices were fabricated by thermal evaporation of the organic small-molecule materials and MoO₃. MoO₃ (99.999% purity) and HAT-CN were used for this study. Figure 2-3 shows a schematic diagram of the devices fabricated in this study. For the *J-V* and DI-SCLC transient measurements, the following hole-only devices were fabricated: (a) ITO/electron accepting HIL (10 nm)/NPB (1.5 μm)/Au (normal device) and (b) ITO/NPB (1.5 μm)/electron accepting HIL (10 nm)/Au (inverted device). Both devices were fabricated in the same thermal evaporation run for ease of comparison. Prior to film deposition, pre-patterned ITO-coated glass substrates were cleaned by sequential baths of de-ionized water, acetone, and isopropanol. The substrates were then exposed to UV-ozone treatment for 15 minutes. The electron accepting HILs and NPB were thermally evaporated at a base pressure ~10⁻⁶ Torr onto the substrates at rates of 0.05 and 0.5 nm/s, respectively. The high work function (WF) metal Au was used as the electron blocking cathode in the normal device and as the anode in the inverted device. It should be noted that UV-ozone treated ITO (WF ~ 4.7 eV) served as an effective electron blocking cathode in the inverted device. To compare the quality of hole injection for a neat MoO₃ hole injection layer versus a MoO₃-doped NPB hole injection layer, the following hole-only devices were fabricated simultaneously: (c)

ITO/MoO₃ (10 nm)/NPB (1.8 μm)/Au, and (d) ITO/NPB:MoO₃ (10 nm, 1-10 mol%)/NPB (1.8 μm)/Au. For *p*-doped NPB single carrier devices, the doping concentration (10 mol%) was held fixed for both MoO₃–doped and HAT-CN–doped NPB films.

2.2.2 Device Characterization

Current-Voltage (*J*-*V*) Measurement: The hole injection behavior of NPB single-carrier devices with electron accepting HILs were analyzed by *J*-*V* characterization. The *J*-*V* characteristics were measured using a test-fixture connected to a Keithley 4200-SCS, which provided a computer-controlled source measuring unit (SMU) as the steady-state voltage source and current measuring device. Assuming that the organic material is trap free with an ohmic injection contact, the steady-state current should follow the space-charge-limited current (*J*_{SCL}) as follows⁴⁵:

$$J_{SCL} = \frac{9}{8} \mu_0 \epsilon_0 \epsilon_r \exp(0.89\beta\sqrt{F}) \frac{F^2}{d} \quad (2-1)$$

where μ_0 is the zero-field mobility, ϵ_0 is the vacuum permittivity, ϵ_r is the relative permittivity, and $F = V/d$ is the applied electric field. The Poole-Frenkel slope β is the field-dependent mobility coefficient. Both $\beta = 1.3 \times 10^{-3}$ (cm/V)^{1/2} and $\mu_0 = 2.7 \times 10^{-4}$ cm²/V s were obtained from independent time-of-flight (TOF) measurements reported in the literature³⁹. The carrier injection efficiency, η , can then be calculated by the following equation³⁸:

$$\eta = J_{INJ}/J_{SCL} \quad (2-2)$$

where J_{INJ} is the measured steady-state current density. If the experimentally measured current density agrees with the ideal J_{SCL} such that $\eta \approx 1$, then the injection contact is ohmic. However, the experimental *J*-*V* curves often deviate from J_{SCL} , signifying that J_{INJ} is injection limited. For a non-ohmic contact, the carrier injection can be described by

the Richardson–Schottky model of thermionic emission, i.e. the charge carriers are injected into the organic semiconductor if and only if they have enough thermal energy to overcome the Schottky barrier (ϕ)^{46,47}.

DI-SCLC Measurement: DI-SCLC transient measurement is a well-known technique for characterizing the carrier mobility and carrier injection in organic semiconductors⁴⁸⁻⁵⁰. For the DI-SCLC measurements taken in this work, a pulse generator [HP model 214B] was used to inject holes into the NPB single-carrier devices by application of a rectangular voltage pulse. A digital oscilloscope captured the voltage across a current-sensing resistor that was connected in series to the samples and the corresponding current density was calculated following the measurement. The large thickness for the NPB layer (1.5 – 1.8 μm) ensured that the *RC* decay did not dominate the measured current transient, making the transit time easy to determine experimentally. Figure 2-4 shows the ideal DI-SCLC transient current response for a trap-free organic semiconductor. The ideal transient shows a well-defined maximum at τ_{DI} , which is the arrival time of the leading front of the injected carriers transporting to the non-injecting electrode. Two critical parameters can be extracted directly from the DI-SCLC transient current response. First, since the position of τ_{DI} is related to the space-charge-free transient time by $\tau_{DI} = 0.787 \tau_{tr}$, the carrier mobility can be calculated as follows⁵¹:

$$\mu_{DI} = \frac{0.787d^2}{\tau_{DI} \cdot V} \quad (3)$$

where d is the thickness of the organic layer and V is the voltage applied to the sample. Second, the carrier injection efficiency can be extracted from the DI-SCLC transient by

calculating the ratio between the measured peak transient current density and the theoretical peak current density, which is ~ 1.21 times the space-charge limited current density. Therefore, the carrier injection efficiency is given as^{45,52}:

$$\eta = J_{DI}/1.21J_{SCL} \quad (4)$$

where J_{DI} is the peak transient current density at $t = \tau_{DI}$.

2.3 Results and Discussions

2.3.1 J-V Characterization

Figure 2-5 shows the current density vs. electric field characteristics for the normal and inverted NPB hole-only devices with either MoO₃ or HAT-CN as the HIL. The solid line shown in the figure represents the theoretical J_{SCL} calculated from Equation 1. Two conclusions can be drawn directly from these results. First, the inverted NPB hole-only devices showed enhanced current densities compared to the devices with the normal architecture with MoO₃ or HAT-CN as the HIL. Second, the devices with HAT-CN HIL showed a significantly larger current density than similar devices using MoO₃ as the HIL. It should be noted that the inverted NPB device with HAT-CN HIL was the only device to show a good agreement with the theoretical J_{SCL} curve. The injection efficiency, η , was then calculated from the J-V characteristics using Equation 2 and plotted as a function of electric field for the devices (see Figure 2-5). A marked improvement in hole injection efficiencies was observed for the inverted devices with either a MoO₃ or HAT-CN HIL compared to the normal device. The injection efficiency for inverted devices with HAT-CN top-contact HIL is near unity, meaning that the injection contact is truly ohmic. These results show that improved hole injection in

inverted NPB hole-only devices using MoO₃ or HAT-CN as HIL is a generalized behavior.

2.3.2 DI-SCLC Transient Measurement

Analysis of the DI-SCLC transient data provides in-depth understanding of the charge injection processes^{38,39}. Figure 2-6 shows the DI-SCLC transients with increasing applied bias for normal and inverted NPB single carrier devices with MoO₃ injection layer. The measured transients show a well-defined maximum at τ_{Dl} followed by decay to a saturation value. The shift in τ_{Dl} to shorter times with increasing applied bias indicates that the hole mobility in NPB is field dependent²⁵. Larger current density values can be observed in the inverted hole-only devices compared to normal devices with the same film thickness. A similar result was obtained from DI-SCLC transients of normal and inverted NPB single carrier devices with HAT-CN HIL, shown in Figure 2-7. These devices showed larger transient current densities compared to the corresponding devices with MoO₃ HIL, which is consistent with the J-V measurements highlighted in Section 2.3.1. Furthermore, to confirm that HAT-CN HIL provides ohmic hole injection in inverted NPB single-carrier devices, the carrier injection efficiencies were calculated for the same devices based on the measured DI-SCLC transients using Equation 4. This result is shown in Figure 2-8. The field-dependent injection efficiencies based on the DI-SCLC transients are in good agreement with the results showed in Figure 2-5, with ohmic hole injection ($\eta \approx 1$) being obtained for the inverted NPB devices with top-contact HAT-CN HIL.

Analyzing all of the normal and inverted NPB hole-only devices under the same applied field revealed a difference in the measured τ_{Dl} . DI-SCLC transient

measurements assume the injection contact for the device is truly ohmic. If the injection contact is injection limited, then the carrier mobility calculated from the transients (μ_{Dl}) will be limited since the transient time corresponding to the leading front charge (τ_{Dl}) will be delayed due to inefficient charge injection. Since the injection contact for our inverted device with HAT-CN HIL was truly ohmic while the injection contacts corresponding to the other devices were somewhat injection-limited, the measured τ_{Dl} for the inverted device with HAT-CN HIL was shorter than those obtained for the other devices. Using Equation 3, the carrier mobility was plotted as a function of electric field for each of the normal and inverted NPB devices with either MoO₃ or HAT-CN HIL (see Figure 2-9). The field-dependent mobility values extracted from previously reported time-of-flight (TOF) measurements are shown for comparison⁵³. The extracted hole mobility for the devices correlated very well with the measured injection efficiencies. Devices with higher injection efficiency showed a larger μ_{Dl} under the same applied field. The mobility values for inverted device with HAT-CN HIL are in good agreement with previously reported time-of-flight (TOF) mobility values measured at the same applied electric field for NPB single-carrier devices^{39,53}. These results provide further evidence that inverting the device architecture when using electron acceptors as HILs is necessary to improve hole injection into organic electronic devices.

2.3.3 MoO₃-doped NPB Injection Layer For Improved Hole Injection

The enhancement in hole injection observed in the inverted devices is attributed to enhanced charge transfer at the top hole-injecting contact. In the inverted device, the electron acceptor dopes the surface and subsurface of the organic semiconductor during thermal evaporation. To confirm that the improved hole injection using electron

acceptors as HIL is due to interfacial doping, we fabricated normal structure devices with a 10 nm thick MoO₃ HIL and compared the results to devices with a 10 nm thick NPB:MoO₃ HIL of different doping concentrations. Figure 2-10 shows the current density and the hole injection efficiency vs. electric field plots for these devices. As expected, hole injection for the normal NPB device with MoO₃ HIL is contact limited. When the MoO₃ HIL is replaced with a NPB:MoO₃ HIL, significantly larger current densities and enhanced injection efficiencies are obtained. As the doping concentration in the NPB:MoO₃ HIL is increased from 1-10 mol%, the hole injection efficiency is greatly increased at high fields. The difference in hole injection for these devices is due to the degree of surface and subsurface doping occurring at the bottom hole-injecting contact. With MoO₃ as a HIL, the surface layer of NPB is *p*-doped due to the charge transfer at the MoO₃ / NPB interface^{54,55}. By doping the entire HIL with MoO₃, the resulting heavily *p*-doped NPB enables the formation of ohmic contacts for enhanced hole injection.

This interfacial doping model characterized by the surface and subsurface doping of NPB when using electron acceptors as HIL also applies to our results for HAT-CN assuming that this electron acceptor serves as a *p*-type dopant. Based on the results of our injection study, HAT-CN provides stronger surface and subsurface doping of NPB compared to MoO₃ when used as an injection layer. To compare the *p*-type doping of NPB due to MoO₃ and HAT-CN, we fabricated MoO₃-doped and HAT-CN-doped NPB hole-only devices. The same doping concentration (10 mol%) was used for each electron acceptor. The current density-electric field characteristics of these devices are shown in Figure 2-11. The data for an undoped NPB hole-only device with HAT-CN HIL

is also shown for comparison. The data for the undoped device shows the transition from ohmic to trap limited to trap-free SCL transport. On the other hand, the HAT-CN-doped NPB devices show only trap-free SCL transport over the entire voltage range with a current density 3 orders of magnitude larger than the undoped device in the ohmic regime. Compared to the HAT-CN device, the MoO₃-doped NPB device shows the transition from trap limited transport to trap-free SCL transport with a current density at low fields substantially lower than that of the HAT-CN-doped NPB device. These results show a clear indication of *p*-type doping effect of NPB using HAT-CN as dopant which is significantly stronger than that of the devices with MoO₃ doped layer, confirming that HAT-CN provides stronger charge transfer with NPB when used as a dopant compared to MoO₃. When used as a hole injector, HAT-CN would therefore provide stronger interfacial doping of NPB compared to MoO₃ and allow for more efficient charge injection in OLED devices. Based on these results, we conclude that both MoO₃ and HAT-CN injection layers rely on efficient surface and subsurface doping of NPB to form an ohmic contact for hole injection.

Lastly, the anode/electron acceptor interface could play a critical role in the results reported in this chapter. To address the issue of whether the metal/electron acceptor interface contributed to the injection efficiencies of the NPB single-carrier devices, the hole current densities for normal devices with HAT-CN HIL and either Au or ITO as anode were analyzed. The measured current densities for the devices were independent of the electrode used for the device as shown in Figure 2-12. This result is in agreement with previous studies on metal/electron acceptor interfaces, which showed that the strong charge transfer between the electron acceptor and the anode leads to a

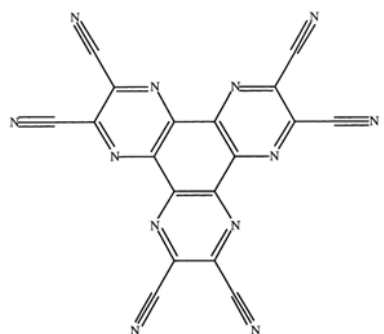
lowering of the interfacial energy barrier^{56,57}. The work function of the anode becomes pinned to the Fermi level of the electron acceptor, with this Fermi-level pinning being observed for ITO and various metals when paired with an electron accepting HILs⁵⁸. This behavior is consistent with the classical description of an ohmic contact between a metal and an n-type semiconductor, which requires that the work function of the n-type semiconductor (Φ_n) is larger than the work function of the metal (Φ_m)⁵⁹. This phenomenon is independent of the device architecture employed, since the degree of charge transfer between the anode and the electron acceptor is very strong^{29,30}. Based on these findings, we confirmed that the interfacial doping of NPB at the NPB/electron acceptor interface is responsible for the enhanced hole injection in inverted NPB devices.

2.4 Concluding Remarks

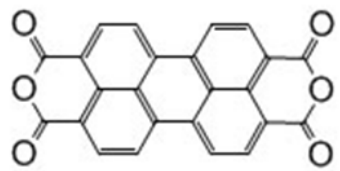
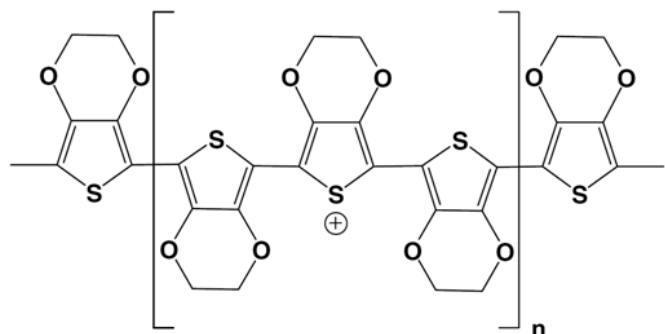
In conclusion, enhanced hole injection has been demonstrated for inverted NPB hole-only devices by using electron acceptors as HIL. *J-V* and DI-SCLC transient measurements were performed to cross-examine the hole injection behavior in normal and inverted NPB hole-only devices. The enhanced hole injection in the inverted hole-only devices was due to enhanced charge transfer at the NPB/electron accepting HIL interface. An interfacial doping model was then proposed to explain the results obtained for the normal and inverted devices. By utilizing MoO₃-doped NPB HILs, it has been demonstrated that the hole injection in the normal NPB device can be further enhanced. Increasing the doping concentration of the MoO₃-doped NPB HIL directly increased the injection efficiency, highlighting the importance of interfacial doping to obtain an ohmic contact using these electron acceptors. Lastly, it was determined that a strong degree of

charge transfer between the HAT-CN and NPB was responsible for the large injection efficiencies obtained in devices with HAT-CN injection layer.

HAT-CN

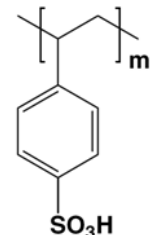
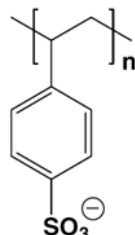


PEDOT



PTCDA

C₆₀



PSS

Figure 2-1. Molecular structure of electron acceptors and conducting polymers used as injection layers in conventional OLEDs.

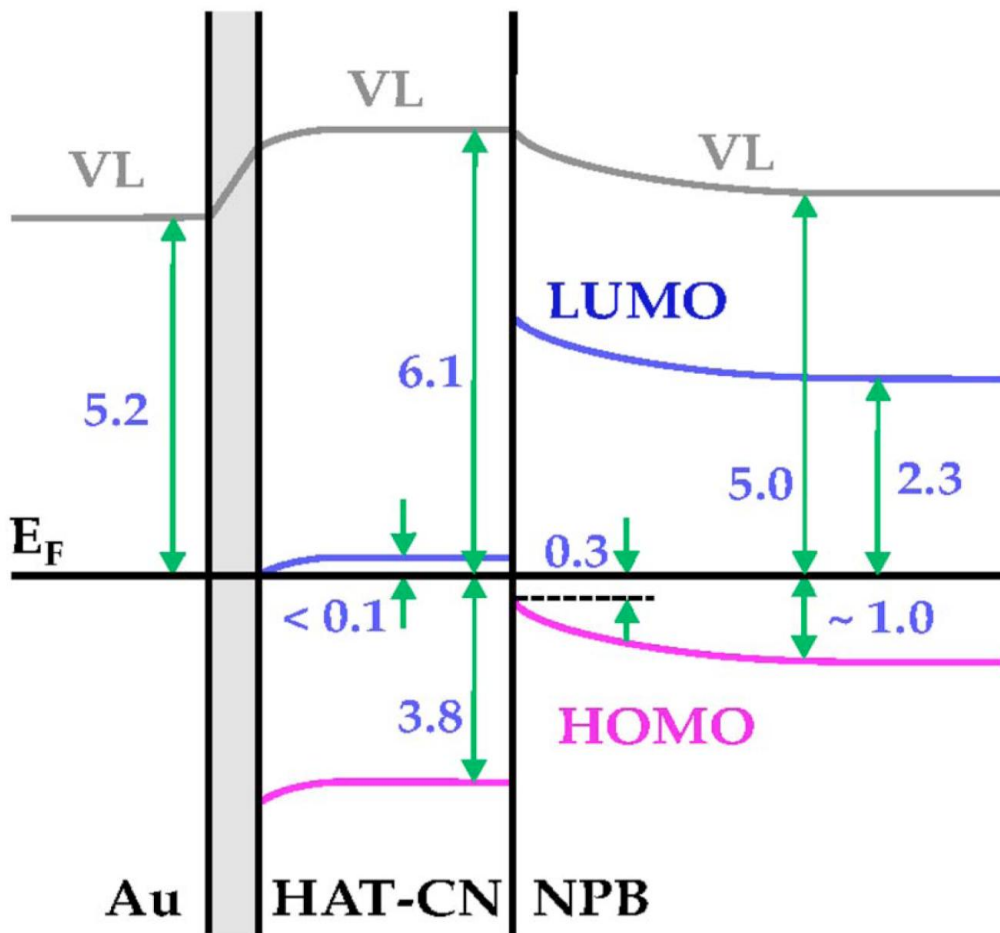


Figure 2-2. Energy level diagram at the NPB/HAT-CN/Au interface. Reproduced with permission from Kim, Y.-K. et al. *Appl. Phys. Lett.*, vol. 94, 063305, 2009³⁰.

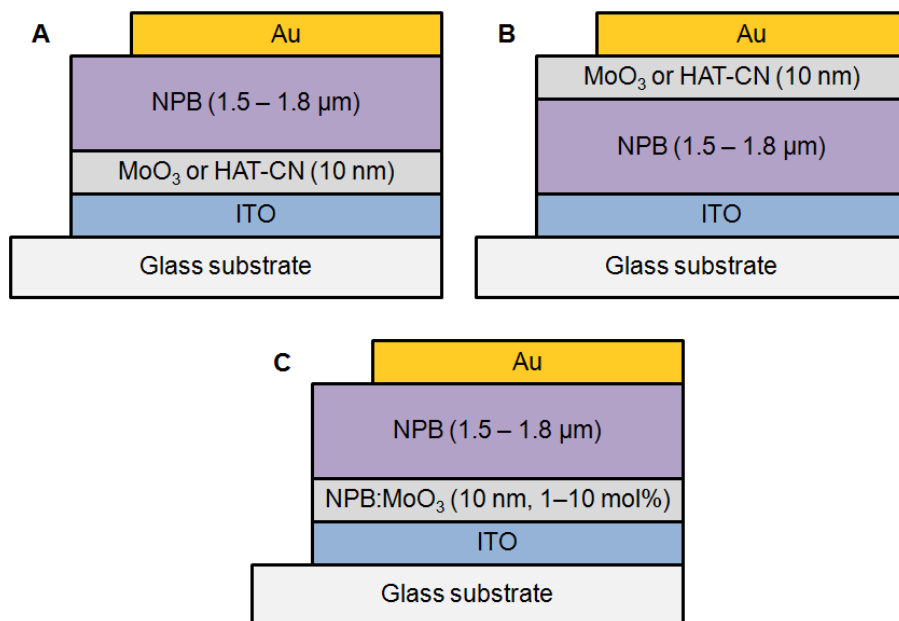


Figure 2-3. Schematic cross-section view of NPB single-carrier devices fabricated in this study. A) Conventional device with bottom-contact Mo_O₃ or HAT-CN HIL. B) Inverted device with top-contact Mo_O₃ or HAT-CN HIL. C) Conventional device with a NPB:Mo_O₃ interlayer (1–10 mol% doping concentration).

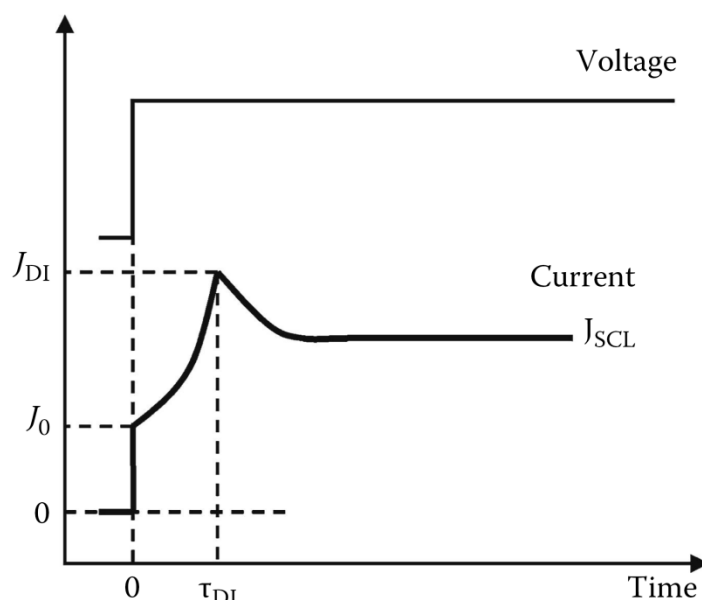


Figure 2-4. An ideal DI-SCLC transient current response for a trap-free organic semiconductor. Reproduced with permission from Tse, S. et al. *J. Appl. Phys.*, vol. 100, 063708, 2006⁴³.

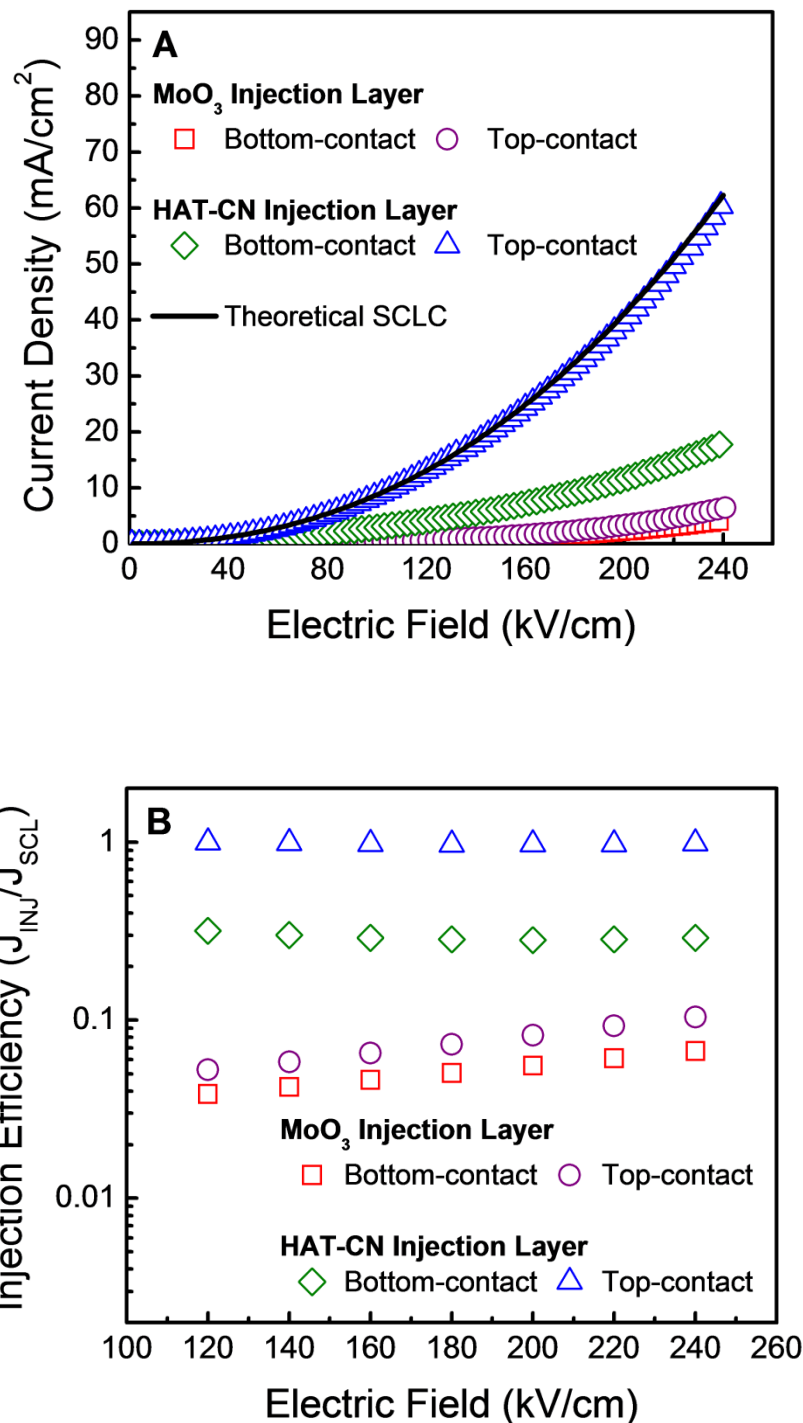


Figure 2-5. Current density and injection efficiency vs. electric field for conventional and inverted NPB hole-only devices using MoO₃ or HAT-CN as HIL. A) J - E curves for the device studied. Solid line represents theoretical J_{SCL} . B) Hole injection efficiency as a function of electric field for the devices⁶⁰.

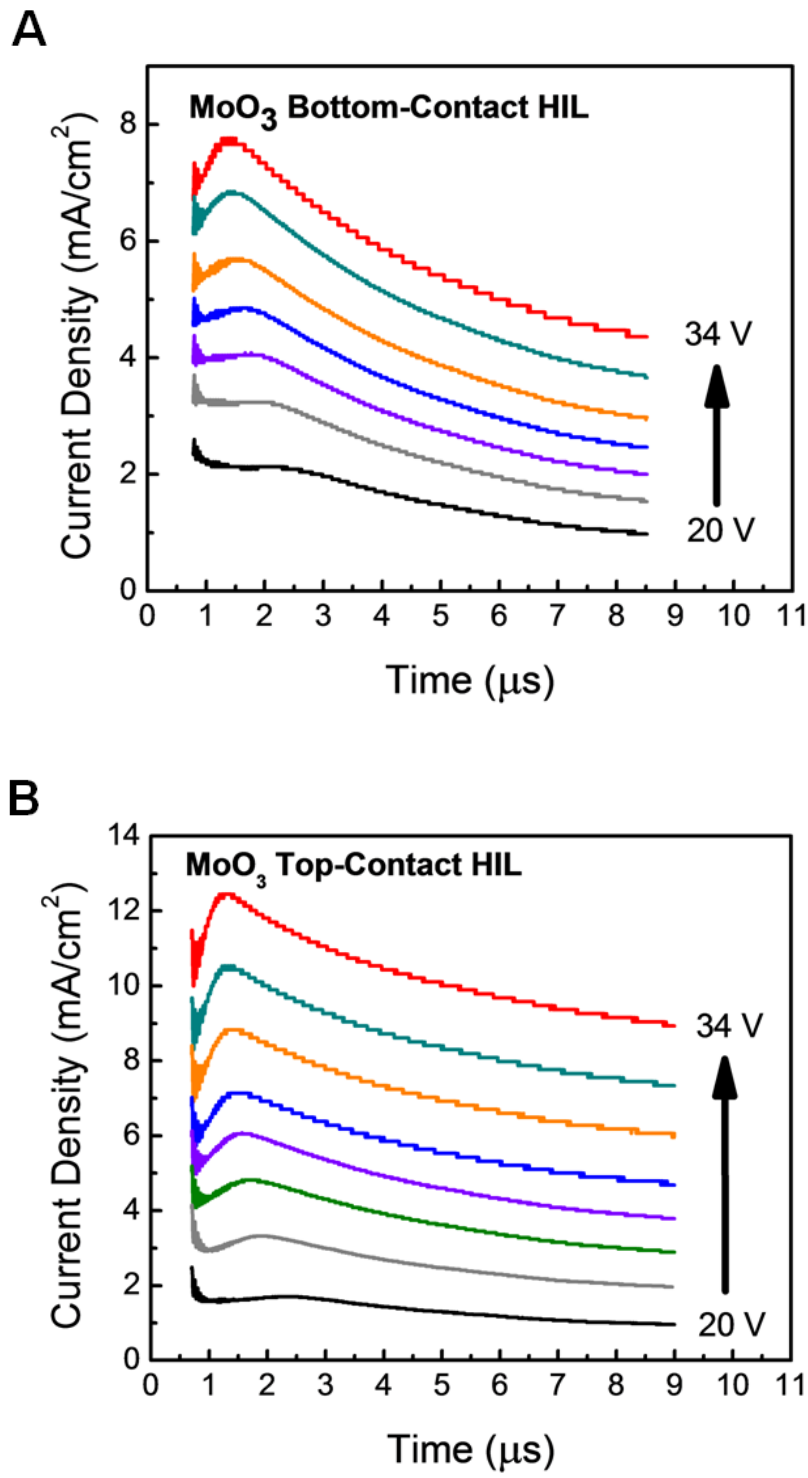


Figure 2-6. DI-current density transients measured at various applied voltages using MoO_3 as HIL. A) Normal device architecture. B) Inverted device architecture⁶⁰.

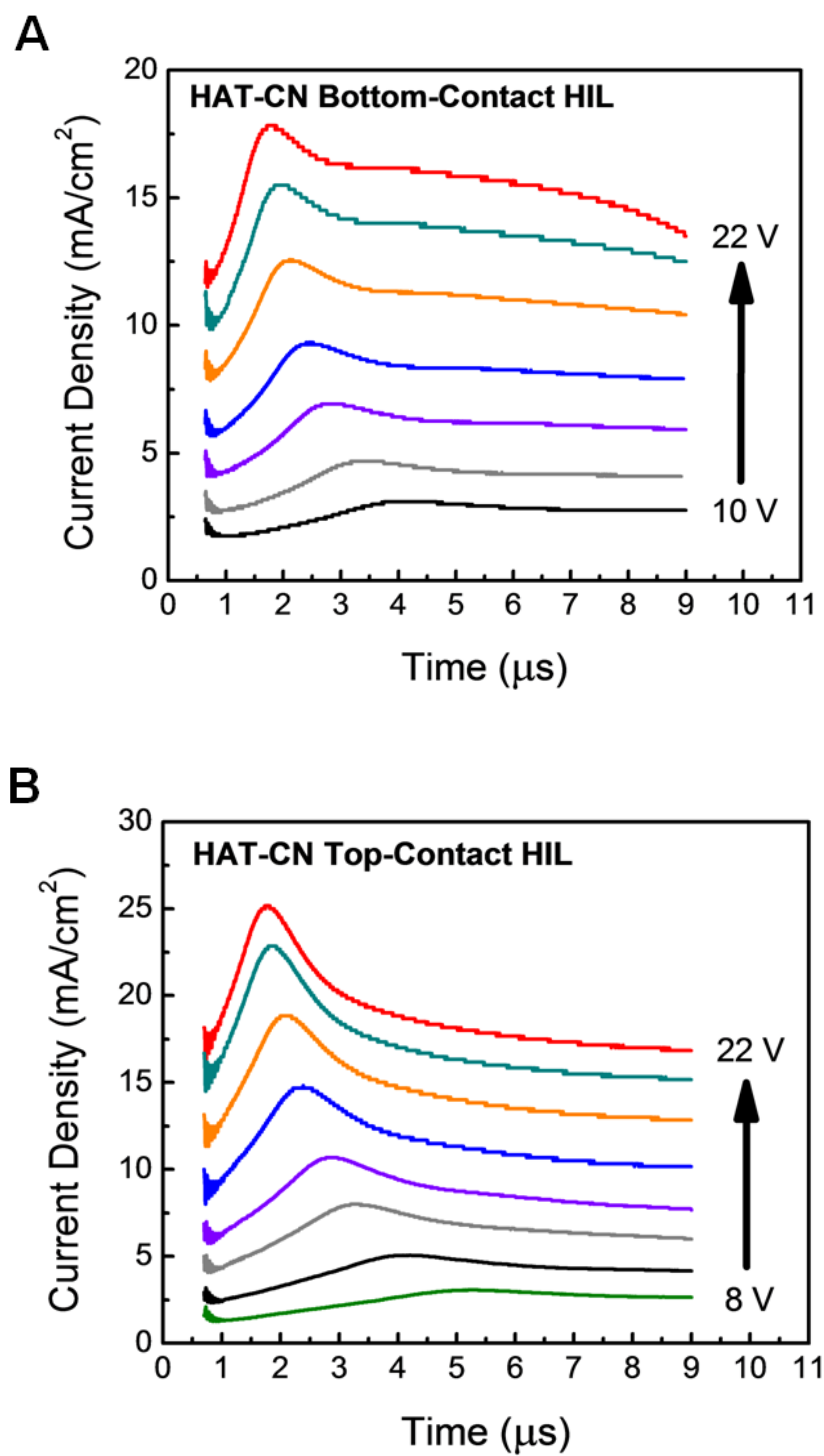


Figure 2-7. DI-current density transients measured at various applied voltages using HAT-CN as HIL. A) Normal device architecture. B) Inverted device architecture⁶⁰.

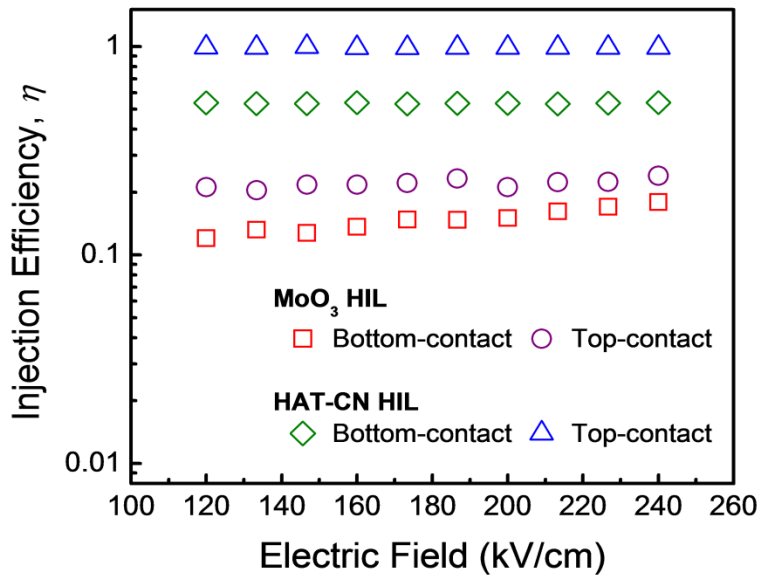


Figure 2-8. Injection efficiency, η , extracted from DI-SCLC transient current measurements vs. electric field for normal and inverted NPB single-carrier devices with either MoO₃ or HAT-CN as injection layer⁶⁰.

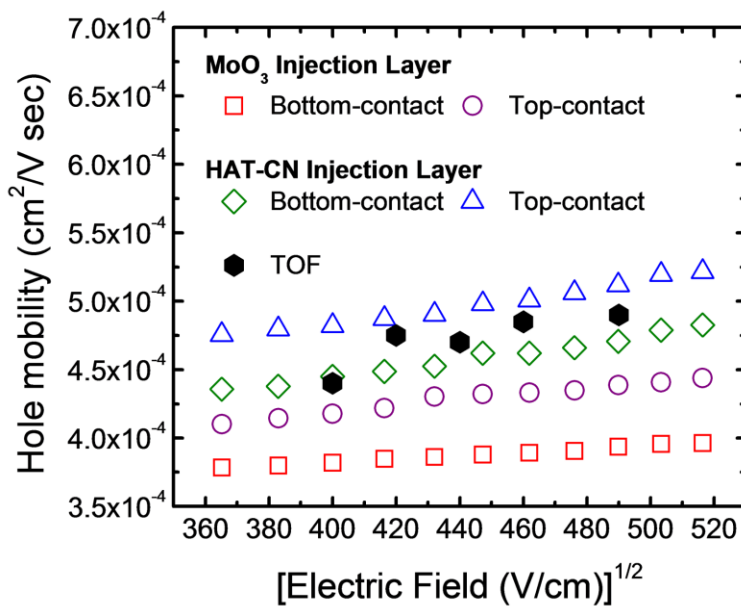


Figure 2-9. Hole mobility (μ_{DI}) as a function of electric field ($F^{1/2}$) for normal and inverted NPB hole-only devices with either MoO₃ or HAT-CN injection layer. Field-dependent mobility based on time-of-flight (TOF) measurements is shown for comparison^{53,60}.

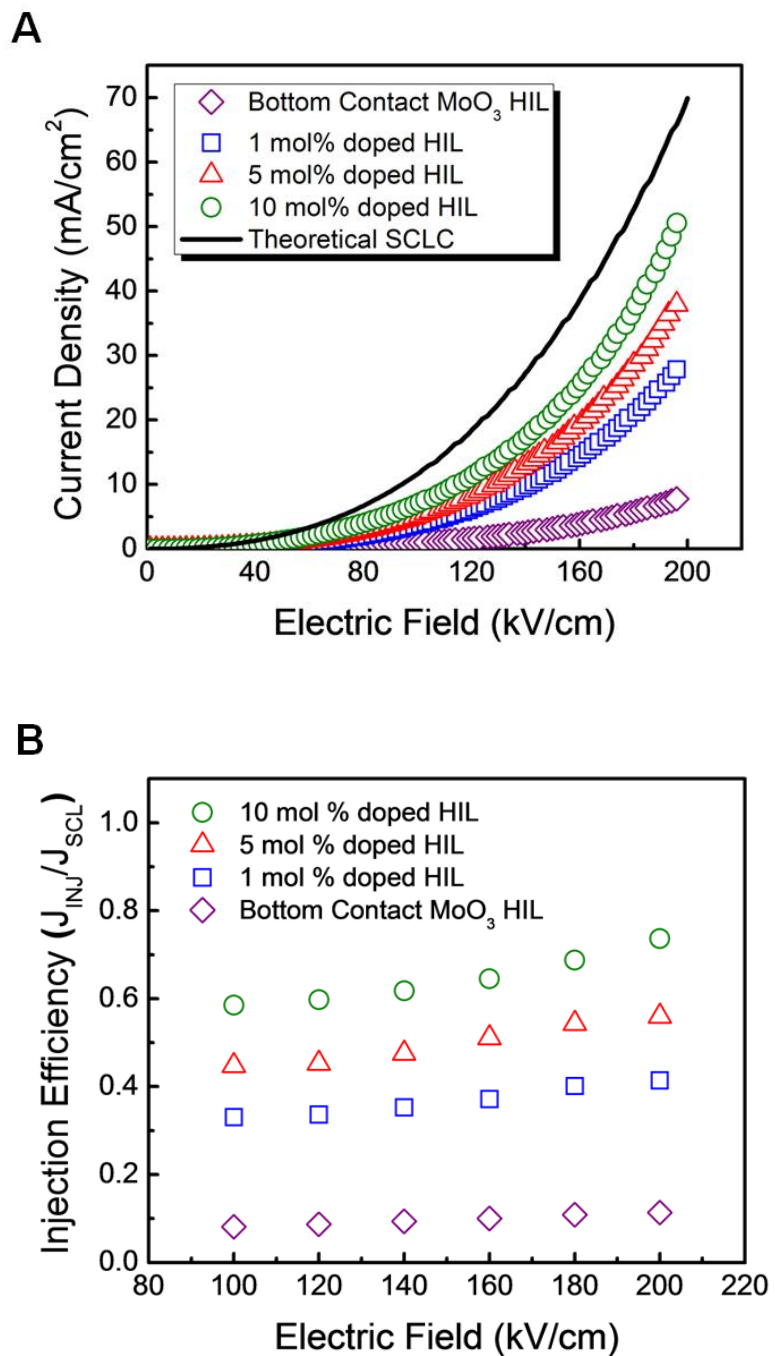


Figure 2-10. Current density and injection efficiency plots for conventional NPB hole-only devices with either a neat MoO_3 or MoO_3 -doped NPB HIL of varying doping concentration (1, 5, 10 mol%). A) J - E curves for the devices. B) Injection efficiency-electric field plot for the devices⁶⁰.

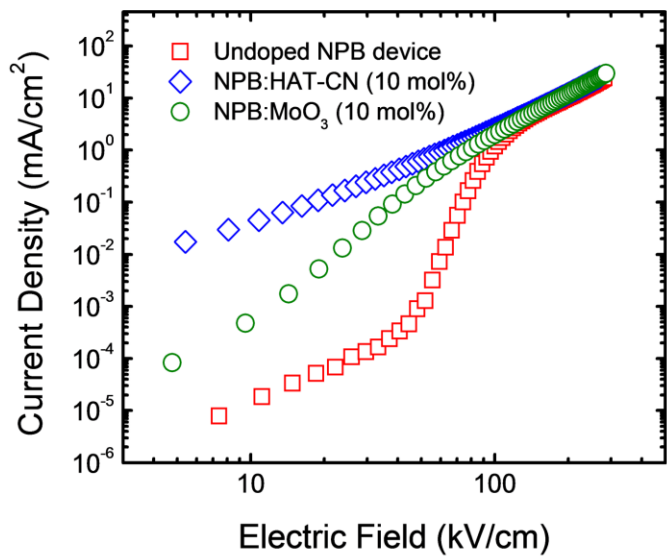


Figure 2-11. Current density vs. applied electric field for MoO_3 -doped and HAT-CN-doped NPB single-carrier devices. The data for an undoped NPB hole-only device with HAT-CN HIL is shown for comparison⁶⁰.

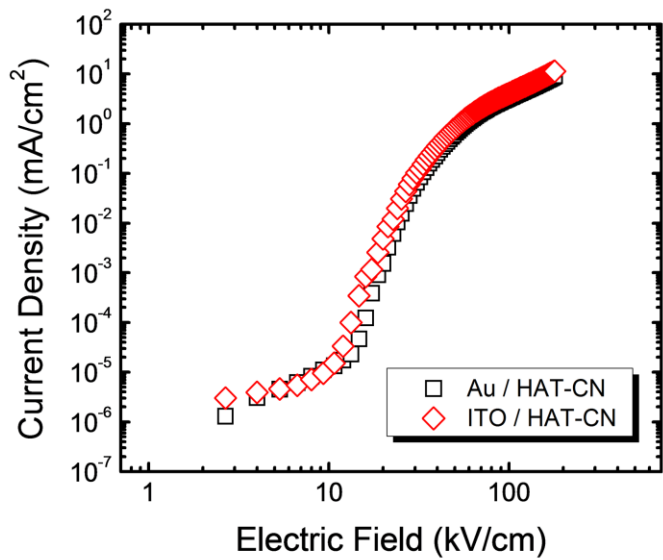


Figure 2-12. Current density vs. electric field for normal NPB single-carrier devices with either ITO or Au anode. HAT-CN is used as injection layer for both devices⁶⁰.

CHAPTER 3

INTRODUCTION TO ORGANIC PHOTOVOLTAIC CELLS

3.1 Overview and History

Due to the significant effort in the research and development of photovoltaic cells, this renewable energy technology has become a promising candidate for meeting the world's energy requirements. The state-of-the-art for this technology consist of photovoltaic cells using inorganic materials such as silicon and compound semiconductors. Photovoltaic cells and modules based on these materials have shown high power conversion efficiencies, highlighting the potential of this technology to achieve grid-parity. However, to achieve grid-parity, the total cost per watt would need to be reduced for this technology to be competitive with non-renewable energy sources. In an attempt to reduce the material and processing cost, thin-film inorganic photovoltaic cells using materials such as amorphous/nanocrystalline Si, CdTe, and $\text{CuIn}_{1-x}\text{Ga}_x\text{Se}_2$ (CIGS) or $\text{Cu}_2\text{ZnSn}(\text{S}_{1-x}\text{Se}_x)_4$ (CZTSSe) have been adopted⁶¹⁻⁶³. Despite the potential cost savings associated with these thin-film devices, their power conversion efficiency, which is typically between 10–20%, is significantly lower than the state-of-the-art technology⁶⁴.

In addition to thin-film inorganic photovoltaic cells, devices based on organic materials is a promising technology for low-cost energy harvesting. These organic photovoltaic cells typically consist of either organic molecules of well-defined molecular weight, structure and chemical composition, or conjugated polymers with high molecular weight but a polydispersity index (PDI) greater than 1. Organic photovoltaic cells are intrinsically flexible, mechanical robust, and can be processed on inexpensive substrates using high-throughput methods. For example, small molecule OPVs are

generally processed by high vacuum thermal evaporation and can be processed in high throughput using this method^{65,66}. Similarly, devices based on conjugated polymers and novel oligomers can be fabricated by solution processing methods that are large-scale roll-to-roll (R2R) processing compatible, such as slot-die coating, doctor blading, and ink-jet printing⁶⁷⁻⁷⁰. Figure 3-1 illustrates various processing methods utilized in the fabrication of large-area and laboratory-scale organic solar cells. Organic photovoltaic cells also have an additional benefit associated with the design of organic small molecules and conjugated polymers: the electronic and optical properties of these organic materials can be modified by altering their chemistry. For example, one approach for enhancing the performance of organic photovoltaic cell is to manipulate the chemical structure of the electron donor. Modifications such as introducing electron withdrawing groups, reducing the conjugated length, or enhancing the planarity of the polymer can lower the bandgap, lower the HOMO level, or increase the polymer's carrier mobility, respectively^{71,72}. Such intelligent design of the conjugated polymer has lead to enhanced J_{sc} and V_{oc} in laboratory-scale organic photovoltaic cells.

Despite these advantages, the properties of the organic materials employed in organic photovoltaic cells have introduced a number of issues that have impacted device design. One of the key challenges with organic photovoltaic cells is to efficiently dissociate tightly bound electron-hole pairs, called excitons, generated within the organic semiconductor. There are two types of excitons formed in organic semiconductors: Frenkel excitons and charge-transfer excitons (CTEs)^{73,74}. Frenkel excitons consist of electron-hole pairs with a binding distance less than a single molecule, while charge-transfer excitons are characterized as electron-hole pairs that

are delocalized over adjacent molecules. The binding energy for these excitons are both greater than 0.1 eV^{73,74}. To separate these tightly-bound excitons, the first organic photovoltaic cells utilized Schottky diodes to facilitate exciton dissociation. Although the strong electric field near the metal electrode-organic interface dissociated excitons and generated charge carriers, exciton quenching at this interface and limited exciton dissociation throughout the photoactive layer limited the overall device performance⁷⁵⁻⁷⁷. In 1986, a major breakthrough in organic photovoltaic cell performance was achieved by Ching Tang with the demonstration of the donor-acceptor (D:A) bilayer heterojunction photovoltaic⁷⁸. A schematic diagram illustrating the D:A bilayer heterojunction structure is shown in Figure 3-2. In the bilayer heterojunction photovoltaic cell, excitons generated within the organic materials dissociate at the heterojunction assuming that the energy level offset between the donor and acceptor are large enough to provide a sufficient driving force. For efficient device operation, the thickness of the donor and acceptor layers must be less than the exciton diffusion length (L_D)⁷⁹. Although the shift to the bilayer D:A heterojunction structure lead to enhanced photocurrent produced by the device, exciton dissociation was still limited since the PV cells consisted of only one D:A interface. In the 1990's, a further enhancement in exciton dissociation was demonstrated in OPVs through the development of the D:A bulk heterojunction (BHJ) photovoltaic cell⁷⁹⁻⁸¹. In BHJ photovoltaic cells, the interpenetrating network created by the D:A blend resulted in enhanced exciton dissociation since photogenerated excitons now were within L_D (see Figure 3-2). Significant enhancements in photocurrent were observed for these photovoltaic cells as compared to bilayer heterojunction devices. In more recent work, improvements to BHJ structure (optimizing the D:A blend

morphology, incorporating anode/cathode interlayers) and modification of the donor conjugated polymer's energy levels have led to a world record power conversion efficiency of 9.21% in single junction devices⁸².

3.2 Principles of Operation

To better appreciate the progress that has been made in organic photovoltaic cell research, it is important to understand the operating principles of these devices. The ability to generate power in an OPV cell is dependent on four processes that sequentially occur with the photoactive layer. These processes are as follows: photon absorption, exciton diffusion, charge transfer (exciton dissociation), and charge carrier collection. The external quantum efficiency (EQE, η_{EQE}), or the ratio of the number of charge carriers collected by the photovoltaic cell to the number of photons incident on the device, is the product of the efficiencies associated with each of the four processes:

$$\eta_{EQE} = \eta_A \eta_{ED} \eta_{CT} \eta_{CC} \quad (3-1)$$

where η_A is the photon absorption efficiency, η_{ED} is the exciton diffusion efficiency, η_{CT} is the efficiency of charge transfer, η_{CC} and is the charge carrier collection efficiency.

This expression can also be written as:

$$\eta_{EQE} = \eta_A \eta_{IQE} \quad (3-2)$$

where η_{IQE} is the internal quantum efficiency. In the ideal case, a η_{EQE} value approaching unity can be achieved if both η_A and η_{IQE} are maximized. However, in the state-of-the-art OPV cells, the processes influencing absorption efficiency and internal quantum efficiency are opposing. Since organic semiconductors have a high absorption coefficient (α) of $\sim 10^4$ to 10^5 cm⁻¹, the optical absorption length ($1/\alpha$) in these materials is typically at least 100 nm^{83,84}. As a result, increasing the photoactive layer thickness in

BHJ OPV cells above 100 nm enhances η_A . However, charge carrier collection becomes limited due to recombination losses in the thicker photoactive layer. Research efforts have focused on enhancing device performance despite this tradeoff between η_A and η_{IQE} . Chapter 4 will demonstrate an approach to enhance charge carrier collection through the use of novel interlayers, while Chapter 5 will highlight this tradeoff problem for high efficiency polymer photovoltaic cells with increased active layer thickness.

3.3 Photovoltaic Cell Characterization

The key parameters used to characterize organic photovoltaic cells under operation will be discussed herein. In general, photovoltaic cells act as photodiodes which operate when unbiased and show rectifying behavior. These devices differ from typical photodiodes in that a wide spectral response over a broad solar wavelength range is required⁸⁵. The current-voltage (J - V) characteristics for a photovoltaic cell in the dark and under illumination is shown in Figure 3-3. The J - V characteristics for the effective photocurrent (J_{ph}), which is the difference between the current under illumination (J_L) and the dark current (J_D), is also shown. From the J_L - V curve, the key parameters used to characterize the device performance can be extracted. The short-circuit current (J_{sc}), the photocurrent at zero bias, and the open-circuit voltage(V_{oc}), the voltage at which the $J_L = 0$, is highlighted in the figure. The product of the J_{sc} and V_{oc} is the theoretical maximum power produced from the cell. The actual maximum power output ($P_m = I_m \times V_m$) is typically less than this theoretical maximum. The determination of P_m is illustrated by a small rectangle in Figure 3-3. The fill factor (FF) measures the sharpness of the J_L - V curve and is defined as the ratio between the actual and theoretical maximum power outputs⁸⁵,

$$FF \equiv \frac{J_m V_m}{J_{sc} V_{oc}}. \quad (3-3)$$

The most important figure-of-merit is the power conversion efficiency (η_p), which is the ratio of the maximum power output to the incident power P_{inc} ,

$$\eta_p = \frac{P_m}{P_{inc}} = \frac{J_{sc} V_{oc} FF}{P_{inc}}. \quad (3-3)$$

3.3.1 Current-Voltage Measurement

To experimentally determine η_p , the J - V characteristics of the organic photovoltaic cell were measured in the dark and under Air Mass 1.5 global (AM 1.5G) illumination. The standard reporting conditions (SRC) for rating the performance of terrestrial photovoltaic cells are as follows: 100 mW cm⁻² (1 sun), AM 1.5G reference spectrum, and 298 °K cell temperature. To measure the current-voltage characteristics, a standard test method for photovoltaic cells was utilized⁸⁶. A xenon lamp with 1.5G air mass filter was used to simulate the solar spectrum. The incident light from the solar simulator was calibrated using a certified Si reference cell to ensure that $P_{inc} = 100$ mW cm⁻². To control the incident light intensity, neutral density filters were used so P_{inc} could be varied from 10 to 100 mW cm⁻². With the J - V characteristics measured, the key parameters described in the previous section can be extracted.

3.3.2 Spectral Response Measurement

To experimentally determine η_{EQE} , a spectral responsivity measurement was performed on the organic photovoltaic cells studied in this work. A computer-controlled spectral responsivity measurement system that met the ASTM E1021 testing standard was used for this measurement⁸⁷. The measurement system consisted of a 150 W xenon arc lamp solar simulator with a 1.5G AM filter coupled with a monochromator as

the light source, producing monochromatic light with wavelengths from 400 nm to 1800 nm. The light beam from the monochromator is collimated and chopped using a collimating lens and a optical chopper, respectively. The optical chopper creates an alternating signal which allows the photocurrent produced by the test cell to be differentiated from the background noise. By connecting the chopper to a lock-in amplifier and using the chopper frequency (~400 Hz) as a reference , the photocurrent signal can be isolated. The chopped monochromatic light then passes through a condensing lens to either a calibrated Si photodetector for measuring the wavelength-dependent incident light power or to the test cell. The beam spot size is less than both the Si photodetector area and the test cell area for accuracy. A *labVIEW* program was used to control the testing procedure and acquire the relevant data.

The spectral responsivity and, ultimately, the external quantum efficiency spectrum can now be calculated. The spectral responsivity for the test cells, $S_T(\lambda)$, is calculated as follows:

$$S_T(\lambda) = \frac{J_{cell}(\lambda)}{P_{inc}(\lambda)} = \frac{J_{cell}(\lambda)}{J_D(\lambda)/R_D(\lambda)} \quad (3-4)$$

where $J_{cell}(\lambda)$ is the measured photocurrent density of the test cell, $P_{inc}(\lambda)$ is the incident light power measured with the Si photodetector, $J_D(\lambda)$ is the Si photodetector current density, and $R_D(\lambda)$ is the responsivity of the reference detector. The external quantum efficiency, also known as the incident photon-to-current efficiency (IPCE), can now be calculated as

$$EQE(\lambda) = \frac{hc}{q\lambda} \times S_T(\lambda) \times 100\% \quad (3-5)$$

where h is Planck's constant, c is the speed of light, q is the electron charge, and λ is the wavelength. Lastly, the short-circuit current density under AM 1.5G illumination at 100 mW cm⁻² can be calculated from the external quantum efficiency spectrum as

$$J_{sc} = \int_{\lambda_1}^{\lambda_2} \frac{q\lambda}{hc} EQE(\lambda)S(\lambda)d\lambda \quad (3-5)$$

where $S(\lambda)$ is the reference AM 1.5G power intensity. Ideally, the integrated J_{sc} calculated from the EQE spectrum should match the value extracted from the J - V characterization for the test cells. This is only possible if the calibrations for both the J - V measurement setup and the spectral responsivity measurement setup are done correctly.

3.4 Progress in Organic Photovoltaic Cell Performance

Since the first demonstration of organic photovoltaic cells utilizing the BHJ structure, research efforts have focused on enhancing the power conversion efficiency of these devices. Improving the properties of the conjugated polymers and organic small molecules used as the donor in the D:A blend through intelligent chemical design has been largely responsible for the high efficiencies reported in the literature⁸⁸⁻⁹⁰. These materials are typically blended with C₆₀ fullerene or its derivatives to facilitate exciton dissociation within the photoactive layer. C₆₀ derivatives, such as [6,6]-phenyl-C61-butyric acid methyl ester (PCBM), have become the standard n-type materials used in OPV cells due to their high electron mobility and strong electronegativity⁹¹. This section will discuss the chemical design and important material properties of the novel conjugate polymers employed in Chapters 4 and 5 of this dissertation, as well as similar polymers reported in the literature. Furthermore, the power conversion efficiencies reported for polymer BHJ OPV cells incorporating these polymers will be highlighted.

3.4.1 Novel Conjugated Polymers for OPVs

Figure 3-4 shows the chemical structure for standard conjugated polymers and fullerene acceptor materials used in OPV cells⁹². Of the conjugated polymers shown in this figure, soluble thiophenes such as poly(3-hexylthiopene) (P3HT) has become a standard for the fabrication of solution-processed polymer OPV cells⁹³. Devices incorporating P3HT:PCBM blends showed higher charge carrier mobilities compared to previously reported OPV cells, leading to enhanced FF and power conversion efficiencies in these devices⁹⁴. Despite these enhancements, the large optical bandgap of P3HT (~1.9 eV) limits the fraction of the solar spectrum that can be harvested by the photovoltaic cell. To achieve power conversion efficiencies approaching 10%, conjugated polymers with optical bandgap between 1.4 eV and 1.7 eV would be required⁹⁵.

In addition to the previously mentioned methods for reducing the bandgap of the conjugated polymer (i.e. increasing the conjugation length, controlling the polymer chain planarity), the most common approach is to utilize an alternating donor-acceptor architecture. By incorporating alternating pairs of electron donating and accepting moieties within the polymer repeat unit, a push-pull driving force between these moieties allow for the bandgap of the polymer to be tuned^{96,97}. Figure 3-5 shows a schematic diagram illustrating the push-pull interaction for a donor-acceptor copolymer and the resulting bandgap. The advantage of this approach is that not only can the polymer's bandgap be reduced, but the position of its HOMO level can be lowered. Since $V_{oc} \propto (E_{HOMO}^{donor} - E_{LUMO}^{acceptor})$ for BHJ OPV cells, it is possible to increase the V_{oc} for the photovoltaic cell by lowering the donor polymer's HOMO level⁹⁵. However, this

approach is not without its disadvantages. As shown in Figure 3-5, the HOMO level for the copolymer is centralized around the donor unit while the LUMO level resides on the acceptor unit. For efficient hole transport along the copolymer's HOMO level, the donor unit must be in close proximity to other donor units. The same is true for electron transport along the copolymer's LUMO level, which is centralized around the acceptor unit. Therefore, interchain packing becomes critically important for sufficient carrier transport in donor-acceptor copolymers.

Figure 3-6 displays the chemical structure of representative donor-acceptor copolymers used in state-of-the-art polymer solar cells. Initial progress in the development of these novel polymers was made by incorporating the acceptor unit benzothiadiazole (BTD) into the copolymer. Examples include the copolymers poly[2,6-(4,4-bis-(2-ethylhexyl)-4H-cyclopenta[2,1-*b*;3,4-*b'*]dithiophene)-alt-4,7-(2,1,3-benzothiadiazole)] (PCPDTBT) and poly[N-9"-hepta-decanyl-2,7-carbazole-alt-5,5-(4',7'-di-2-thienyl-2',1',3'-benzothiadiazole)] (PCDTBT), both of which have shown power conversion efficiencies from 5.5% to 6.1% when incorporated in optimized polymer BHJ solar cells^{90,98}. A further enhancement in device performance was observed for donor-acceptor polymers composed of either benzodithiophene (BDT) or thienopyrrolodione (TPD) as the acceptor unit^{99,100}. For example, Reynolds and coworkers demonstrated high efficiency polymer solar cells incorporating a dithienosilole-fused (DTS) or dithienogermole-fused (DTG) donor-acceptor copolymer with TPD as the acceptor unit¹⁰¹. Replacing the carbon bridging atom in the donor unit with Si or Ge improved molecular chain packing in the BHJ film, leading to increased FF and power conversion efficiencies over 7% for the solar cell. Such manipulations to the chemical structure of

the conjugated polymer's has been vital to the continued improved of polymer solar cell performance.

3.4.2 Inverted Device Geometry

In addition to developing novel conjugated polymers for improved light harvesting and increased V_{oc} , researchers have also focused on the inverted device architecture for improved polymer solar cell stability and large-scale roll-to-roll (R2R) processing compatibility. A schematic of the conventional and inverted geometries employed for polymer solar cell fabrication is shown in Figure 3-7. In the inverted architecture, the device stability is improved since unfavorable materials such as acidic PEDOT:PSS and low work function metals are replaced by more favorable materials. Novel anode and cathode interlayers, which modify the work function of the electrodes and thus form Ohmic contacts for improved carrier extraction, have enabled high efficiency polymer solar cells with an inverted geometry to be realized. These interlayers also serve as selective contacts for electron or hole transport while effectively blocking the opposing charge carrier. Presently, novel interlayers for inverted polymer solar cells include n-type materials like TiO_x , ZnO , and water/alcohol soluble polyfluorenes, while transition metal oxides such as MoO_3 and V_2O_5 have been successfully used as anode interlayers for improved carrier extraction¹⁰²⁻¹⁰⁴. Using this approach, world-record certified power conversion efficiencies of over 9% has been demonstrated⁸².

In Chapter 4, high efficiency inverted polymer solar cells based on polydithienogermole-thienopyrrolodione (PDTG-TPD) will be discussed. The focus of that discussion will be on the materials characterization and electronic properties of a novel ZnO composite electron transporting layer employed in the device. The impact of this result on demonstrating the commercial viability of OPV cells will be highlighted. In

Chapter 5, the active layer thickness dependence of the power conversion efficiency will be investigated for inverted solar cells with novel low-bandgap polymers. Furthermore, the consequence of space-charge formation on carrier extraction will be discussed.

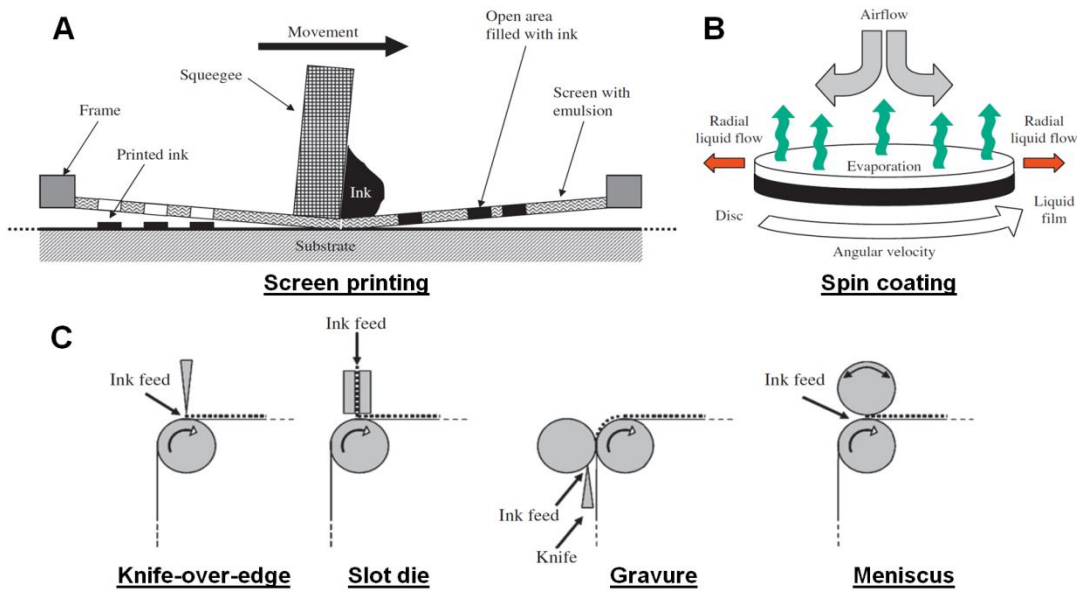


Figure 3-1. Schematic illustrations for various solution processing methods used in the fabrication of large-scale and laboratory-scale polymer photovoltaic cells. A) Screen printing. B) Spin coating. C) knife-over-edge, slot-die, gravure, and meniscus coating¹⁰⁵.

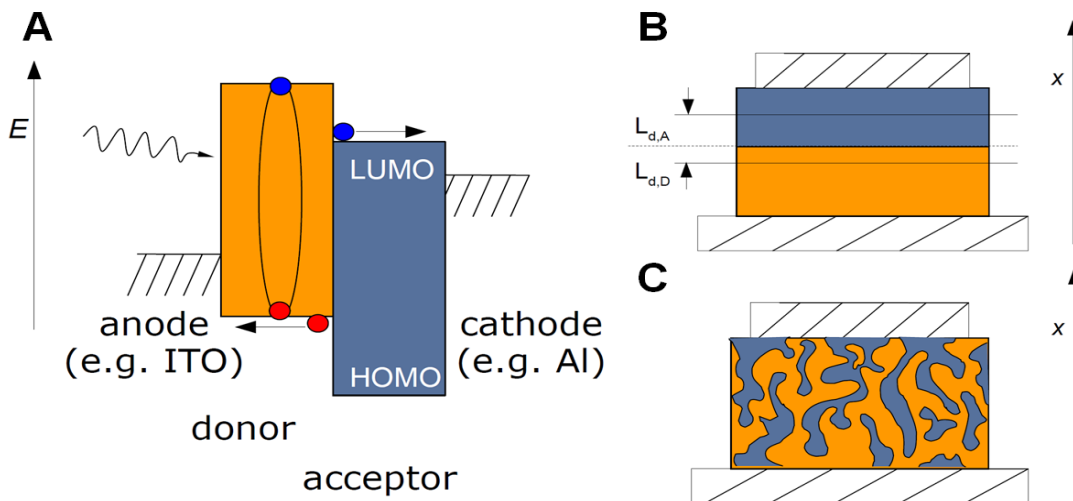


Figure 3-2. Schematic diagram illustrating an organic donor-acceptor heterjunction, as well as the bilayer and bulk heterojunction concepts. A) The D:A heterojunction. B) The bilayer heterojunction device structure. C) The bulk heterojunction device structure. Taken from: M. Riede. I-CAMP 2012 Lecture, Topic: "Vacuum Processing and the p-i-n Concept for OPV." Boulder, CO, July 7, 2012.

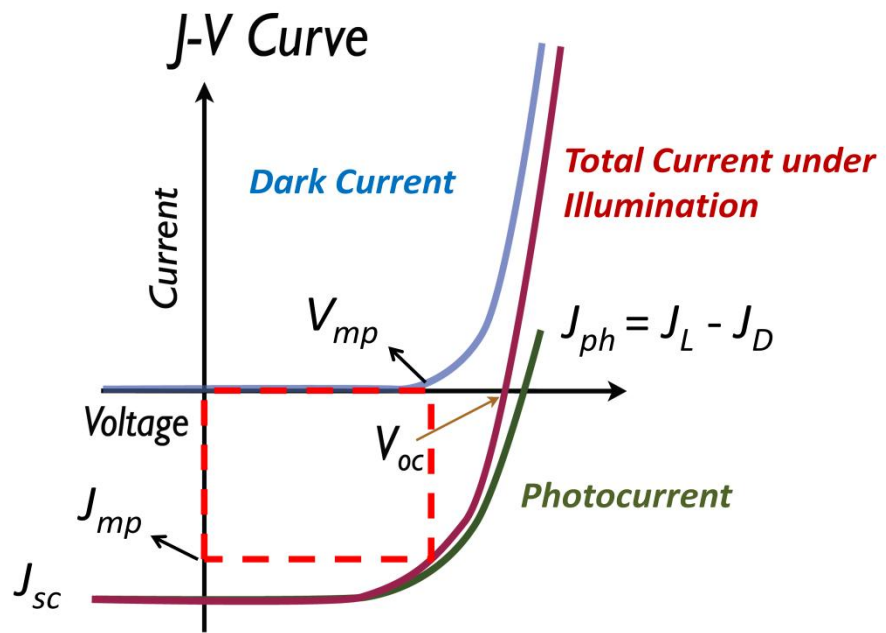
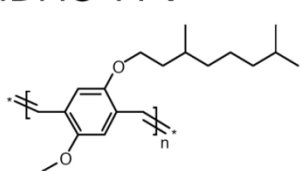


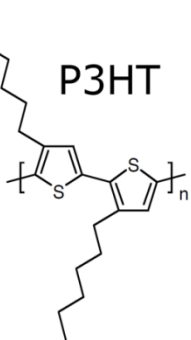
Figure 3-3. Typical J-V characteristics for a photovoltaic cell tested in the dark (J_D) and under illumination (J_L). The resulting photocurrent, which is given by $J_{ph} = J_L - J_D$, is also shown.

Typical electron donor materials: conjugated polymers and small-molecules

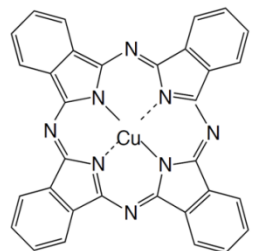
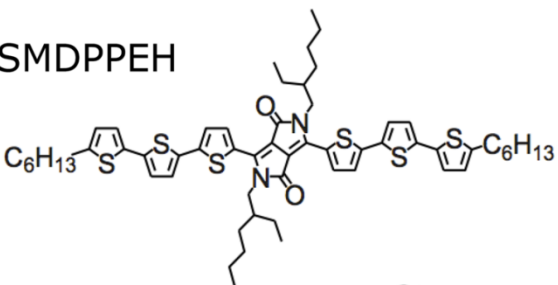
MDMO-PPV



P3HT

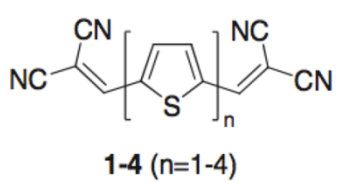


SMDPPEH

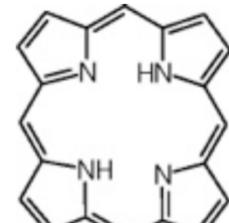


metal phthalocyanine

DCV_nT

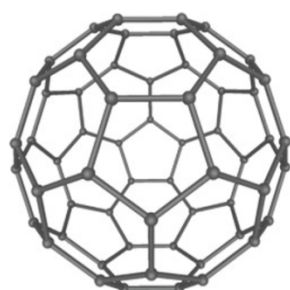


1-4 (n=1-4)

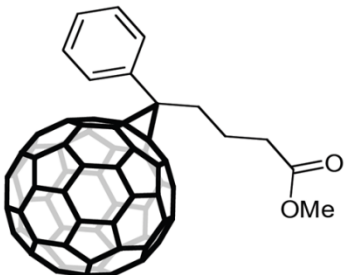


porphyrin

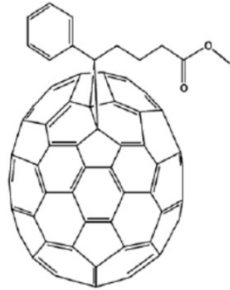
Typical electron acceptor materials:
vacuum-processed and solution-processable small-molecules



C₆₀



[60]PCBM



[70]PCBM

ICBA



Figure 3-4. Chemical structure for standard electron donor and acceptor materials used in the fabrication of organic photovoltaic cells.

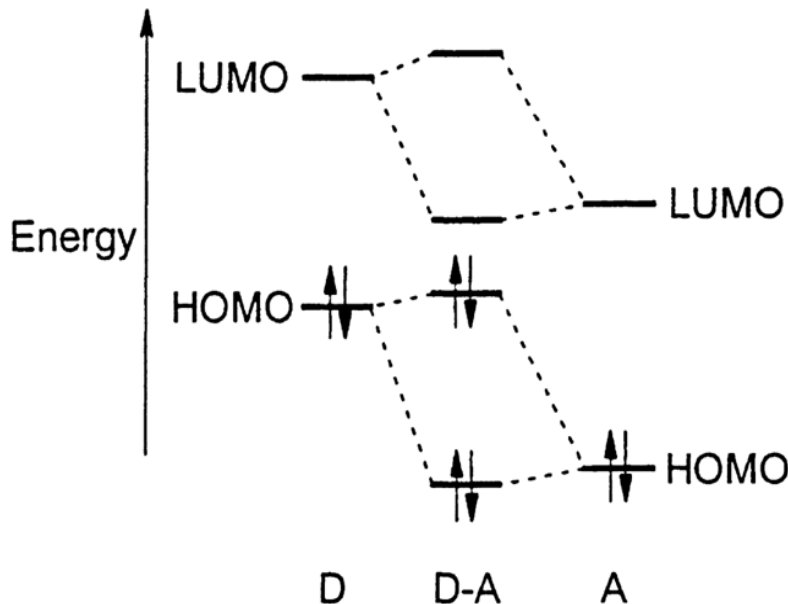


Figure 3-5. Schematic illustration showing the molecular orbital hybridization for a donor-acceptor (D-A) copolymer and the resulting reduction in the effective bandgap¹⁰⁶.

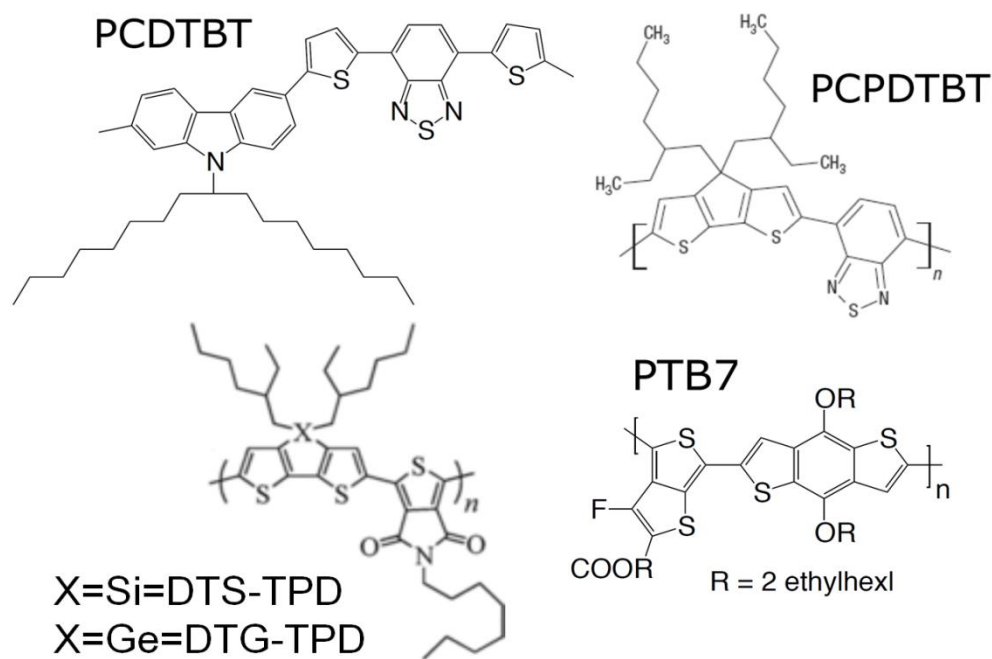


Figure 3-6. Chemical structure for state-of-the-art donor-acceptor copolymers used for high efficiency polymer photovoltaic cells.

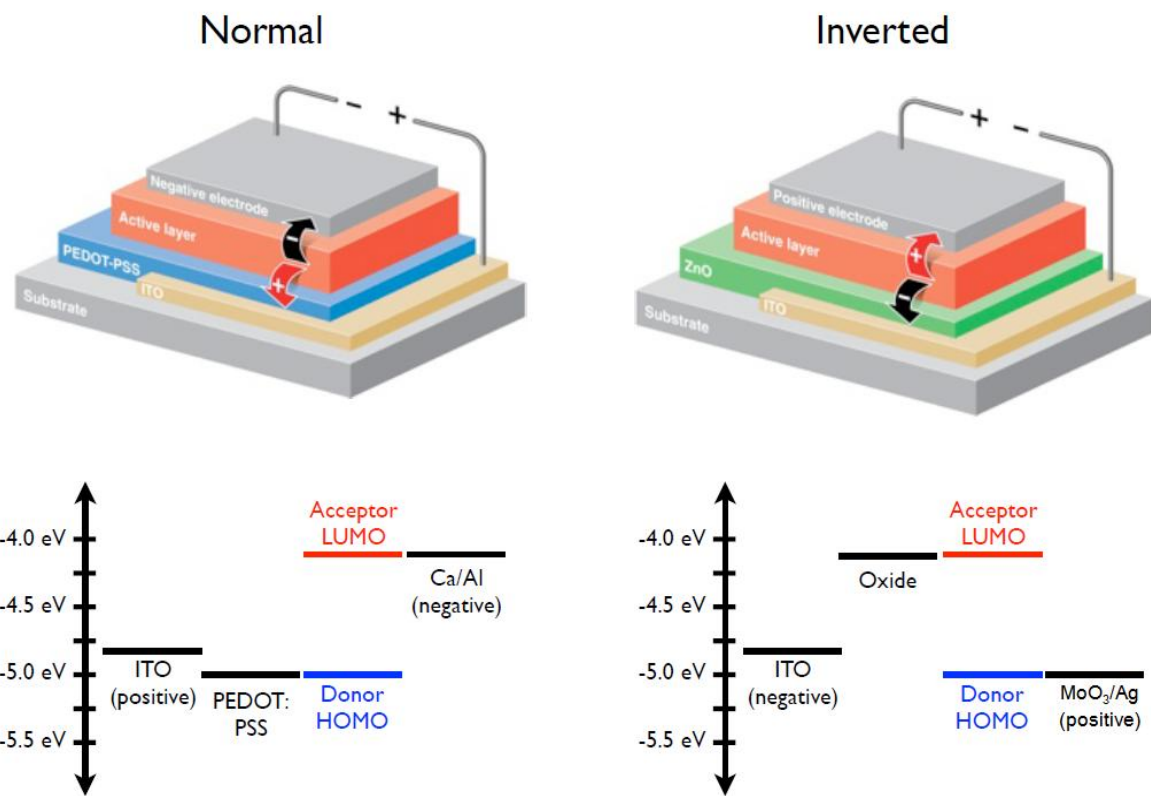


Figure 3-7. Normal vs. inverted device architectures for organic photovoltaic cells¹⁰⁷.

CHAPTER 4

HIGH EFFICIENCY INVERTED POLYMER PHOTOVOLTAIC CELLS

4.1 Introductory Remarks

Extensive efforts have been directed at developing polymer bulk heterojunction (BHJ) solar cells due to their potential for low-cost energy harvesting^{108,109}. High-efficiency, laboratory-scale polymer solar cells based on low-bandgap polymers have been demonstrated as highlighted in Chapter 3^{98,110-113}. The device geometry of typical laboratory-scale polymer solar cells consists of a bottom indium tin oxide (ITO) anode, an anode interfacial layer, a photoactive layer, and a low-work function top metal cathode. Because vacuum deposition of low-work function metals is required for these top cathode devices, it is not viable to use this device architecture in large-scale roll-to-roll (R2R) processing.

To avoid the use of low-work function metals employed in such devices, large-scale R2R processed modules and laboratory-scale model devices have utilized a device geometry in which the polarity of the solar cells is inverted^{16,114-116}. Figure 4-1 compares the typical solar cell geometry used for laboratory-scale devices and the inverted solar cell geometry used both laboratory-scale devices and large-scale R2R-processed modules for a P3HT:PCBM solar cell. As displayed in Figure 4-1, inverted cells have an oxide electron-transporting layer (ETL)-coated ITO as the bottom cathode and a screen-printed Ag layer as the top anode. To date, this device architecture is prototypical for the fabrication of large-scale R2R-processed modules as shown in Figure 4-2^{16,114-116}. Ultimately, there are two factors promoting the use of the inverted device geometry for large-scale R2R processing. For one, the commercial availability of printable Ag formulations makes solution processing of the Ag electrode a possibility.

Second, the development of solution-processed transition metal-oxides such as TiO_x and ZnO has lead to their use in large-scale solar cell manufacturing as ETLs to reduce the ITO work function^{117,118}. In particular, ZnO colloidal nanoparticles are used for the ETL because of their low work function, high electron mobility and optical transparency, as well as their ease of synthesis^{119,120}. However, the major challenges in using ZnO nanoparticle films as ETLs are the presence of defects with adsorbed oxygen and poor spatial distribution of the nanoparticles over a large area¹²¹⁻¹²⁵. For example, the poor spatial distribution observed in ZnO nanoparticle films is attributed to the formation of aggregates, which is highlighted in the AFM image shown in Figure 4-3. This AFM image of a knife-over-edge-coated ZnO nanoparticle film shows distinct particles with height ~ 60 nm and diameter of $\sim 300\text{--}500$ nm, indicating that severe aggregation of the ZnO nanoparticles is typical for large-scale processed films¹¹⁵. Accordingly, there is a need to develop low-defect and uniform ZnO films so as to realize high-efficiency inverted polymer solar cells.

Here, enhanced charge collection was demonstrated in inverted polymer BHJ solar cells using a ZnO -poly(vinyl pyrrolidone) (PVP) composite sol-gel film as the ETL, leading to devices that operate with laboratory-measured PCEs in excess of 8% and certified efficiencies of 7.4% under AM 1.5G illumination at 100mW cm^{-2} . The composite film, termed ‘ ZnO -PVP nanocomposite’ for clarity, consists of ZnO nanoclusters whose growth is mediated by a PVP polymeric matrix¹²⁶. ZnO -PVP nanocomposite films have been previously studied for chemical/bio-sensing applications and have the following advantages over conventional ZnO sol-gel films¹²⁷⁻¹³⁰. First, the ZnO nanocluster size and its concentration can be tuned by controlling the $\text{Zn}^{2+}/\text{PVP}$ ratio^{127,128}. Second, the

distribution of ZnO nanoclusters in the PVP polymer is uniform compared to the aggregation observed in ZnO sol-gel films without PVP^{127,128}. We hypothesized that inverted solar cells using this composite would demonstrate enhanced device performance. Furthermore, because the sol-gel processing for the ZnO-PVP nanocomposite is performed in air, this approach to depositing the ZnO ETLs is compatible with large-scale R2R processes.

The synthesis and BHJ solar cell performance of the polymer used in this study, a dithienogermole (DTG)-containing alternating conjugated donor-acceptor polymer with *N*-octylthienopyrrolodione (TPD) was used as the acceptor has been previously reported¹⁰¹. Inverted polydithienogermole-thienopyrrolodione (PDTG-TPD):[6,6]-phenyl-C₇₁-butyric acid methyl ester (PC₇₁BM) solar cells demonstrated a higher short-circuit current density (J_{sc}) and fill factor (FF) than devices with an analogous polydithienosilole-containing polymer (PDTS-TPD), leading to inverted polymer solar cells with PCEs of 7.3%¹³¹. To determine whether our ZnO-PVP nanocomposite films would enhance charge collection for inverted solar cells, inverted PDTG-TPD:PC₇₁BM BHJ solar cells was fabricated using the nanocomposite as an ETL. The following inverted device geometry was used for our study: ITO/ZnO-PVP nanocomposite/PDTG-TPD:PC₇₁BM/anode interfacial layer/Ag. For the anode interfacial layer, molybdenum trioxide (MoO₃) was used, which has a better charge extraction efficiency than more commonly used poly(ethylenedioxythiophene) doped with poly(styrene-sulfonate) (PEDOT:PSS)^{101,132-135}. While both MoO₃ and Ag are thermally evaporated in our devices, these electrode materials are compatible with R2R processing because MoO₃

can be coated from a nanoparticles suspension¹³⁶ and Ag paste can be screen printed^{16,114-116}.

4.2 Experimental Details

4.2.1 Device Fabrication

The detailed synthesis, polymer characterization and device fabrication and testing for PDTG-TPD:PC₇₁BM has been reported elsewhere¹¹⁰. PC₇₁BM used for solar cell fabrication was purchased from Solenne. Polymers and PC₇₁BM were dissolved in chlorobenzene with 1:1.5 (8 mg mL⁻¹:12 mg mL⁻¹) weight ratio and 5% volume ratio of 1,8-diiodooctane (DIO) was added as a processing additive prior to use. The ZnO-PVP nanocomposite was prepared from a precursor, in which zinc acetate dihydrate ($\text{Zn}(\text{CH}_3\text{COO})_2 \cdot 2\text{H}_2\text{O}$, Aldrich, 99.9%, 11 mg ml⁻¹) and polyvinylpyrrolidone (PVP, 2.5 mg ml⁻¹) were dissolved in ethanol. Ethanolamine was added to the precursor as a stabilizer in equal molar concentration to zinc acetate dihydrate. The ZnO-PVP precursor was spin-coated on indium tin oxide (ITO)-coated glass substrates, which were first cleaned with detergent, ultrasonicated in DI water, acetone, and isopropyl alcohol, and subsequently dried via N₂. The films were annealed at 200 °C for 40 minutes in air. After annealing and slow-cooling to room temperature, the ZnO-PVP composite films were UV-ozone treated using a UV-ozone cleaner. The film thicknesses for the ZnO-PVP composite film before and after UV-ozone treatment were 36 nm and 33 nm, respectively. The polymer-fullerene solutions were then spin-coated and the resulting film with thickness of 105 nm was annealed at 80 °C for 30 minutes. Finally, thin films of MoO₃ (10 nm) and Ag (100 nm) were deposited through shadow masks via thermal evaporation. The active area of the device was 4.6 mm².

4.2.2 Device Characterization

For PV measurements, a light mask with an area of 3.04 mm² was used to define the active area of the device. Device characterization was carried out in air after encapsulation using an Air Mass 1.5 Global (A.M. 1.5G) solar simulator with irradiation intensity of 100 mW cm⁻². The beam spot used in EQE measurement was smaller than the device area to ensure accuracy of the measurement.

4.3 Results and Discussions

4.3.1 ZnO-PVP Nanocomposite Film Characterization

Surface Morphology: The enhanced device performance with UV-ozone treated ZnO-PVP nanocomposite films is believed to be attributable to the modified surface composition promoting charge collection. The nanoscale surface morphologies of the as-prepared and UV-ozone treated ZnO-PVP nanocomposite films were investigated by atomic force microscopy (AFM). Fig. 4-4a and b shows the three-dimensional surface topography images for the nanocomposite film before and after UV-ozone treatment. The ZnO-PVP nanocomposite film shows an increase in r.m.s. roughness from 7.07 nm to 9.18 nm following UV-ozone treatment, suggesting that PVP is removed with this treatment, leaving the ZnO nanoclusters exposed at the surface. This removal of the PVP is more clearly shown in the AFM phase images in Fig. 4-4c and d. For the nanocomposite film without UV-ozone treatment, no nanoclusters can be observed, indicating that the surface is covered by a thin layer of PVP. However, the phase image for the UV-ozone treated ZnO-PVP nanocomposite film shows that the PVP domain size has been reduced to 50-100 nm and that the ZnO nanoclusters are now exposed on the surface. The PVP-rich and ZnO nanocluster-rich surfaces of the nanocomposite

films before and after UV-ozone treatment, respectively, are shown schematically in Fig. 4-4e,f.

To determine whether the removal of PVP from the nanocomposite film surface altered the film thickness, step-height measurements were taken for the films before and after UV-ozone treatment. The average thickness of the nanocomposite film shows negligible change after 10 min UV ozone treatment, which provides further evidence that PVP was removed only at the surface of the ZnO-PVP nanocomposite film upon UV-ozone treatment. Furthermore, to illustrate the surface morphology of the ZnO-PVP nanocomposite films before and after UV-ozone treatment, 5- μ m-scale phase images are shown in Fig. 4-5. These images show that the removal of PVP by UV-ozone treatment significantly alters the surface morphology of the nanocomposite film. This change in surface morphology from being PVP-rich before UV-ozone treatment to ZnO-rich after treatment supports our idea that the removal of PVP from the nanocomposite film by UV-ozone treatment leads to improved charge collection in our inverted polymer solar cells due to better electronic coupling between the ZnO nanoclusters within the nanocomposite film and PC₇₁BM in the active layer.

Chemical Composition: To further confirm that the compositional changes determined from the AFM data were due to the removal of PVP, X-ray photoemission spectroscopy (XPS) was performed on the ZnO-PVP nanocomposite films. Considering the period of UV-ozone treatment required to optimize the device performance, it is believed that some changes in the chemical composition of ZnO might be plausible. The core level XPS spectra for the C 1s, O 1s, and Zn 2p were measured for the as-prepared and 10 min UV-ozone treated ZnO-PVP nanocomposite films. The binding

energies were calibrated by taking the C 1s peak (284.6 eV) as a reference. The O 1s XPS spectra for as-prepared and UV-ozone treated ZnO-PVP nanocomposite films are shown in Fig. 4-6a. UV-ozone treatment increased the relative magnitude of the peak at 531.4 eV (corresponding to the oxygen atoms bonded to the zinc in the ZnO matrix^{127,128,137}) by ~37%. Thus the number of Zn-O bonds in the wurtzite structure of ZnO at the surface of the film is increased. UV-ozone treatment also increased the relative magnitude of the peak at ~ 530.0 eV, which corresponds to O⁻² ions present in the porous ZnO clusters, but not chemically bonded to zinc in the ZnO wurtzite structure. Fig. 4-6b shows the Zn 2p3/2 XPS spectra for the as-prepared and UV-ozone treated ZnO-PVP nanocomposite films. The intensity of the peak at 1021.6 eV, which corresponds to the Zn-O bonds^{127,128,137,138}, increases after UV-ozone treatment. These results are in agreement with the result from the O 1s XPS spectra. Based on the O 1s and Zn 2p XPS spectra, we conclude that the chemical composition of the ZnO nanoclusters on the surface of the nanocomposite film has become oxygen-rich after UV-ozone treatment.

The atomic concentrations of carbon, oxygen, and zinc in the as-prepared and 10 min UV-ozone treated ZnO-PVP nanocomposite films based on the C 1s, O 1s, and Zn 2p XPS spectra are summarized in Fig. 4-6c. The atomic concentration of carbon from the PVP in the nanocomposite is significantly reduced by UV-ozone treatment (from 38.2% to 15.7%). Conversely, the atomic concentrations of oxygen and zinc present in the nanocomposite film both increase from 28.5% and 33.3% for the untreated film to 31.6% and 52.6%, respectively, for the treated film. The relatively smaller increase in oxygen atomic concentration compared to zinc is due to the competition between the

increases in oxygen content coming from UV-Ozone treatment and the decrease in oxygen content coming from the removal of PVP. These results strongly support our assertion that UV-ozone treatment removes PVP from the surface of the ZnO-PVP nanocomposite film.

Optical Transparency: Finally, the effect of UV-ozone treatment on optical transmission for the as-prepared and treated ZnO-PVP nanocomposite films was studied. UV-vis-NIR transmission spectra for these films are shown in Supplementary Fig. 4-7. Following UV-ozone treatment, a 6% to 10% increase in transmission across the entire visible spectrum was observed in the nanocomposite film. This increase in optical transmission was attributed to the changes in the effective index of refraction of the nanocomposite film upon UV-ozone treatment. It should be noted that the increase in optical transparency is less than the enhancement observed in J_{sc} for inverted solar cells with UV-ozone treated ZnO-PVP nanocomposite films. Therefore, although the increase in optical transparency contributes to the enhancement in J_{sc} , the improved charge collection due to enhanced electronic coupling between ZnO nanoclusters in the nanocomposite film and PC₇₁BM in the active layer is primarily responsible for this enhancement.

4.3.2 Inverted Polymer Photovoltaic Cell with ZnO-PVP Nanocomposite ETL

The photo J - V characteristics for inverted PDTG-TPD:PC₇₁BM solar cells were measured under AM 1.5G solar illumination at 100 mW cm⁻². The photovoltaic (PV) performance results for the inverted cells with ZnO-PVP nanocomposites are shown in Fig. 4-8. On initial light exposure the inverted solar cells had a low FF of 25.5% and J_{sc} of 10.9 mA cm⁻². With continuous illumination, device performance was enhanced significantly over time¹³⁹. After ~10 min of light soaking, an enhanced FF of 63.7% and

J_{sc} of 12.9 mA cm⁻² were obtained, resulting in an average PCE of 7.0%. Previously, we reported inverted PDTG-TPD-based polymer solar cells with FF of ~68% using colloidal ZnO NPs as ETL¹⁰¹. We suspected that by using ZnO-PVP composite as the ETL, the ZnO-PVP surface would be compositionally rich in PVP, creating a contact barrier between the ZnO nanoclusters and PC₇₁BM lead to the lower FF of our present devices.

To ensure a good contact between the ZnO nanoclusters and PC₇₁BM, we performed UV-ozone treatment on the ZnO-PVP nanocomposite films to remove PVP from the surface. Previous work has shown that UV-ozone treatment can remove PVP on colloidal nanoparticle film surfaces¹⁴⁰. The removal of PVP did not alter the size, shape, or distribution of the nanoclusters in the films^{140,141}. Based on these findings, we believed that the UV-ozone treatment would improve electronic coupling between photo-active layer and ZnO nanoclusters.

The photo *J-V* characteristics for the inverted PDTG-TPD:PC₇₁BM solar cells with UV-ozone treated ZnO-PVP nanocomposites are shown in Fig. 4-9a. All devices were tested under initial light exposure, and no additional light soaking was applied to the devices. The ZnO-PVP nanocomposite films were UV-ozone treated for 5, 10, 20, and 30 min, leading to significant enhancements in J_{sc} and FF for the inverted PDTG-TPD:PC₇₁BM solar cells compared to cells with as-prepared nanocomposite films. Table 4-1 summarizes the device performance for inverted solar cells with treated ZnO-PVP nanocomposite films. UV-ozone treating the ZnO-PVP nanocomposite films for 10 min led to an optimal device with enhancements in both J_{sc} and FF compared to the light-soaked devices without UV-ozone treatment, resulting in an average PCE of 8.1%. This average PCE of 8.1 ± 0.4% is based on measurement from 102 fabricated solar

cells. Our best device had a J_{sc} of 14.4 mA cm⁻², V_{oc} of 0.86 V, FF of 68.8% and PCE of 8.5%. For devices with ZnO-PVP nanocomposite films that had been UV-ozone treated for less than or more than 10 min, a reduction in FF was observed. For the shorter treatment, we attribute this reduction in FF to incomplete removal of the PVP from the surface of the composite film. For the longer treatment, excess oxygen is present on the ZnO film surface, which reduces the electron extraction efficiency. Based on these findings, we conclude that removal of extra PVP from the ZnO-PVP nanocomposite film surface by UV-ozone treatment greatly enhances the charge collection efficiency of these devices.

To confirm the accuracy of the photo J - V measurements, the external quantum efficiency (EQE) spectra for the solar cells with as-prepared and 10 min UV-ozone treated ZnO-PVP nanocomposite films were measured; these are compared in Fig. 4-9b. An enhanced efficiency is observed throughout the full spectral range from 350 – 700 nm for cells with the UV-ozone treated ZnO-PVP nanocomposite films when compared to cells without UV-ozone treatment. The maximum EQE for the optimized inverted PDTG-TPD:PC₇₁BM solar cell with UV-ozone treated nanocomposite films was 73.6%. The J_{sc} value was then calculated by integrating the EQE data with the AM 1.5G spectrum. The calculated J_{sc} value of 14.5 mA cm⁻² is in good agreement with the directly measured J_{sc} value.

To study the difference in light soaking behavior for inverted PDTG-PC₇₁BM solar cells with either as-prepared or UV-ozone treated ZnO-PVP nanocomposite ETL, dark J - V measurements were taken on the inverted devices before and after AM 1.5G solar illumination. Fig. 4-10 shows the results for inverted devices measured with either no

light soaking or with light soaking using filters to block incident light below 600 nm or 350 nm wavelength. The devices were encapsulated and stored in the dark prior to measurements. The dark J-V curves for the device before light soaking and after light soaking using the 600 nm filter are identical, showing low current density values for the inverted devices. Therefore, long wavelength light soaking has no effect on device performance. However, when the inverted device is light soaked using the 350 nm long-pass filters, a significant enhancement in dark current density is observed. The enhanced dark current density matches the values observed for typical dark J-V measurements of these devices under forward bias. Therefore, the inverted solar cells with UV-ozone treated ZnO-PVP shows immediate enhancement in conductivity upon illumination of short wavelength light. The fact that we see optimized performance during the initial J-V scan for the UV-ozone treated device indicates that the soaking time required is significantly less than that required for the untreated devices.

Encapsulated devices with UV-ozone treated ZnO-PVP nanocomposite films were then sent to NEWPORT Corporation for certification. The photo J-V characteristics and the corresponding solar cell parameters are shown in Fig. 4-11. A PCE of 7.4 +/- 0.2% was certified for the devices. Although this certified efficiency is 9% less than that measured in our laboratory because of a reduction in J_{sc} and FF in the certified device, we attribute the reduction in PCE in the certified cells to degradation because of a non-optimized encapsulation process. The devices were retested in our laboratory after certification and we obtained an efficiency (7.2%) comparable to the certified results.

We sought to further investigate the effect of UV-ozone treatment on ZnO-PVP composite films and the corresponding photovoltaic device stability. As shown in Fig. 4-

12, after light soaking, the performance of the device with untreated ZnO-PVP nanocomposite ETL reduced significantly over time, showing that the enhancement in J_{sc} and FF due to light soaking was only temporary¹³⁹. In contrast, the device performance observed for solar cells with UV-ozone treated ZnO-PVP nanocomposite ETLs had much better stability. In fact, we observed no measureable changes in J_{sc} , FF, or PCE over a period of one month provided that the encapsulated devices were stored in a nitrogen glove box. Thus, UV-ozone treatment of the ZnO-PVP nanocomposite films provides enhanced stability in the inverted solar cells.

4.3 Concluding Remarks

To conclude, improved charge collection efficiency has been demonstrated in inverted PDTG-TPD BHJ solar cells using a UV-ozone treated ZnO-PVP nanocomposite film as the ETL to obtain organic polymer solar cells with PCEs in excess of 8% under A.M.1.5G illumination at 100 mW cm⁻². The use of PVP as an organic capping molecule and polymeric matrix for ZnO produced electron-transporting nanocomposite films, which had excellent film-forming characteristics. We found that UV-ozone treatment was required to remove PVP from the surface of the film, and consequently exposed the ZnO nanoclusters to the film surface. Using our UV-ozone treated ZnO-PVP nanocomposite ETL, inverted PDTG-TPD solar cells with laboratory-measured PCE higher than 8% have been realized due to improved charge collection by the nanocomposite film.

Table 4-1. Average solar cell performance for inverted PDTG-TPD:PC₇₁BM devices with 5, 10, 20, or 30-minute UV-ozone treated ZnO-PVP composite ETLs under initial AM 1.5G solar illumination¹⁴².

UV-ozone treatment time	J_{sc} (mA cm ⁻²)	V_{oc} (V)	FF (%)	Average PCE (%)	Best PCE (%)
5 min	13.9±0.1	0.85±0.005	56.0±3.8	6.6±0.5	7.1
10 min	14.0±0.4	0.86±0.003	67.3±1.5	8.1±0.4	8.5
20 min	14.1±0.2	0.86±0.003	64.8±0.8	7.8±0.2	8.0
30 min	14.0±0.1	0.86±0.003	61.9±1.6	7.5±0.3	7.6

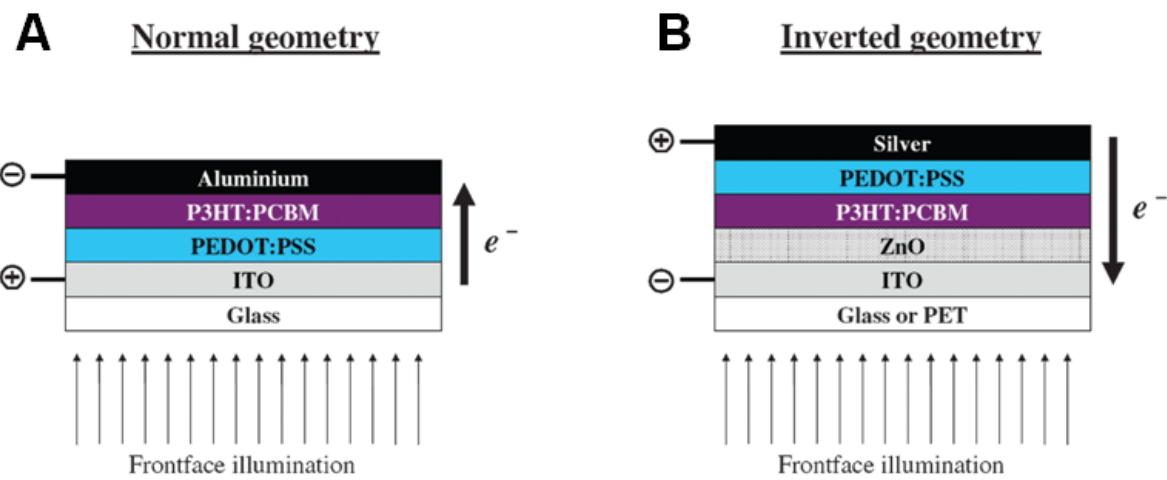


Figure 4-1. The normal and inverted device geometries for P3HT:PCBM solar cells. A) The normal device geometry. B) The inverted device geometry¹¹⁶.

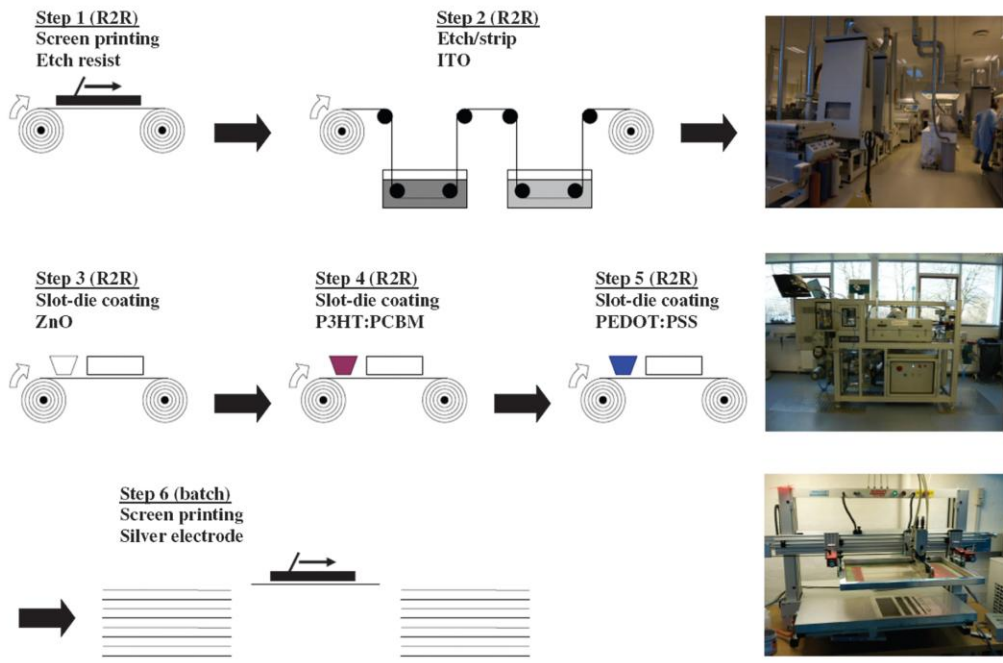


Figure 4-2. An illustration of the process and the six processing steps employed during fabrication of the R2R coated modules. The modules utilize the inverted device geometry¹¹⁶.

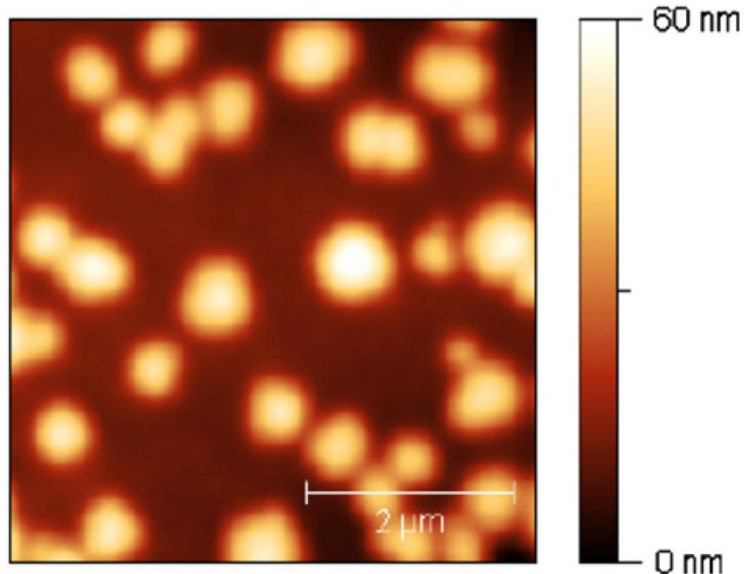


Figure 4-3. AFM image (measuring $5 \times 5 \mu\text{m}^2$) of a knife-over-edge coated ZnO nanoparticle film used in the fabrication of large-scale R2R-processed modules¹¹⁵.

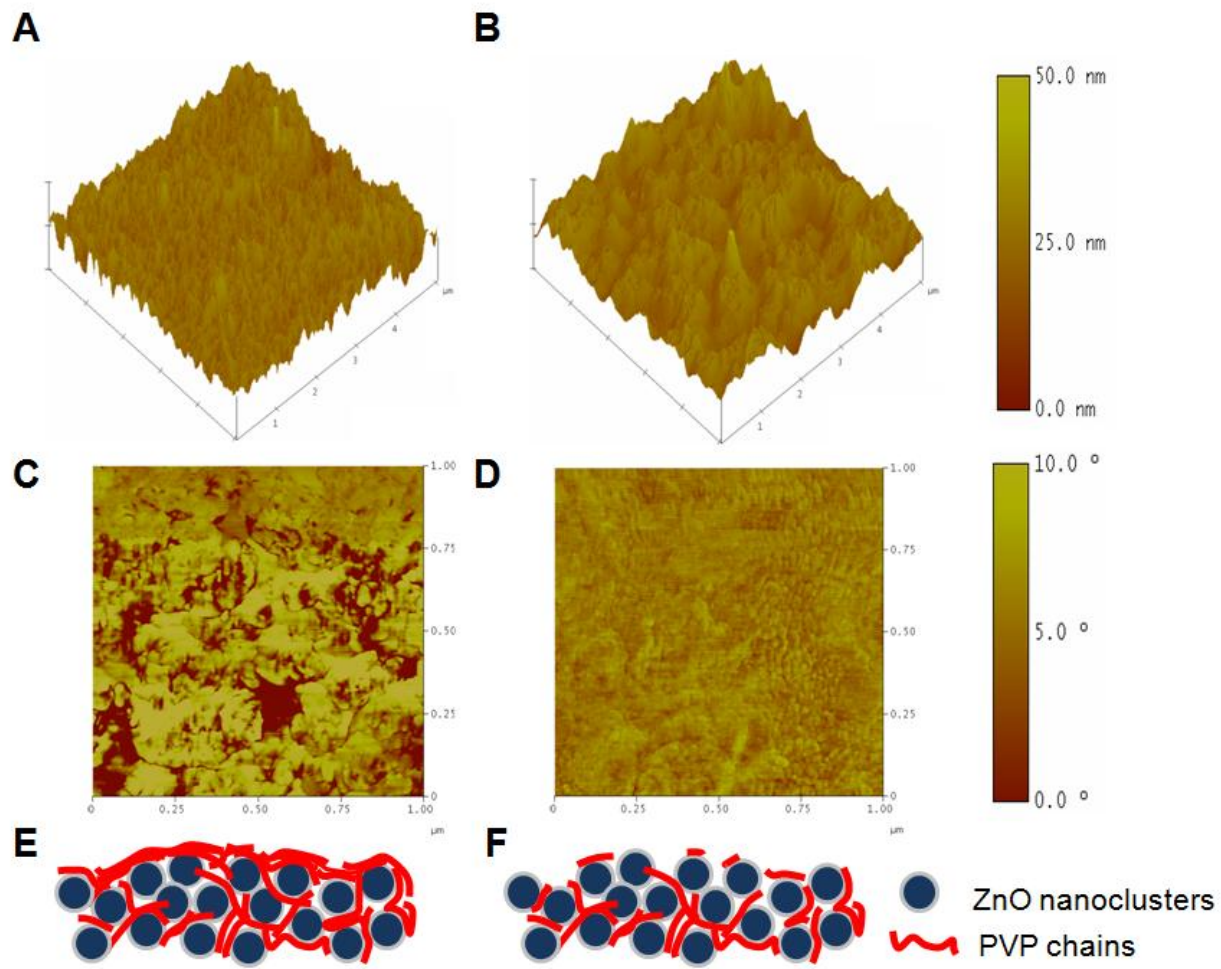


Figure 4-4. Tapping mode AFM images for as-prepared and 10-min UV-ozone treated ZnO-PVP nanocomposite films. Appropriate scales are shown on the right. A) 3-D topography images for the as-prepared composite film. B) 3-D topography images for the UV-ozone treated composite films. C) Phase image for the as-prepared composite film. D) Phase image for the UV-ozone treated composite film. E) Schematic image for the as-prepared composite film showing a PVP-rich surface. F) Schematic image for the UV-ozone treated composite film showing a ZnO-rich surface¹⁴².

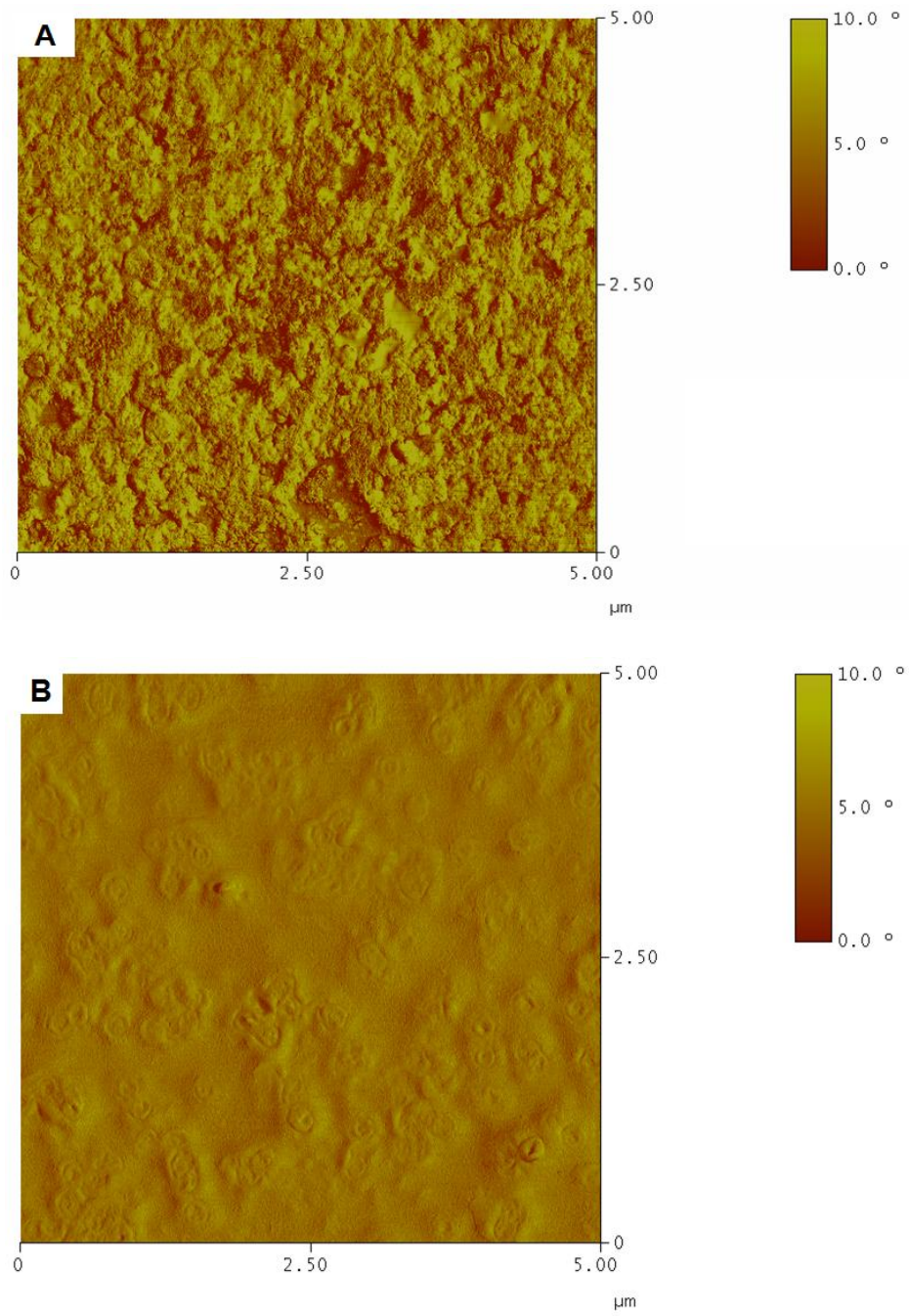


Figure 4-5. Tapping-mode AFM phase images for ZnO-PVP nanocomposite films before and after UV-ozone treatment (5 μm scale size). A) As-prepared composite films. B) 10-minute UV-ozone treated composite film¹⁴².

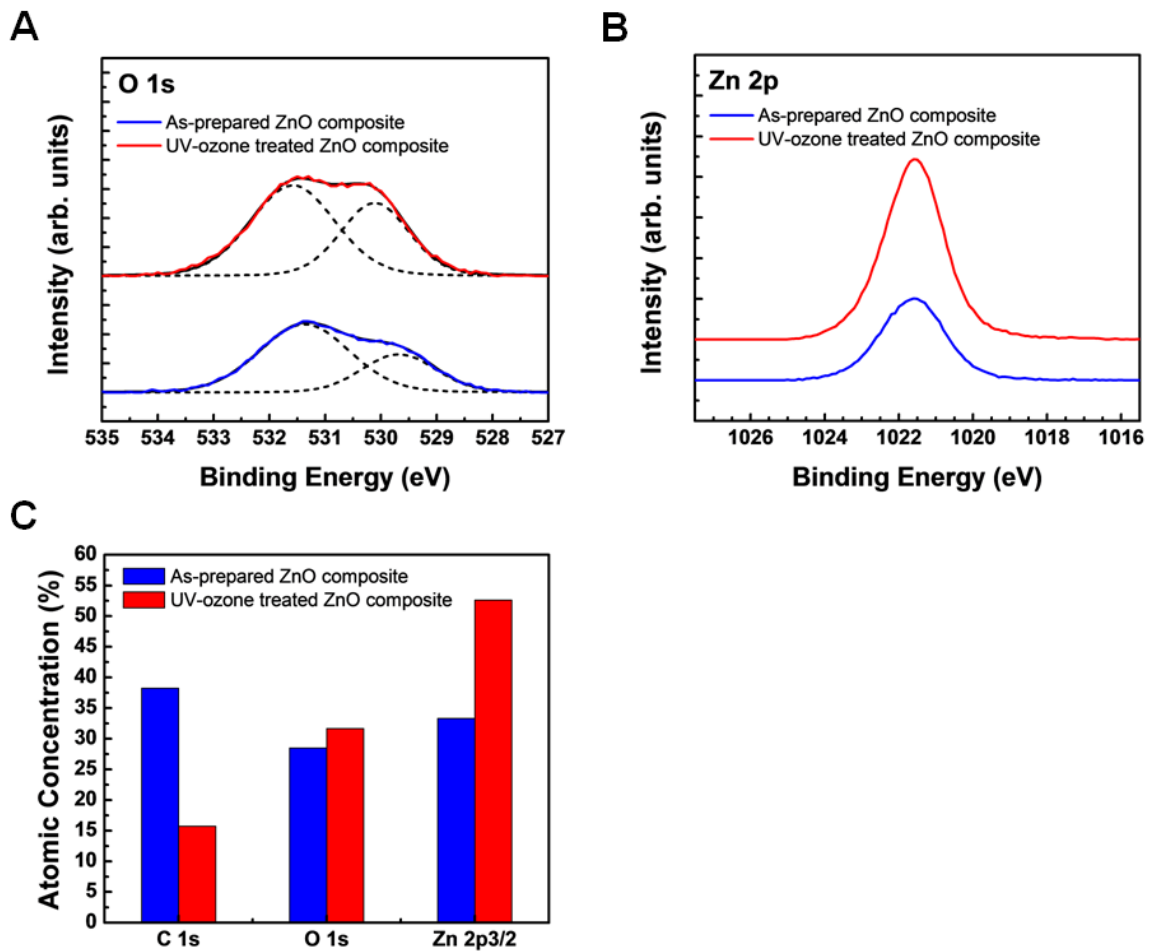


Figure 4-6. X-ray photoemission spectra (XPS) for the as-prepared and 10-minute UV-ozone treated ZnO-PVP nanocomposite films. A) O1s narrow-scan XPS spectra. B) Zn 2p XPS narrow-scan XPS spectra. C) Atomic concentration of C, Zn, and O before and after UV-ozone treatment based on the corresponding XPS spectra¹⁴².

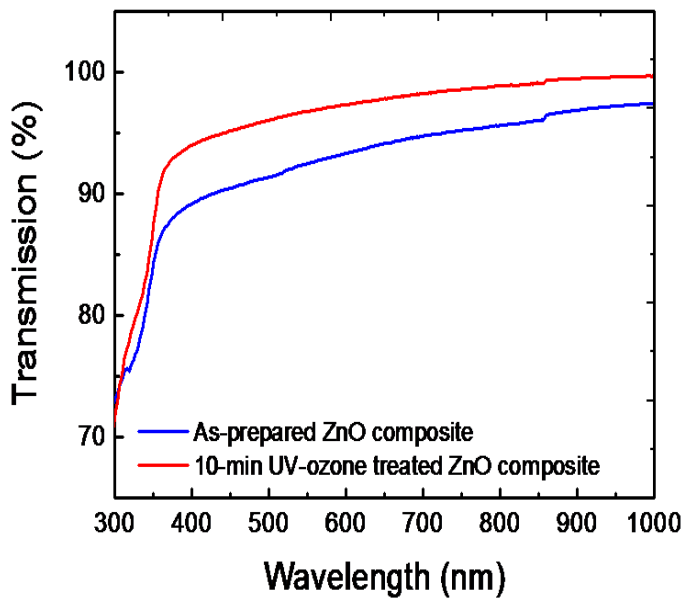


Figure 4-7. UV-visible-NIR transmission spectra for the as-prepared and 10-minute UV-ozone treated ZnO-PVP nanocomposite films¹⁴².

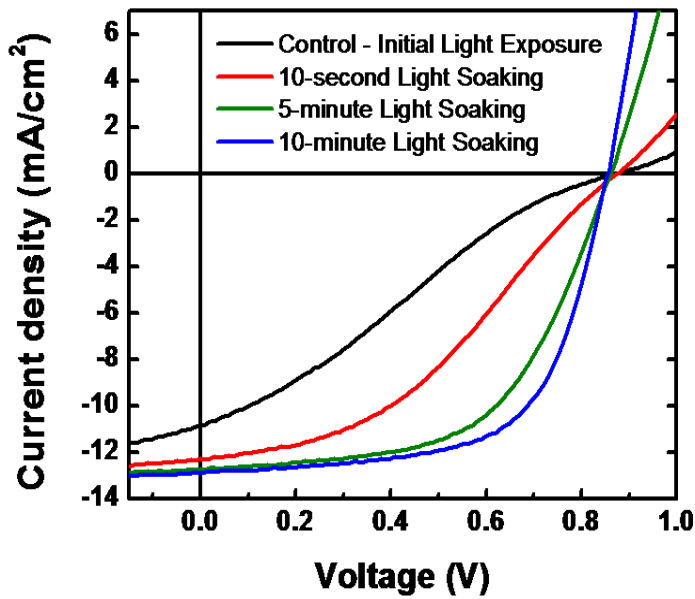


Figure 4-8. Photo J-V characteristics for inverted PDTG-TPD:PC₇₁BM solar cells highlighting the effect of prolonged light soaking on device performance under AM 1.5G solar illumination at 100 mW cm⁻²¹⁴².

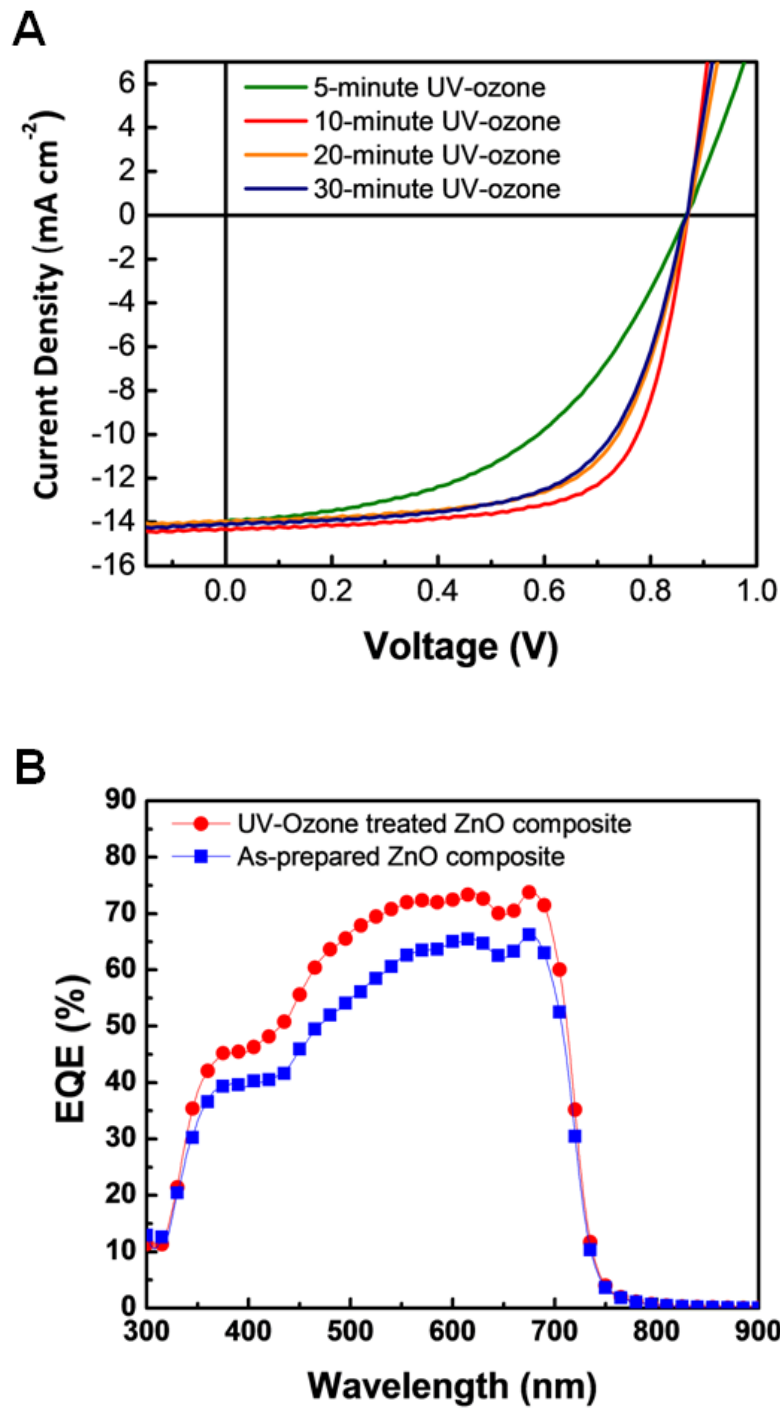


Figure 4-9. Photo J-V characteristics and EQE spectra for inverted PDTG-TPD:PC₇₁BM solar cells with UV-ozone treated ZnO-PVP nanocomposite ETL for various treatment times. A) Photo J-V characteristics for the devices. B) Corresponding EQE spectra for the device with 10-minute UV-ozone treated ZnO-PVP nanocomposite films. The EQE spectrum for the device with as-prepared composite films is shown for comparison¹⁴².

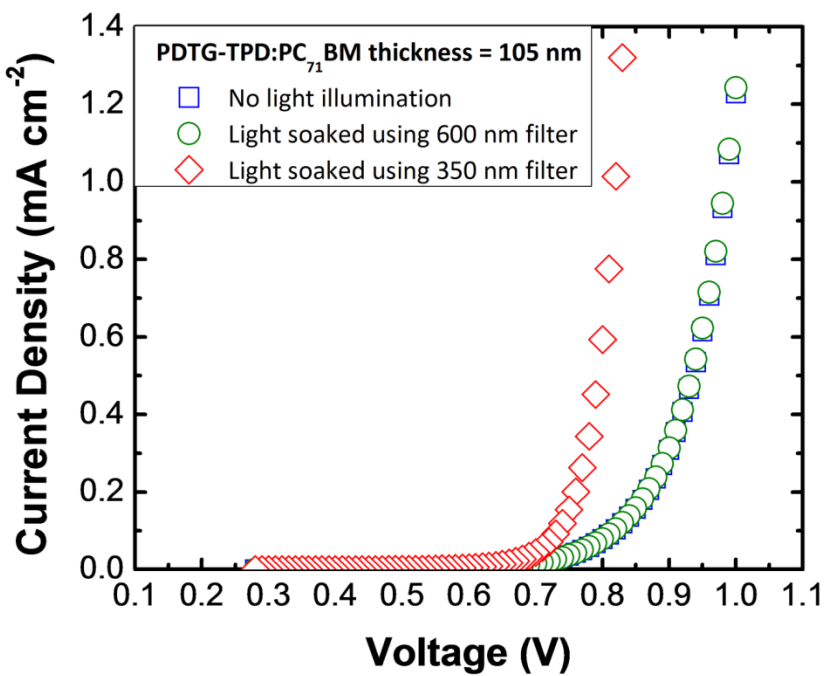


Figure 4-10. Dark J-V characteristics for inverted PDTG-TPD:PC₇₁BM solar cells with UV-ozone treated ZnO-PVP nanocomposite ETL measured as-is and after being light soaked using either a 600 nm or 350 nm band-pass filter¹⁴².

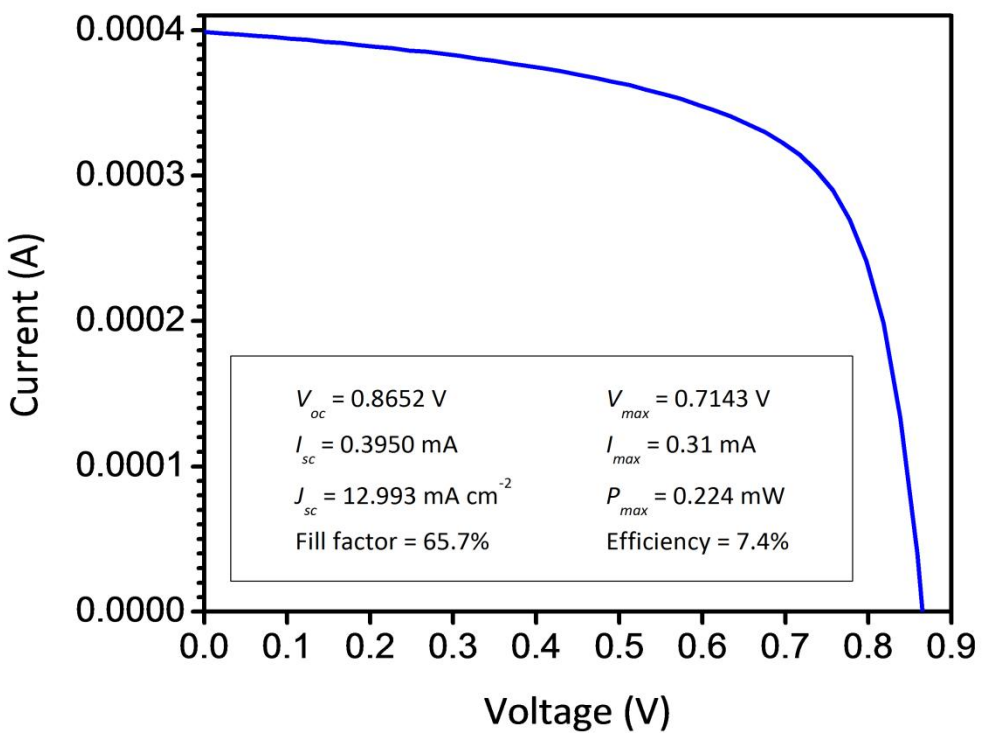


Figure 4-11. Certified *I*-*V* characteristics for an inverted PDTG-TPD:PC₇₁BM solar cell with 10-minute UV-ozone treated ZnO-PVP nanocomposite ETL. The device was certified by NEWPORT Corporation¹⁴².

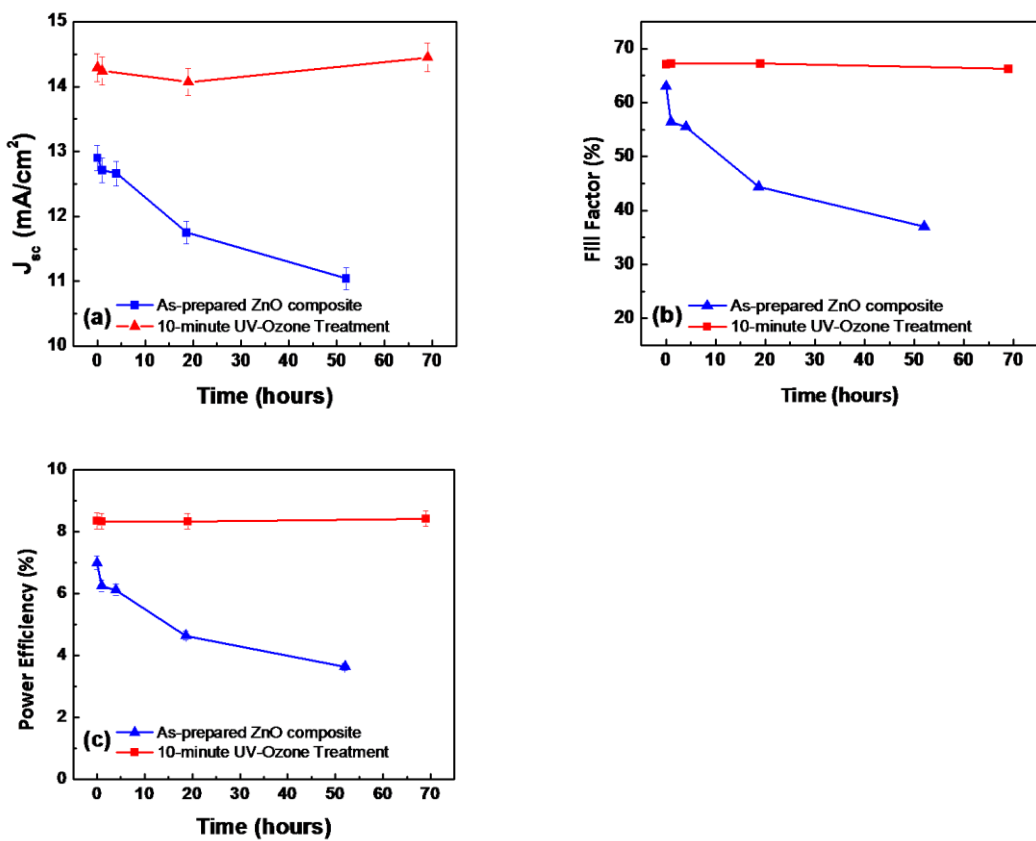


Figure 4-12. Solar cell parameters versus time for encapsulated inverted PDTG-TPD:PC₇₁BM with as-prepared and 10-minute UV-ozone treated ZnO-PVP nanocomposite ETLs. A) Short-circuit current density (J_{sc}) vs. time. B) Fill factor (FF) vs. time. C) Power conversion efficiency (PCE) vs. time¹⁴².

CHAPTER 5

LOSS MECHANISMS IN THICK-FILM LOW-BANDAP POLYMER SOLAR CELLS

5.1 Introductory Remarks

Polymer BHJ solar cells, which have the potential to provide low cost energy harvesting, are receiving much attention in research and development^{109,114,116,143}. In Chapter 4, inverted PDTG-TPD:PC₇₁BM solar cells with over 8% power conversion efficiency was demonstrated, which is crucial for demonstrating the viability of this technology for large-scale R2R processing^{142,144}. Despite this performance for laboratory-scale inverted devices, the cell geometry is not the only factor determining their compatibility for large-scale manufacturing. Another key factor for large-scale R2R processing of polymer solar cells is the active layer thickness required to ensure high manufacturing yields in the PV modules¹⁴⁵. Most high efficiency laboratory-scale devices have an active layer that is too thin for large-scale R2R processing. Krebs and coworkers have shown that polymer:fullerene active layers deposited by slot-die coating have a high surface roughness and non-uniform film thickness due to the large difference between the wet film thickness and dry film thickness¹⁴⁵. This high surface roughness and non-uniform film thickness for the active layer leads to a lower yield of serially-connected polymer solar cells. To address this issue, a larger solid concentration of polymer and fullerene is used in solution. As a result, the active layer film thickness for the R2R processed PV module is typically around 200 nm, which is larger than the film thickness employed in optimized laboratory-scale polymer solar cells. Therefore, obtaining high efficiency devices with active layers thicker than 200 nm is critical for commercialization^{115,145}.

In addition to the thickness requirement associated with large-scale R2R processing, increased active layer thickness is also required for optimal light harvesting to produce high efficiency polymer solar cells. Presently, solar cells with enhanced light absorption have been demonstrated by employing low bandgap polymers with optical bandgap between 1.2 and 1.7 eV^{95,101,113,146,147}. To obtain a high FF in these high efficiency cells, with the exception of poly(3-hexylthiophene) (P3HT) BHJ solar cells, the active layer used is typically less than 100 nm. However, due to optical interference effects, a high EQE can only be obtained in these devices when the thickness exceeds 200 nm¹⁴⁸. Therefore, despite their high power conversion efficiencies (PCEs), low bandgap polymer solar cells do not take advantage of the true light harvesting potential of the polymer used in such thin-film devices. The average EQE is expected to increase for solar cells with a thicker active layer due to enhanced light absorption and optimum optical interference. Therefore, to meet the large-scale R2R processing requirement and ultimately realize optimum light absorption, high efficiency polymer solar cells with a thicker active layer must be demonstrated.

In the past, demonstrating high efficiency polymer solar cells with a thick active layer has been a challenge. Previous work has focused on obtaining high hole mobilities in low bandgap polymers when blended with fullerene. This has been achieved by developing novel polymer structural designs and by improving the nanoscale morphology of polymer:fullerene BHJ films^{149,150}. The improved carrier transport helps alleviate the buildup of photogenerated carriers in devices with thicker active layer, which decreases the probability of carrier recombination and, consequently, enhances the carrier collection efficiency¹⁴⁹⁻¹⁵⁴. While this approach has been successful for

polymer solar cells such as poly(3-hexylthiophene):[6,6]-phenyl-C₆₁ butyric acid methyl ester (P3HT:PC₆₁BM), solar cells employing low bandgap conjugated polymers with fused donor–acceptor moieties show significant reductions in FF and PCE with increasing the BHJ film thickness despite showing record efficiencies for thin-film devices^{117,155,156}. Minimizing this FF reduction and, consequently, achieving high efficiency in low bandgap polymer solar cells with thicker active layer is particularly important for the development of low-cost, high efficiency polymer solar cell for commercial application.

In this chapter, the thickness dependence of the efficiency in polymer solar cells employing the low-bandgap polymer PDTG-TPD is studied¹⁰¹. Previous work reported that the PCEs of these cells can be as high as 8.1% with an active layer thickness of about 100 nm^{142,144}. Increasing the active layer thickness (L) up to 200 nm yielded devices with a PCE above 8.0%, which shows the viability of the PDTG-TPD:[6,6]-phenyl-C₇₁ butyric acid methyl ester (PC₇₁BM) system for large-scale R2R processing. For devices with an active layer thickness > 200 nm, a marked reduction in FF and PCE were observed. On the contrary, similar P3HT:PC₆₁BM polymer solar cells showed almost no reduction in FF for devices with active layer thickness up to 453 nm. Interestingly, similar space-charge-limited (SCL) hole mobility values were obtained for both polymer:fullerene BHJ films despite the difference in fill factor behavior with increasing active layer thickness. These results are interpreted as follows: the broader absorption band for the PDTG-TPD:PC₇₁BM system leads to increased charge carrier generation and increased space-charge buildup in the photoactive layer compared to P3HT:PC₆₁BM. The onset of space charge accumulation coincides with increased

carrier recombination loss in the photoactive layer, which results in a significant FF reduction in devices with thicker active layer¹⁵⁰. Analysis on the incident light intensity dependence of the FF, as well as an analysis of SCL photocurrent in PDTG-TPD:PC₇₁BM solar cells further support this hypothesis¹⁵⁷. In addition to space-charge effects, the reduced FF observed in thick PDTG-TPD:PC₇₁BM solar cells is also attributed to a low carrier lifetime as compared to similar P3HT:PC₆₁BM devices. Overall, these results indicate that recombination loss due to space-charge effects and low carrier lifetime limits the performance of thick film low-bandgap polymer solar cells.

5.2 Experimental Details

5.2.1 Device Fabrication

The detailed synthesis, purification, and polymer characterization for PDTG-TPD has been reported in the work by Amb and coworkers¹⁰¹. P3HT was purchased from Rieke Metals, Inc. Both PC₆₁BM and PC₇₁BM used for solar cell fabrication were purchased from Solenne. For the inverted PDTG-TPD-based devices, the polymer and PC₇₁BM were dissolved in chlorobenzene with 1:1.5 weight ratio and 5% volume ratio of 1,8-diiodooctane (DIO) was added as a processing additive to both solutions. The ZnO-PVP nanocomposite electron transporting layer, whose solution processing was discussed in Chapter 4, was spin-cast on indium tin oxide (ITO)-coated glass substrates. The ITO substrates were first cleaned with detergent, ultrasonicated in DI water, acetone, and isopropyl alcohol, and subsequently dried via N₂. The polymer-fullerene solutions were then spin-coated at various spin speeds to control active layer thickness and the resulting films were annealed at 80 °C for 30 minutes. Finally, thin films of MoO₃ (4 nm) and Ag (100 nm) were deposited through shadow masks via thermal evaporation. The active area of the device was 4.6 mm². For the P3HT:PC₆₁BM

solar cells, P3HT and PC₆₁BM were dissolved in chlorobenzene with 1:1 (8 mg mL⁻¹:12 mg mL⁻¹) weight ratio. Thermally evaporated films of MoO₃ (Sigma Aldrich, 4 nm) and bathocuproine (BCP, 5 nm) were used for the anode and cathode interlayers, respectively. The active layer thickness was controlled by varying the spin-coating speed. Hole-only devices were fabricated to extract the space-charge limited hole mobility. The device structures for the polymer solar cells and hole-only devices fabricated in this chapter is shown in Figure 5-1.

5.2.2 Device Characterization

Current density-voltage measurements were carried out in air after encapsulation using a Keithley 4200 semiconductor system. For light intensity-dependent J-V measurements, neutral density filters were used to control the incident light intensity from the AM 1.5G solar simulator. For field-dependent EQE measurements, a bias was applied to the device using a current amplifier. For all EQE measurements, the beam spot used was smaller than the device area to ensure accuracy of the measurement.

5.3 Results and Discussions

5.3.1 PDTG-TPD:PC₇₁BM Solar Cell Performance

Figure 5-2 shows the photocurrent density–voltage (J-V) characteristics and the corresponding external quantum efficiency (EQE) spectra for inverted PDTG-TPD:PC₇₁BM solar cells with 105 nm, 204 nm, and 258 nm-thick active layers. The short-circuit current density (J_{sc}) for the solar cells increases with increasing active layer thickness due to enhanced light absorption, with the highest J_{sc} of 16.1 mA cm⁻² obtained for the device with an active layer thickness of 258 nm. The integrated current density from the EQE spectra, shown in Figure 5-2, is consistent with the measured J_{sc} with only 5% deviation. The difference in the EQE spectra is due to the optical

interference effects between the incident light and light reflected from the Ag back electrode¹⁴⁸. For devices with $L \geq 200$ nm, the interference effects no longer affect the photocurrent density of the device and the active layer absorbs almost all the incident light below 700 nm, resulting in EQEs above 70% from 400 nm to 700 nm.

Table 5-1 summarizes the average solar cell parameters for the PDTG-TPD:PC₇₁BM devices with an active layer thickness varying from 90 nm to 409 nm. The reduction in FF observed for PDTG-TPD solar cells with increasing active layer thickness is the major factor limiting the device performance. A power conversion efficiency (PCE) of 7.9% is obtained for the device with a 105 nm thick active layer, which is consistent with the results shown in Chapter 4. The efficiency remains constant for devices with $L \leq 204$ nm, with an average PCE of 8.2% being obtained for devices with an active layer thickness of 204. Above 200 nm, the FF reduction becomes significant, from 69% in the 105 nm film to 42% in the 409 nm film. The performance for PDTG-TPD:PC₇₁BM solar cells was then compared to similar devices based on P3HT:PC₆₁BM, which is a well studied material system for investigated the active layer thickness dependence of the efficiency for polymer solar cells^{149,151}. The photo J-V and EQE curves for P3HT:PC₆₁BM devices with active layer thickness from 100 nm to 453 nm are shown in Figure 5-3. Although the J_{sc} increased in the devices due to enhanced light absorption in the P3HT:PC₆₁BM BHJ film, the overall enhancement in J_{sc} was only ~23–24% when the active layer thickness was increased from 100 nm to 453 nm. This small increase in J_{sc} can be attributed to narrow-band absorption of P3HT and, consequently, the limited fraction of the solar spectrum absorbed by the P3HT:PC₆₁BM solar cells. As shown in Table 5-2, the fill factor for these devices remained above 65%

despite increasing the thickness from 100 nm to 453 nm. This is in stark contrast to the results obtained for the PDTG-TPD:PC₇₁BM solar cells. The high FF obtained for these devices is characteristic of the balanced *e* and *h* mobility in the active layer, as well as the ability to efficiently extract photogenerated charge carriers. The low rate of hole generation in the thick-film P3HT:PC₆₁BM solar cells, as indicated by the small enhancement in J_{sc} , helps to prevent space-charge from accumulating within the active layer. The average FF and average EQE versus active layer thickness for both PDTG-TPD:PC₇₁BM and P3HT:PC₆₁BM solar cells is summarized in Figure 5-4. Here, ‘average EQE’ refers to external quantum efficiency for the solar cell averaged over the wavelength range corresponding to the EQE spectra. For PDTG-TPD solar cells, a high average FF can only be obtained for devices with $L \leq 204$ nm. In contrast, a FF $\geq 65\%$ was observed for P3HT:PC₆₁BM solar cells with $L \leq 453$ nm. In terms of the average EQE, only thick-film PDTG-TPD:PC₇₁BM solar cells with $L \geq 204$ nm was capable of reaching an average EQE of 65%.

In previous work, the reduction in FF for thick-film devices was attributed to polymer solar cells with low carrier mobility such as MDMO-PPV:PC₆₁BM¹⁵⁰. The low mobility increases the chances of carrier recombination and therefore reduces the FF. To confirm that low carrier mobility was not responsible for the reduction in FF, the SCL hole mobility was extracted from *J-V* measurements for PDTG-TPD:PC₇₁BM single-carrier devices using the Mott-Gurney Law outlined in Chapter 2 and compared those values with the mobility values for P3HT:PC₆₁BM solar cells (see Figure 5-5). The hole mobility values for the 105 nm and 409 nm-thick PDTG-TPD:PC₇₁BM devices were $3.4 \times 10^{-3} \text{ cm}^2 \text{ V}^{-1} \text{ s}^{-1}$ and $2.3 \times 10^{-3} \text{ cm}^2 \text{ V}^{-1} \text{ s}^{-1}$, respectively. These values are comparable

with hole mobility values found for optimized P3HT:PC₆₁BM solar cells reported in the literature^{149,150}. It suggests that the reduction in device performance in PDTG-TPD:PC₇₁BM solar cells is not due to the mobility since both PDTG-TPD and P3HT have the same mobilities.

To determine the root cause for the reduction in FF observed in thick-film PDTG-TPD:PC₇₁BM solar cells, the EQE spectra for the thin-film and thick-film devices were measured under different values of internal electric field¹⁵⁸. Figure 5-6 shows the field-dependent EQE spectra for devices with 105 nm, 204 nm, 258 nm, and 409 nm-thick active layer, respectively. Here, the internal electric field (E) was approximated as $E = (V_{oc} - V)/L$. For devices an active layer thickness ≤ 204 nm, increasing the applied field from 20 kV cm⁻¹ to 70 kV cm⁻¹ leads to a uniform enhancement in EQE across the entire spectral range. The increased applied field enhances the extraction of photogenerated charges equally across the EQE spectrum. Interestingly, for devices with $L > 204$ nm, a stronger field-dependent enhancement in EQE is observed in the spectral range from 500 to 750 nm when the applied field is increased from 20 kV cm⁻¹ to 70 kV cm⁻¹. This wavelength range corresponds to the absorption spectrum for pristine PDTG-TPD films¹⁰¹. For devices with thick active layer, the build-up of carriers in PDTG-TPD:PC₇₁BM will hinder charge collection and contribute to the fill factor reduction in thick solar cell.

As a result of the limited charge collection observed for thick-film PDTG-TPD solar cells measured at low field, we expect the photocurrent to be reduced in this field regime. Figure 5-7 shows the normalized photocurrent density–electric field ($J_L - E$) curves for PDTG-TPD:PC₇₁BM solar cells with increasing active layer thickness. For

inverted PDTG-TPD:PC₇₁BM solar cells with thickness ≤ 204 nm, the shapes of the J_L-E curves are identical. In this thickness regime, the internal electric field effectively extracts photogenerated charges from the active layer. For inverted devices with $L > 204$ nm, a change in the J_L-E profile is observed. In this thickness regime, a reduction in photocurrent is observed in the low field regime. The internal electric field is no longer able to efficiently extract photogenerated charges out of the active layer. Based on this result, the reduced fill factor observed in PDTG-TPD:PC₇₁BM solar cells with thicker active layer can be attributed to two factors: (1) the reduction in internal electric field due to increased active layer thickness L , and (2) the reduced photocurrent at low electric field due to limited charge collection. The results in Figures 5-6 and 5-7 provide evidence that space-charge accumulation contributes to the limited charge collection and reduced fill factor observed in thick-film PDTG-TPD:PC₇₁BM solar cells. Furthermore, increased recombination loss in thick-film devices is expected since carriers have to traverse a longer distance to be collected. To better understand the loss mechanisms in thick-film low-bandgap polymer solar cells, a detailed study on space-charge limited (SCL) and recombination limited photocurrent is presented herein.

5.3.2 Loss Mechanisms in Thick-Film PDTG-TPD:PC₇₁BM Solar Cells

In comparing P3HT and PDTG-TPD, a significant difference between these two polymers is the broader absorption spectra in PDTG-TPD due to its lower optical bandgap ($E_{\text{gap}} \approx 1.7$ eV)¹⁰¹. The UV-visible-NIR absorption spectra for P3HT:PC₆₁BM and PDTG-TPD:PC₇₁BM solar cells along with the photon flux for an AM 1.5G solar spectrum are shown in Figure 5-8. From the solar spectrum, an integrated photon flux of $1.6 \times 10^{17} \text{ cm}^{-2} \text{ s}^{-1}$ is obtained for a wavelength range of 400 nm – 800 nm. A larger fraction of this photon flux is absorbed by PDTG-TPD compared to the P3HT due to its

broader absorption spectrum. Figure 5-8 also shows the percentage of the AM 1.5G solar spectrum absorbed for PDTG-TPD and P3HT solar cells as a function of the active layer thickness. Here, these spectra were obtained from results of optical modeling using the n and k optical constants for each layer in the actual devices¹⁵⁹. Based on the results, PDTG-TPD:PC₇₁BM solar cells have over 30% more absorption than that in P3HT:PC₆₁BM solar cells.

Due to its higher light absorption and higher rate of photogenerated charge carriers, it is obvious that thick-film low-bandgap polymer solar cells require more efficient charge collection to prevent space-charge from accumulating in the active layer. The onset of space-charge accumulation in polymer BHJ solar cells occurs when the rate of hole generation in the polymer is greater than the rate at which those carriers can be extracted out of the active layer^{154,157}. The resulting space-charge effect screens the electric field in the active layer, resulting in reduction of electric field in the BHJ film¹⁵⁰. This reduction in electric field would negatively impact charge carrier transport and extraction in polymer solar cells. The issue of SCL photocurrent in polymer solar cells with thick active layer has been addressed with a model first proposed by Goodman and Rose¹⁵⁷. The space-charge limit is reached when the effective photocurrent (J_{ph}) generated is equal or greater than the value shown in the following equation^{157,160}:

$$J_{ph}^{SCL} = q \left(\frac{9\epsilon_0\epsilon_r\mu_h}{8q} \right)^{1/4} G^{3/4} V^{1/2} \quad (5-1)$$

where q is the electric charge, $\epsilon_0\epsilon_r$ is the dielectric permittivity, μ_h is the hole mobility, and G is the generation rate. The value of J_{ph} is determined experimentally as $J_{ph} = J_L -$

J_D , where J_L and J_D are the measured photocurrent density and dark current density, respectively.

To study the role which space-charge accumulation plays in PDTG-TPD:PC₇₁BM solar cells with a thick active layer, the SCL photocurrent model was used to confirm that the electrostatic space-charge limit was reached in devices with thicker active layer. The results for PDTG-TPD:PC₇₁BM solar cells were compared with similar devices based on P3HT:PC₆₁BM, since P3HT solar cells serve as a model system for studying the space-charge effects^{149,151}. The effective photocurrent J_{ph} normalized to the saturation photocurrent $J_{sat} = qG_{max}L$ was plotted on a double logarithmic scale against the effective voltage across the device, given by $V_{eff} = V_0 - V$. Here, V_0 is defined as the voltage where $J_{ph} = 0$ and is slightly larger than V_{oc} ¹⁵⁴. This “corrected” photocurrent analysis is a widely used tool for analyzing recombination loss processes in organic solar cells¹⁶¹⁻¹⁶³. Figure 5-9 shows the results for the PDTG-TPD:PC₇₁BM solar cells with 105 nm, 258 nm and 409 nm-thick active layer. For the device with 105 nm-thick active layer, two different voltage regimes can be observed. For $V_{eff} < 0.30$ V, J_{ph} steadily increases with voltage due to the competition between diffusion and drift for photogenerated carrier transport at low field. Above 0.30 V, the photocurrent saturates with increasing voltage. In this saturation regime, the internal field is strong enough to efficiently extract photogenerated carriers and the high field is responsible for the dissociation of e-h pairs. The voltage corresponding to the short circuit condition falls within the saturation regime, indicating that the high J_{sc} and FF obtained for this device is due to efficient charge collection by the internal electric field. For the device with a 105 nm active layer, space charge effects were not observed based on the data shown

in Figure 5-9. As the active layer thickness for PDTG-TPD cells increased above 200 nm, a square-root effective voltage dependence on J_{ph} is observed. This $J_{ph} \propto V^{1/2}$ dependence corresponds to the onset of space-charge-limited photocurrent in thick PDTG-TPD cells assuming a $J_{ph} \propto G^{3/4}$ dependence is also observed¹⁶³. The solid lines in Figure 5-9 correspond to $J_{ph} \propto V^{1/2}$. For the 409 nm-thick device, the $J_{ph} \propto V^{1/2}$ regime extends to the short circuit condition, which correlates well with the reduction in J_{sc} and FF observed in this device.

The normalized J_{ph} - V_{eff} curves for P3HT:PC₆₁BM solar cells with 100 nm, 200 nm, and 453 nm-thick active layers are shown in Figure 5-9. In contrast with the results obtained for the thick PDTG-TPD:PC₇₁BM devices, the curves for all three P3HT:PC₆₁BM solar cells look very similar despite the increase in the active layer thickness. These results correlate well with the high FF of 65% to 68% obtained for the P3HT:PC₆₁BM devices. Since the onset of the $J_{ph} \propto V^{1/2}$ regime was not occur in the P3HT:PC₆₁BM solar cells, the photocurrent in these devices are not space-charge limited despite the increase in active layer thickness.

To confirm that space-charge accumulation was contributed to the reduction in efficiency in PDTG-TPD:PC₇₁BM solar cells with thick active layer, light intensity-dependent J - V measurements were taken light for a thin-film and thick-film device. Early studies of space-charge effects in organic solar cells demonstrated the onset of SCL photocurrent through light intensity-dependent measurements¹⁵⁷. In the present work, the reduction in fill factor observed in PDTG-TPD BHJ solar cells is attributed to space-charge effects in the thick-film device. Although the square-root dependence of the effective voltage on J_{ph} is an indication of SCL photocurrent, it may also correspond to

recombination-limited photocurrent. In the case of recombination-limited photocurrent, the recombination of charge carriers becomes significant since the mean free electron or hole drift length becomes less than the active layer thickness^{163,164}. Since recombination-limited photocurrent is given by:

$$J_{ph} \propto G \sqrt{\mu\tau} \sqrt{V} \quad (5-2)$$

where τ is the lifetime of free carriers, it is possible to determine whether space-charge-limited or recombination-limited photocurrent is limiting the fill factor of the solar cell by analyzing the light intensity dependence of the photocurrent^{163,164}. While the SCL photocurrent scales with a 3/4 power dependence on light intensity (Eq. 1), the photocurrent scales linearly in the absence of space-charge effects (Eq. 2).

The dependence of J_{ph} and fill factor on incident light intensity (P_0) was plotted for the 105 nm and 409 nm-thick PDTG-TPD:PC₇₁BM solar cells (see Figure 5-10). Neutral density filters were used to control the incident light intensity, which was varied from 11.4 to 100 mW cm⁻². The $J_{ph}-P_0$ data for the thin and thick PDTG-TPD:PC₇₁BM devices, shown in Figure 5-10, was extracted from the $J_{ph}-V_{eff}$ curves shown in the same figure. For the solar cell with a 105 nm-thick active layer, J_{ph} showed a linear dependence on light intensity with the slope of the linear fit to the data equal to 1.09. In contrast, a slope of 0.77 is observed for the 409 nm-thick PDTG-TPD solar cell. The ~3/4 power dependence of J_{ph} on the incident light intensity confirms the occurrence of SCL photocurrent in PDTG-TPD:PC₇₁BM solar cells at low bias. The dependence of the saturation of the saturation voltage (V_{sat}) on incident light intensity provides further evidence, in which a slope of 0.50 is extracted from the $V_{sat}-P_0$ data^{157,163}. To form a more clear physical picture, the light-intensity dependence of the fill factor was also

analyzed and plotted in Figure 5-10. The fill factor remained relatively constant with decreasing incident light intensity for the 105 nm-thick solar cell, which is expected since the device is not space-charge-limited at $P_0 = 100 \text{ mW cm}^{-2}$ and the thickness is sufficiently thin to ensure efficient charge carrier extraction. For the 409 nm-thick PDTG-TPD solar cell, a 24% enhancement in fill factor was observed as the incident light intensity was decreased from 100 mW cm^{-2} to 11.4 mW cm^{-2} . By lowering P_0 and, consequently, reducing the generation rate of charge carriers in the thick PDTG-TPD:PC₇₁BM active layer, space-charge buildup was reduced. As a result, enhanced charge carrier collection and fill factor was observed in the solar cell. Despite this enhancement, the fill factor of the 409 nm-thick device at low light intensity does not reach the value obtained in the 105 nm device. This result indicates that the reduced photocurrent observed for thick-film devices, first shown in Figure 5-7, could not be completely recovered despite lowering the incident light intensity. There is still some degree of limited charge collection occurring in thick-film PDTG-TPD:PC₇₁BM solar cells.

To further understand the relationship between space-charge effects and the increased losses observed in PDTG-TPD:PC₇₁BM solar cells with thick active layer, a first-principles calculation is presented for the photocurrent loss relative to short-circuit current at low effective voltages. The short-circuit current density J_{sc} can be calculated from the following:

$$J_{sc} = \int_{\lambda_1}^{\lambda_2} \frac{q\lambda}{hc} EQE(\lambda)S(\lambda)d\lambda \quad (5-3)$$

where $S(\lambda)$ is the reference AM 1.5G power intensity and λ_1 and λ_2 are the wavelength limits of the absorption spectrum of the device. The external quantum efficiency is given

by $EQE(\lambda) = IQE(\lambda) \cdot \eta_A(\lambda)$, where IQE is the internal quantum efficiency and η_A the absorption efficiency. Using the calculated η_A from Figure 5-6 and assuming various values of IQE (from 50 to 100%), calculated values of J_{sc} was obtained for PDTG-TPD:PC₇₁BM solar cells¹⁶⁴. Figure 5-11 shows the number of photons absorbed in the active layer and the corresponding J_{sc} versus the thickness of this layer. The experimental results for PDTG-TPD:PC₇₁BM solar cells are shown for comparison. The calculated J_{sc} strongly agrees well with the experimental results assuming an IQE of 90 – 100%, which is in agreement with previous results demonstrating that low bandgap polymer solar cells with IQE approaching 100% are obtainable¹¹⁷. The photocurrent at low effective voltages can then be determined from the following equation¹⁶⁵:

$$J_{ph} = qGL \left[\frac{\exp(eV/kT) + 1}{\exp(eV/kT) - 1} - \frac{2kT}{eV} \right] \quad (5-4)$$

where k is Boltzmann's constant and T is the temperature. In the low active layer thickness regime in which $J_{ph} < J_{ph}^{SCL}$, the calculated photocurrent is given by Equation 3. At some critical active layer thickness (L_c), the solar cell becomes space-charge-limited (i.e. $J_{ph} = J_{ph}^{SCL}$). For devices with $L \geq L_c$, the calculated photocurrent is given by Equation 1 since $J_{ph} > J_{ph}^{SCL}$.

Using this formulism, the photocurrent loss relative to J_{sc} for PDTG-TPD:PC₇₁BM solar cells, which is given as $1 - J_{ph}/J_{sc}$, was calculated for a low effective voltage and plotted versus active layer thickness. This result is summarized in Figure 5-11. For this calculation, it was assumed that the number of photons absorbed in the active layer was equal to the generation rate, G ^{159,166}. Figure 5-11 shows the calculated photocurrent loss before the space-charge limit was reached ($J_{ph} < J_{ph}^{SCL}$, black line), after the space-

charge limit is reached ($J_{ph} > J_{ph}^{SCL}$, gray line), and the photocurrent loss extracted from the experimental data. For a given hole mobility, the calculated curves intersect when $J_{ph} = J_{ph}^{SCL}$ at the critical thickness L_c (dotted line). For $L \geq L_c$, the photocurrent loss in PDTG-TPD:PC₇₁BM solar cell significantly increases since J_{ph} is space-charge limited. Increasing the hole mobility in the active layer leads to a larger L_c , allowing for the active layer thickness to be increased without substantially increasing the photocurrent loss. These conclusions are in agreement with previous reports demonstrating that a high hole mobility in the polymer:fullerene blend is required to maintain efficient operation in polymer solar cells with thicker active layer^{149,151}. The experimental photocurrent loss was then extracted for the PDTG-TPD:PC₇₁BM solar cells and compared to the calculated results. The calculated photocurrent loss is comparable to the experimental values assuming a hole mobility of $1.5 \times 10^{-3} \text{ cm}^2 \text{ V}^{-1} \text{ s}^{-1}$, which is close to the hole mobility obtained experimentally.

This theoretical model was used to predict the value of L_c for polymer solar cells with E_g for the conjugated polymer ranging from 1.4 to 2.2 eV. To make this prediction, it was assumed that the absorption efficiency for the polymer-fullerene blend scales linearly with the bandgap of the polymer. Furthermore, the fraction of photons absorbed from AM1.5G versus active layer thickness calculated for PDTG-TPD:PC₇₁BM was used as a reference. Based on these assumptions, the critical thickness corresponding to the onset of SCL photocurrent was plotted versus bandgap of the polymer. This result is shown in Figure 5-12 for polymer solar cells with increasing hole mobility. The critical thickness L_c is linearly proportional to the bandgap of the polymer, and increases as the hole mobility of the polymer-fullerene blend increases. Based on this result, it is clear

that low bandgap polymer solar cells with E_g between 1.4 and 1.7 eV are severely limited in their active layer thickness due to the large carrier concentration generated in these devices. For example, a hole mobility $\geq 1 \times 10^{-3} \text{ cm}^2 \text{ V}^{-1} \text{ s}^{-1}$ would be required to ensure that $L_c > 200 \text{ nm}$. If this high hole mobility cannot be obtained in these devices, the solar cells would show significant reductions in FF with increasing active layer thickness¹⁵⁶.

There are two important assumptions of the theoretical SCL photocurrent model employed in this work. First, the SCL model assumes that $\mu_h \ll \mu_e$ since the accumulation of slow carriers in the active layer is responsible for the space-charge limit being reached. For polymer solar cells, SCL photocurrent was first observed in systems with very imbalanced carrier mobilities¹⁵⁰. In this work, SCL photocurrent was observed for solar cells using a polymer showing high hole mobility and therefore having a smaller carrier mobility imbalance. Nevertheless, the experimental results clearly indicate that space-charge accumulation contributed to the reduced fill and PCE observed in thick-film PDTG-TPD:PC₇₁BM solar cells. Furthermore, by calculating the active layer thickness at which $J_{ph} = J_{ph}^{SCL}$, the model predicts that the space-charge limit is reached when $L \approx 225 \text{ nm}$ (see Figure 5-11). This prediction correlates well with the reduced photocurrent observed for devices with $L > 200 \text{ nm}$. Second, the model assumes that the loss observed in thick-film polymer solar cells is due to either SCL or recombination-limited photocurrent. However, these two loss processes are interrelated¹⁵⁰. It is expected that SCL and recombination-limited photocurrent will contribute to the losses observed in PDTG-TPD solar cells with thick active layer.

5.4 Concluding Remarks

To conclude, the loss mechanisms responsible for limited device performance in thick-film PDTG-TPD:PC₇₁BM solar cells have been investigated. For polymer solar cells with thickness up to 200 nm, efficiencies in excess of 8.0% were obtained for devices under AM 1.5G illumination at 100 mW cm⁻². These results show that the active layer thickness requirement inherent to large-scale R2R processing can be satisfied while still maintaining the high power conversion efficiency, and highlights the potential of PDTG-TPD:PC₇₁BM polymer solar cells for large-scale manufacturing. For $L > 200$ nm, space-charge effects and reduced carrier lifetime limits charge collection in thick-film devices. This limited charge collection coincides with reduced fill factor and power conversion efficiency in thick devices. These results indicate that although high efficiencies can be obtained in solar cells with low-bandgap conjugated donor-acceptor polymers, the high density of photogenerated charge carriers severely limits the performance of solar cells with a thick active layer.

Table 5-1. Averaged solar cell performance for inverted PDTG-TPD:PC₇₁BM devices with various active layer thickness under initial AM 1.5G solar illumination.

Active Layer Thickness	J_{sc} (mA cm ⁻²)	J_{sc} (EQE) (mA cm ⁻²)	V_{oc} (V)	FF (%)	PCE (%)
90 nm	12.5 +/- 0.1	12.3	0.88 +/- 0.007	68.5 +/- 0.01	7.5 +/- 0.001
105 nm	13.3 +/- 0.1	13.0	0.87 +/- 0.006	68.7 +/- 0.01	7.9 +/- 0.001
153 nm	13.5 +/- 0.1	13.5	0.86 +/- 0.007	68.1 +/- 0.01	8.0 +/- 0.001
204 nm	14.9 +/- 0.2	14.7	0.86 +/- 0.009	64.5 +/- 0.01	8.2 +/- 0.002
258 nm	16.1 +/- 0.2	16.0	0.85 +/- 0.006	54.1 +/- 0.01	7.4 +/- 0.001
409 nm	15.2 +/- 0.1	14.9	0.82 +/- 0.005	41.6 +/- 0.01	5.2 +/- 0.001

Table 5-2. Averaged solar cell performance for inverted P3HT:PC₆₁BM devices with various active layer thickness under initial AM 1.5G solar illumination.

Active Layer Thickness	J_{sc} (mA/cm ²)	J_{sc} (EQE) (mA/cm ²)	V_{oc} (V)	FF (%)	PCE (%)
100 nm	6.1 +/- 0.23	6.4	0.62	70.4 +/- 0.1	2.7 +/- 0.12
150 nm	6.1 +/- 0.05	6.4	0.62	67.1 +/- 0.1	2.5 +/- 0.17
170 nm	7.0 +/- 0.43	7.7	0.62	72.0 +/- 0.1	3.1 +/- 0.25
200 nm	7.2 +/- 0.10	7.5	0.62	71.9 +/- 0.1	3.2 +/- 0.04
307 nm	7.6 +/- 0.25	6.4	0.58	68.7 +/- 1.1	3.0 +/- 0.10
340 nm	7.6 +/- 0.04	6.7	0.58	69.0 +/- 0.5	3.1 +/- 0.10
453 nm	7.4 +/- 0.29	6.5	0.56	65.5 +/- 2.2	2.7 +/- 0.20

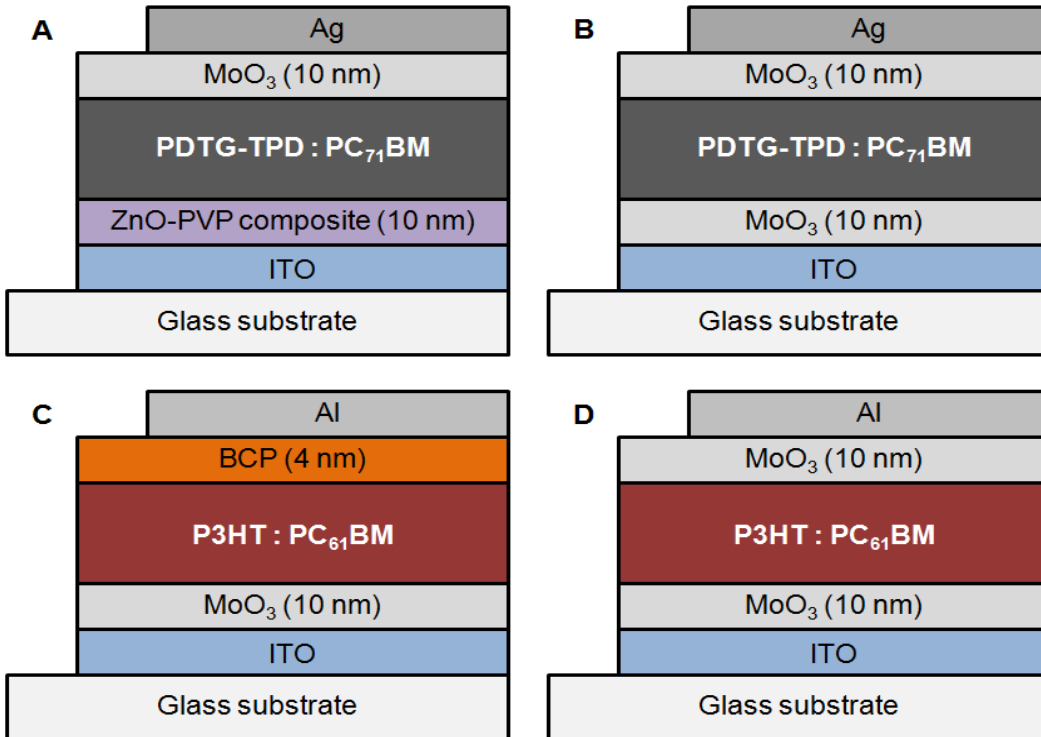


Figure 5-1. Device structure for PDTG-TPD:PC₇₁BM solar cells, P3HT:PC₆₁BM solar cells, and corresponding single-carrier devices studied in this work. A) Inverted PDTG-TPD:PC₇₁BM solar cell. B) PDTG-TPD:PC₇₁BM hole-only device. C) P3HT:PC₆₁BM solar cell. D) P3HT:PC₆₁BM hole-only device.

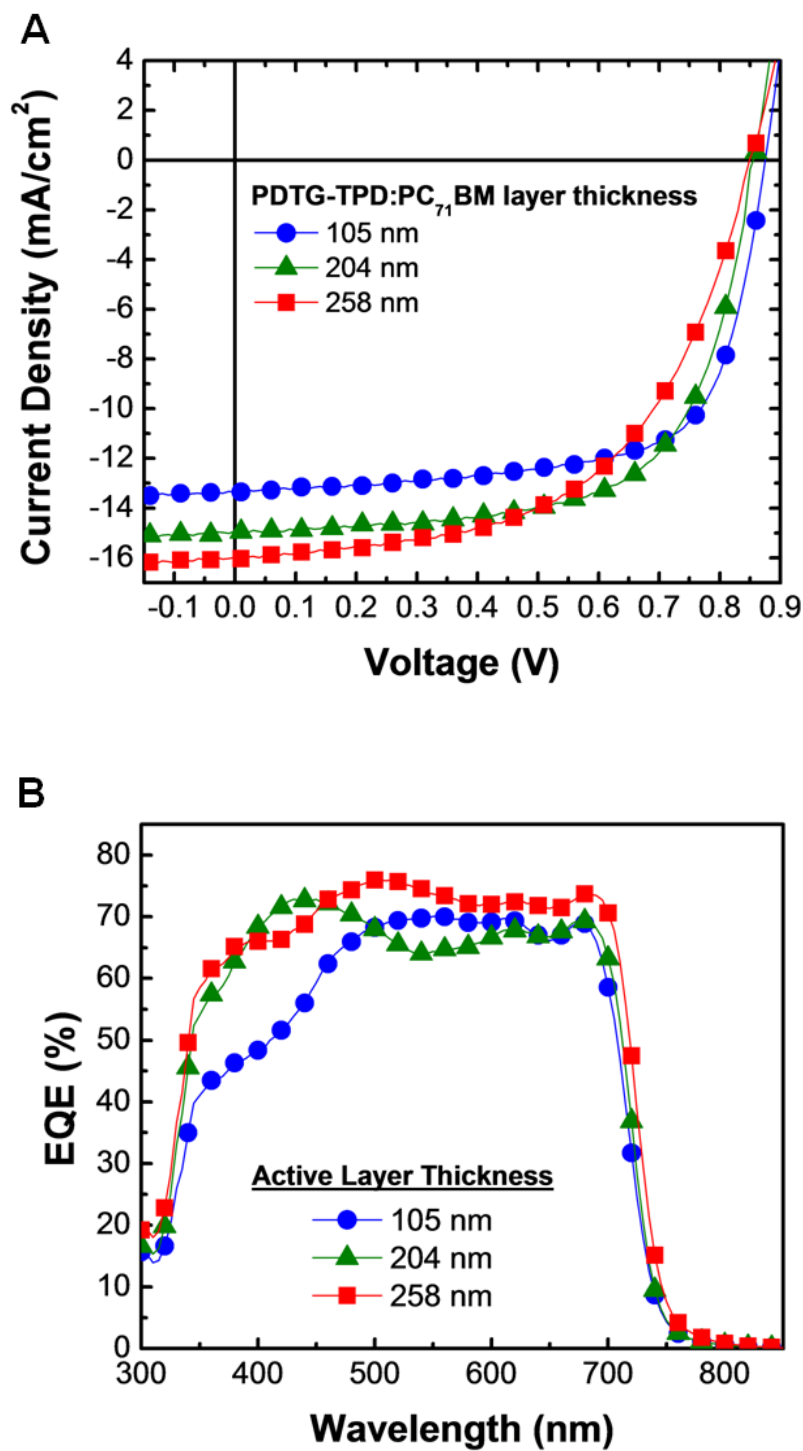


Figure 5-2. Photo J-V characteristics and EQE spectra for inverted PDTG-TPD:PC₇₁BM solar cells with increasing active layer thickness. A) Photo J-V characteristics for PDTG-TPD:PC₇₁BM solar cells with 105 nm, 204 nm, and 258 nm-thick active layer. B) Corresponding EQE spectra for the devices.

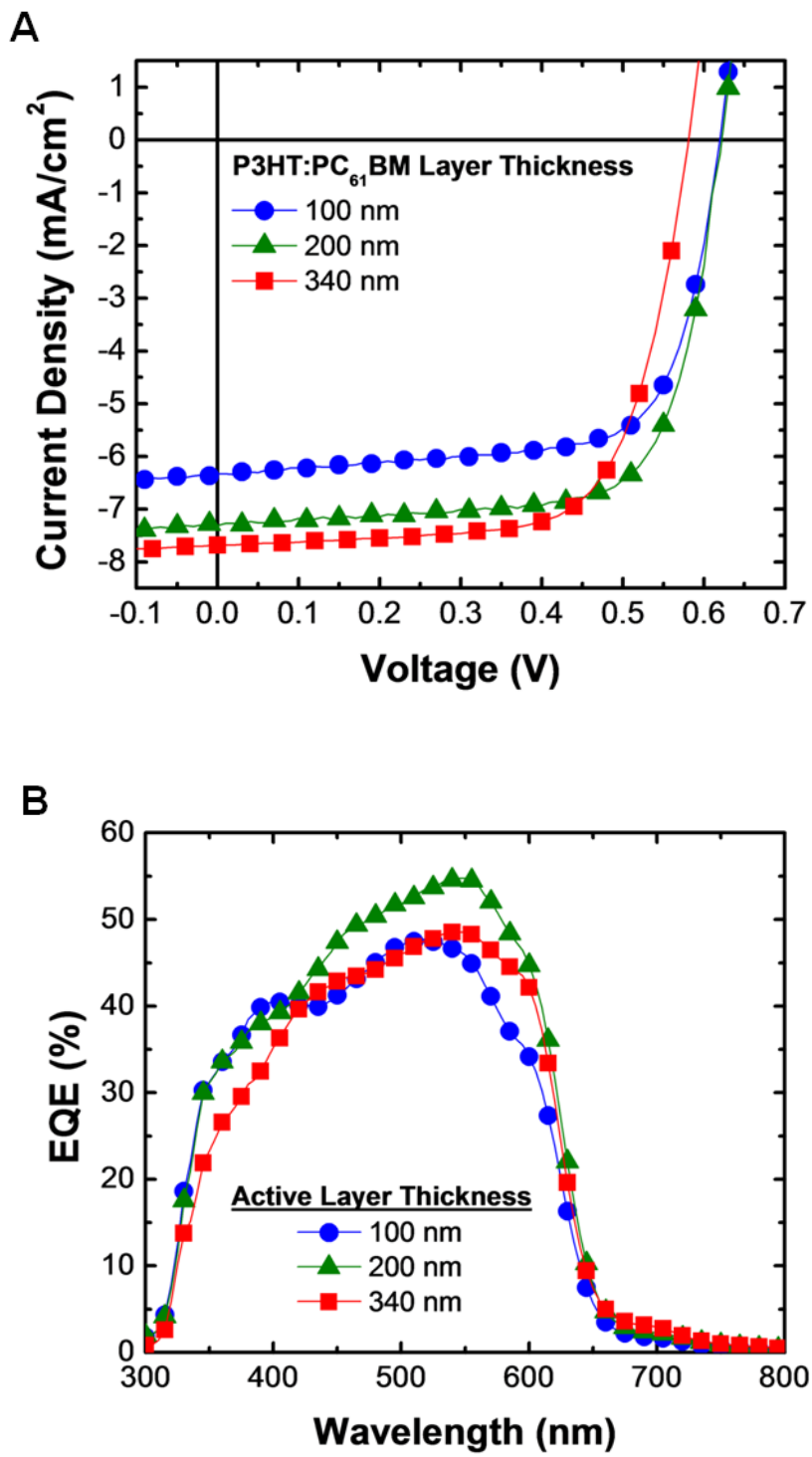


Figure 5-3. Photo J-V characteristics and EQE spectra for inverted P3HT:PC₆₁BM solar cells with increasing active layer thickness. A) Photo J-V characteristics for P3HT:PC₆₁BM solar cells with 100 nm, 200 nm, and 340 nm-thick active layer. B) Corresponding EQE spectra for the devices.

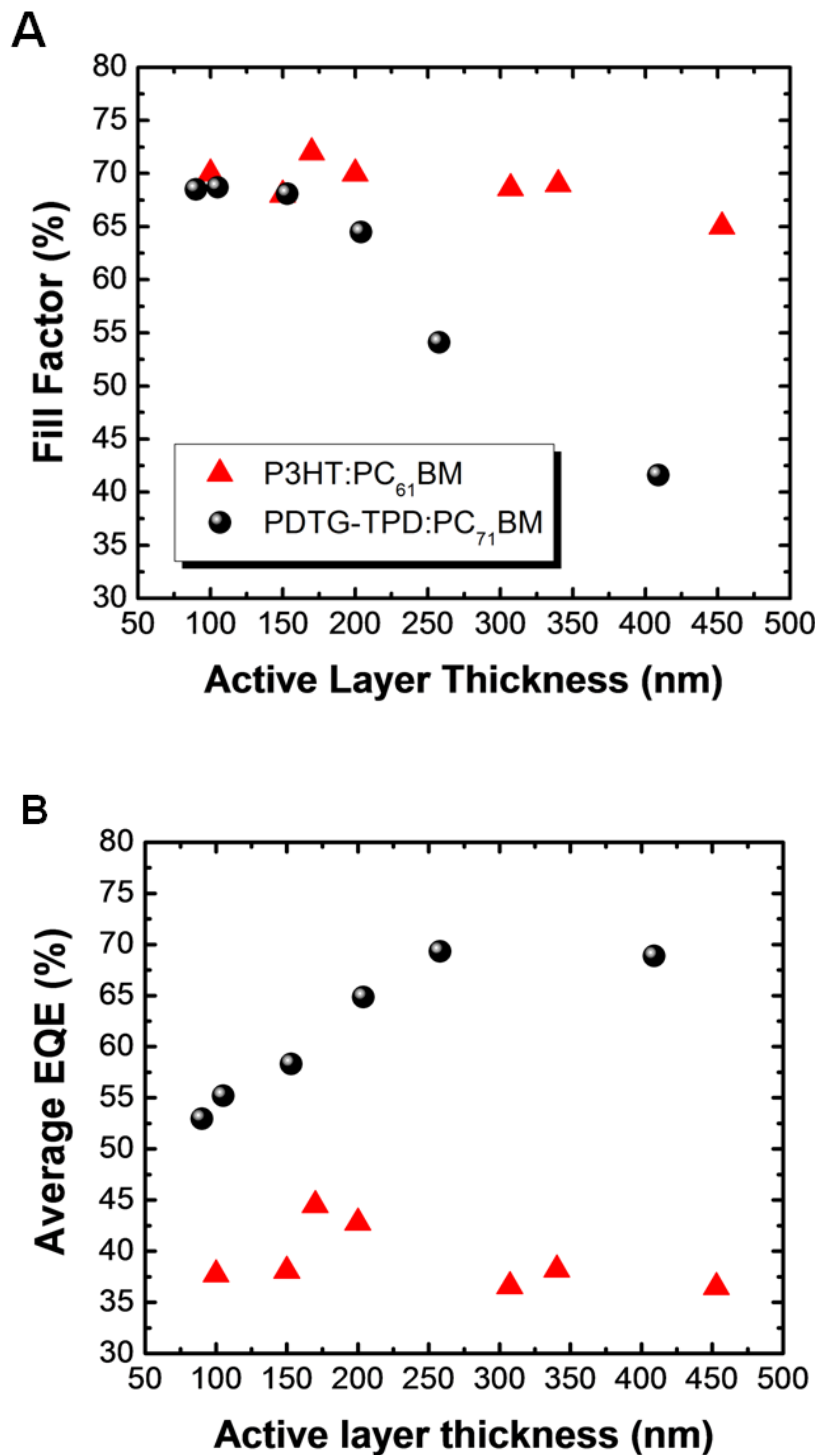


Figure 5-4. Average fill factor and EQE versus active layer thickness for PDTG-TPD:PC₇₁BM and P3HT:PC₆₁BM solar cells. A) Average fill factor vs. active layer thickness for the devices. B) Average EQE vs. active layer thickness for the devices.

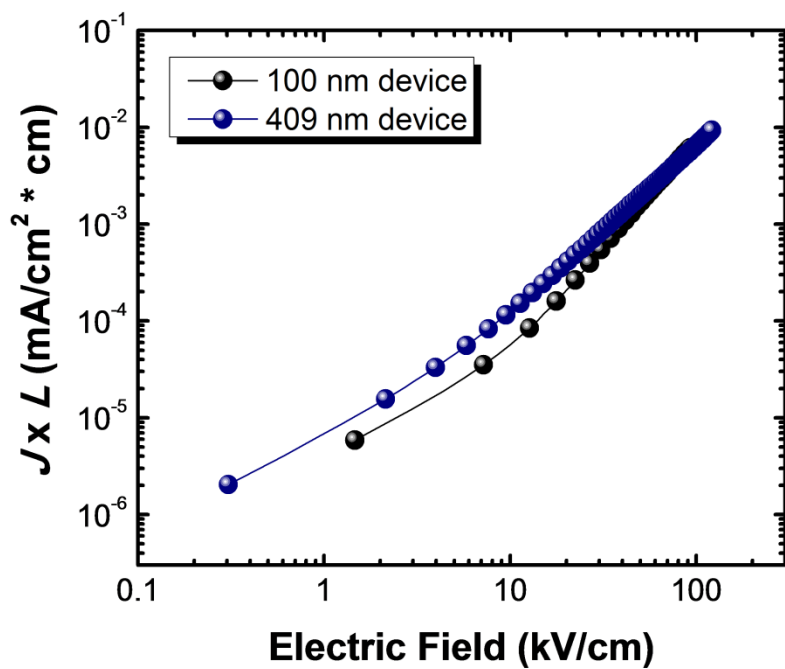


Figure 5-5. Current density times active layer thickness ($J \times L$) versus electric field curves for PDTG-TPD:PC₇₁BM hole-only devices with 100 nm and 409 nm-thick layers.

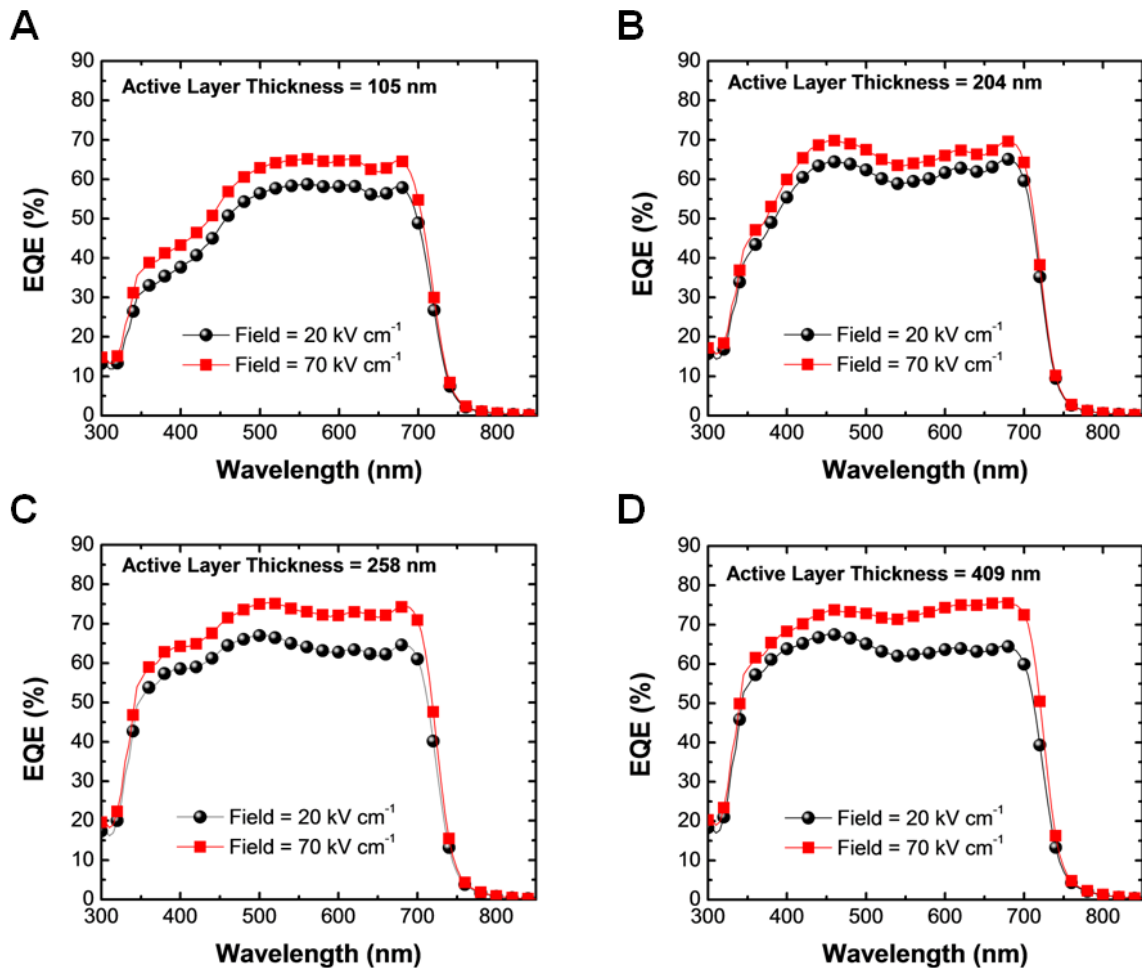


Figure 5-6. Field-dependent EQE spectra for PDTG-TPD:PC₇₁BM solar cells with increasing active layer thickness. A) 105 nm-thick active layer. B) 204 nm-thick active layer. C) 258 nm-thick active layer. D) 409 nm-thick active layer. The EQE spectra were measured at 20 kV cm⁻¹ and 70 kV cm⁻¹.

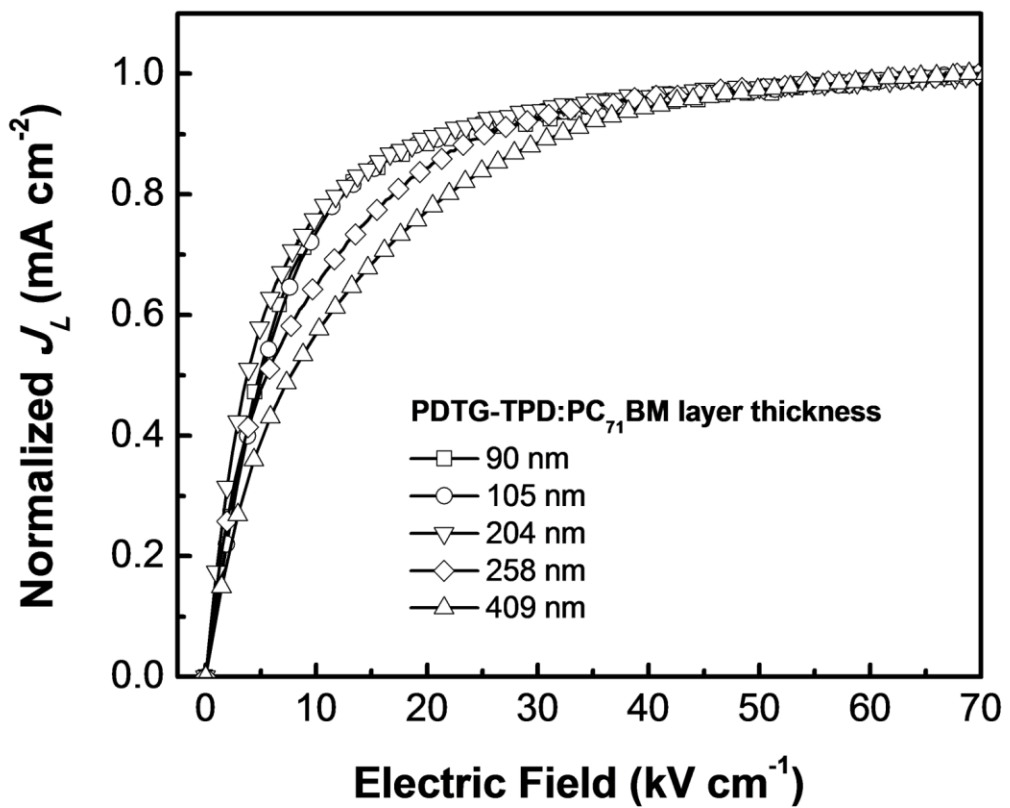


Figure 5-7. Normalized photocurrent density (J_L) as a function of internal electric field for inverted PDTG-TPD:PC₇₁BM solar cells with increasing active layer thickness.

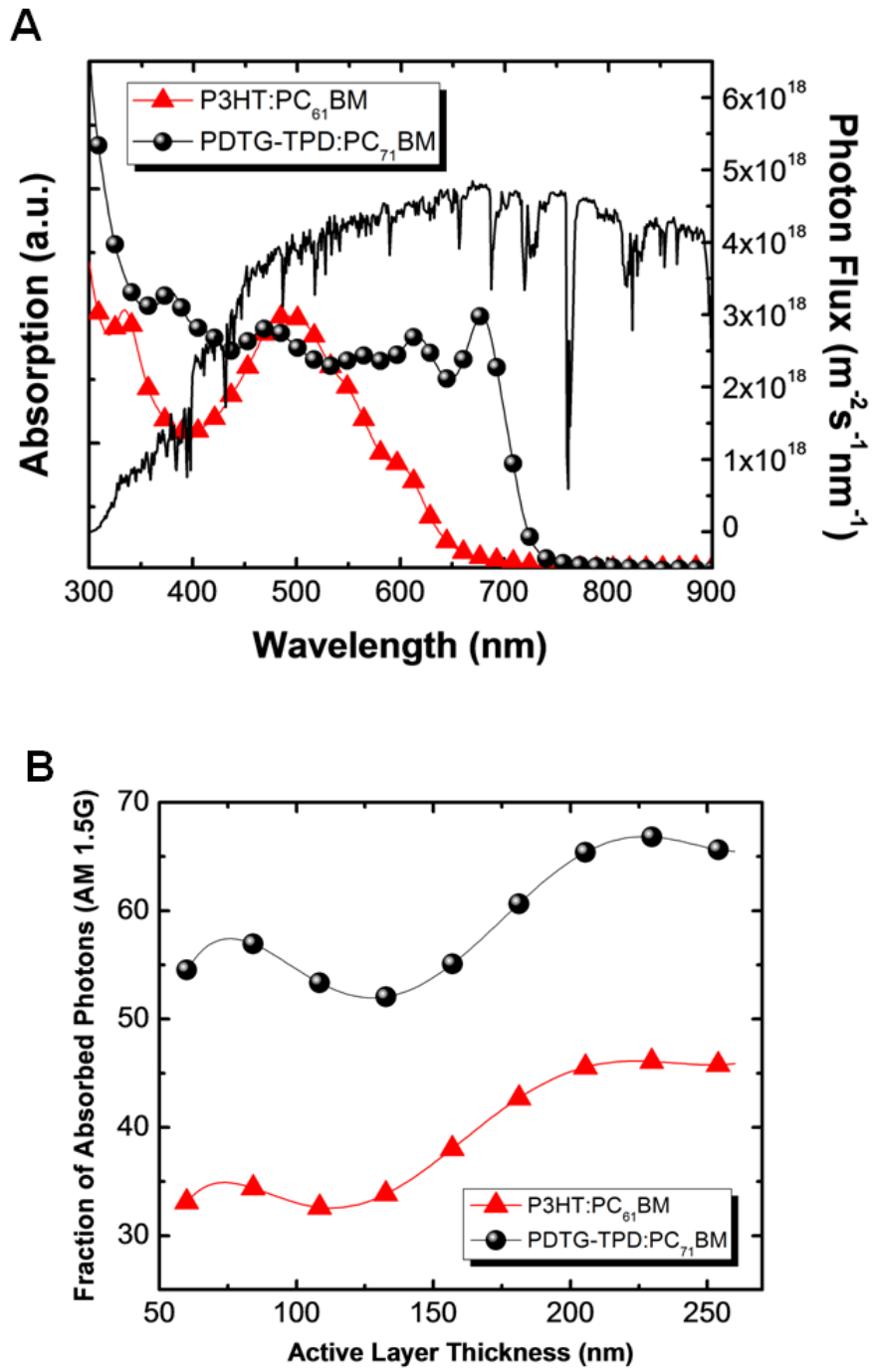


Figure 5-8. UV-Vis-NIR spectra and fraction of photons absorbed vs. active layer thickness for PDTG-TPD:PC₇₁BM and P3HT:PC₆₁BM solar cells. A) UV-Vis-NIR absorption spectra for the devices. The photon flux for the AM 1.5G solar spectrum is shown. B) The fraction of absorbed photons versus active layer thickness.

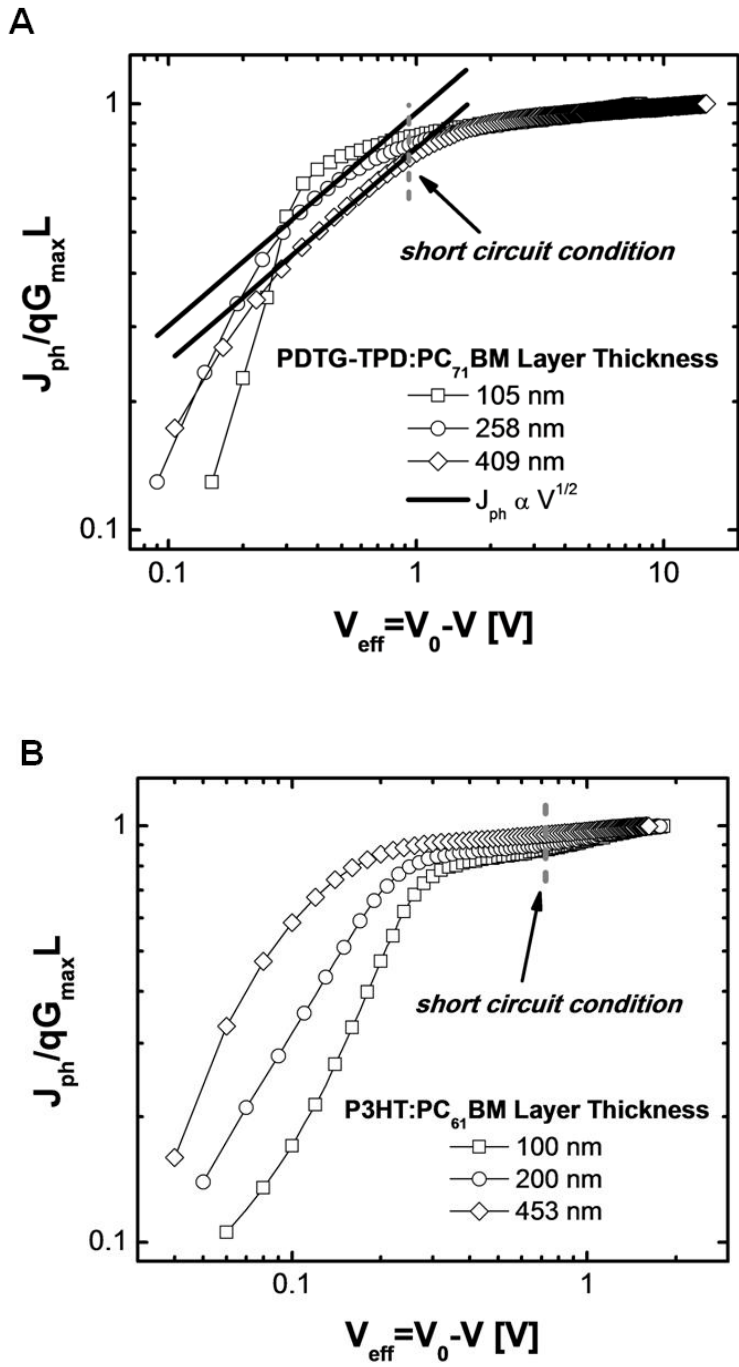


Figure 5-9. Normalized J_{ph} – V_{eff} curves for under 100 mW cm⁻² illumination for PDTG-TPD:PC₇₁BM and P3HT:PC₆₁BM solar cells with increasing active layer thickness. A) PDTG-TPD:PC₇₁BM cells with 105 nm, 258 nm, and 409 nm-thick layer. B) P3HT:PC₆₁BM cells with 100 nm, 200 nm, and 453-nm thick active layer. Dashed lines highlight the value of V_{eff} corresponding the short-circuit condition ($V_{eff} = V_0$). The solid lines correspond to $J_{ph} \propto V^{1/2}$ fits of the photocurrent in the SCL regime for PDTG-TPD solar cells.

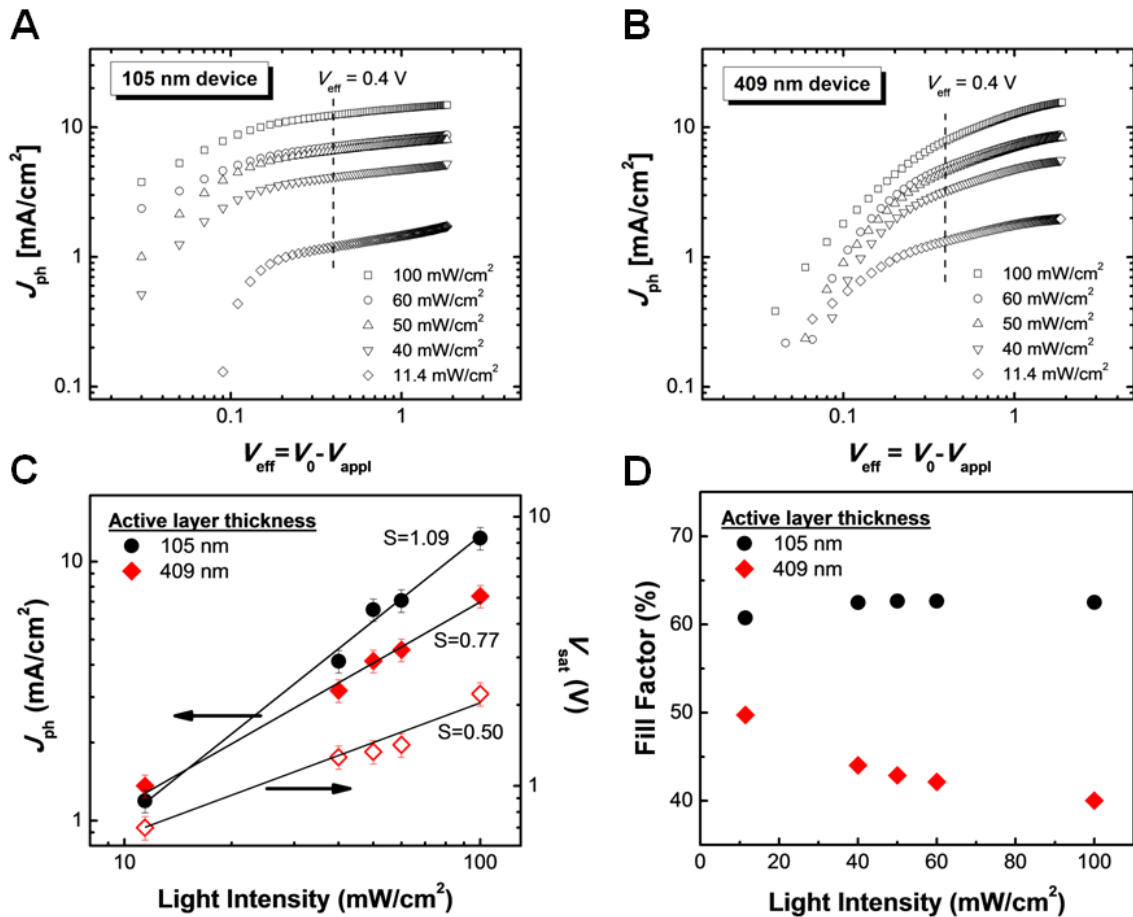


Figure 5-10. Light intensity dependence of the photocurrent and fill factor for 105 nm-thick and 409 nm-thick PDTG-TPD:PC₇₁BM solar cells. A) $J_{\text{ph}}-V_{\text{eff}}$ curves for the 105 nm-thick device under various light intensities (from 10 to 100 mW cm⁻²). B) $J_{\text{ph}}-V_{\text{eff}}$ curves for the 409 nm-thick device under the same light intensities. C) J_{ph} versus light intensity for the same devices. D) Fill factor vs. light intensity for the same devices.

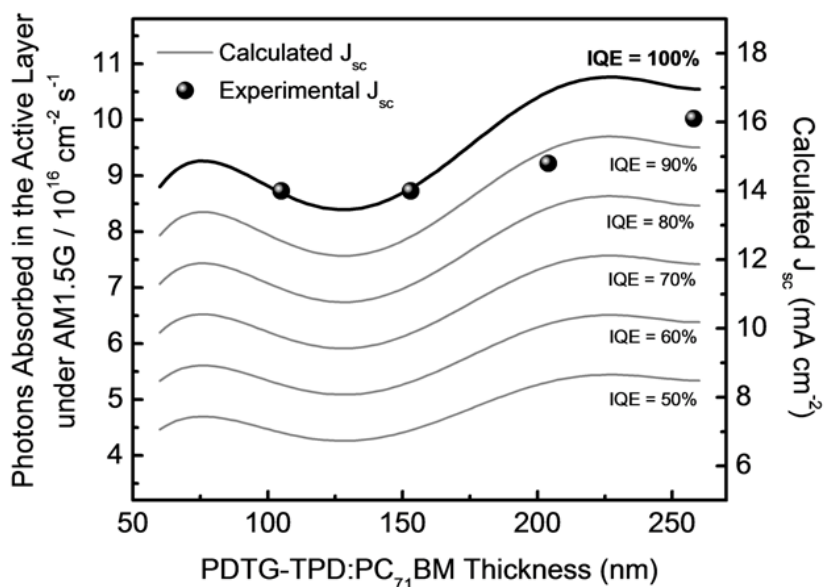
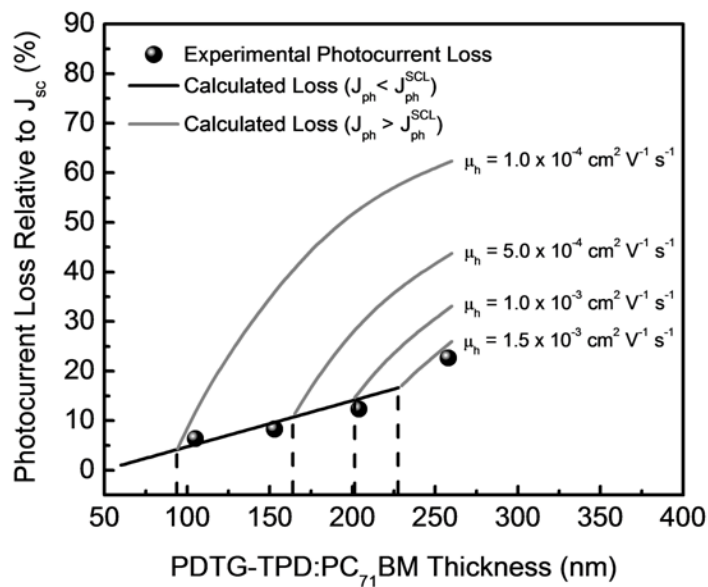
A**B**

Figure 5-11. Calculated number of photons absorbed in the PDTG-TPD:PC₇₁BM layer under AM1.5G illumination and photocurrent loss as a function of layer thickness. A) Number of photons absorbed in the photoactive layer and the corresponding short-circuit density J_{sc} at various IQE values vs. active layer thickness. B) Photocurrent loss relative to J_{sc} ($1 - J_{ph}/J_{sc}$) versus layer thickness at various hole mobility values. For this calculation, $V_{eff} = 0.4$ V and $\epsilon_r = 4.78$.

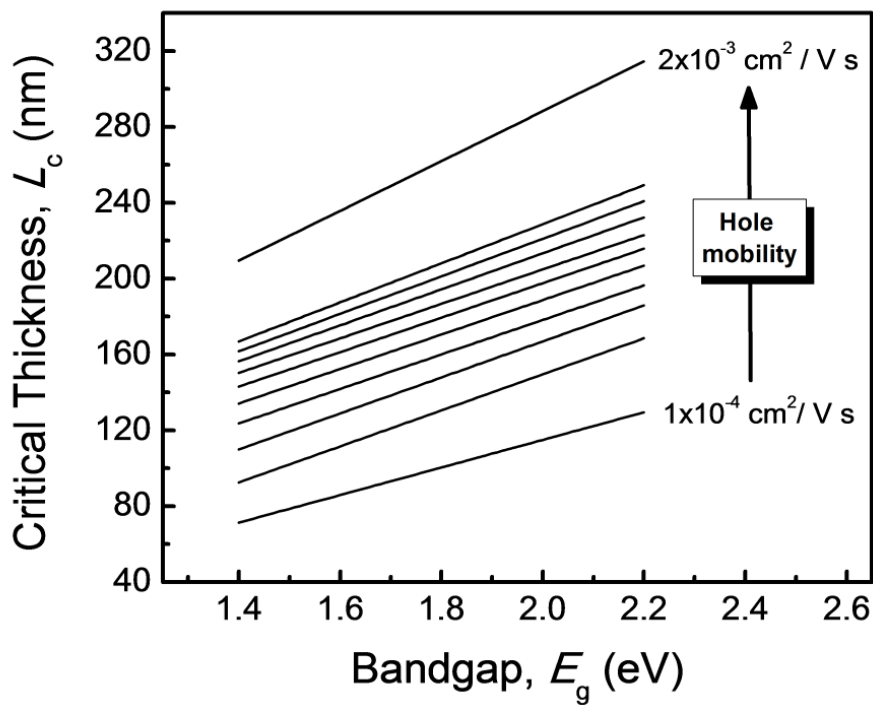


Figure 5-12. The critical active layer thickness corresponding to the onset of SCL photocurrent (L_c) in low bandgap polymer solar cells versus bandgap of the polymer. The calculation was performed for various values of hole mobility, ranging from $1 \times 10^{-4} \text{ cm}^2 \text{ V}^{-1} \text{ s}^{-1}$ to $2 \times 10^{-3} \text{ cm}^2 \text{ V}^{-1} \text{ s}^{-1}$.

CHAPTER 6 CONCLUSIONS

By inverting the device geometry of organic electronic and optoelectronic devices, it is possible to improve the device's stability and large-scale R2R processing compatibility. However, it is important to also demonstrate enhanced device performance for organic electronic devices with this architecture. Early work on inverted small-molecule and polymer LEDs showed high drive voltage due to insufficient carrier injection. To address this problem, carrier injection for conventional and inverted organic single-carrier devices was studied in Chapter 2. To facilitate carrier injection, electron acceptors were used as injection layer for devices with either geometry. It was found that inverted devices showed higher current density and injection efficiency compared to devices with a conventional architecture. The results were confirmed by cross-referencing steady state J - V and DI-SCLC transient measurements. The enhanced carrier injection was attributed to a stronger degree of charge transfer between the electron accepting injection layer and the organic semiconductor in the inverted device.

On that basis, the injection efficiency for devices with conventional structure was enhanced by sandwiching a p-doped hole injection layer between the anode and the organic semiconductor. Controlled doping of this interlayer allowed the injection efficiency to be tuned. Given this result, it was understood that a strong degree of charge transfer between the electron accepting injection layer and the organic semiconductor was required to obtain an ohmic contact. In future work, replacing the electron acceptors studied in this chapter with solution-processed electron accepting interlayers is preferred for large-scale processing. However, obtaining strong charge transfer will be required to observe ohmic injection with these new novel materials.

Similar to reports on inverted OLEDs, early work on inverted OPV cells showed that the device performance was reduced when this geometry was employed. In Chapter 4, we showed that the reduced device performance of inverted polymer photovoltaic cells was due to limited carrier extraction by the bottom electron transporting layer. By introducing a UV-ozone modified ZnO-polymer composite layer, the electronic coupling between this interlayer and the photoactive layer was improved. As a result, carrier extraction was improved and OPV cells with power conversion efficiencies over 8% were obtained. This work illustrated the importance of carrier selective interlayers for OPVs. Much of the research reported in the literature has focused on employing novel carrier-selective interlayers for OPVs, such as the water/alcohol soluble polyfluorenes used in the state-of-the-art devices. This will continue to be an important research area for OPVs.

Lastly, in Chapter 5 the thickness dependence of the efficiency was investigated for inverted organic photovoltaic cells. Demonstrating efficient OPV cell operation for devices with thicker active layer is important for large-scale R2R processing. Since high carrier mobility values were obtained in the polymer photovoltaic cells studied, it was assumed that the active layer thickness could be extended without sacrificing the device's performance. Power conversion efficiencies over 8% was obtained for OPV cells with active layer thickness up to 200 nm. Increasing the active layer thickness further significantly reduced the cell's performance. This loss was attributed to space-charge effects in the thick photoactive layer. Future work on thick-film OPV cells should focus on eliminating space-charge buildup in the photoactive layer.

LIST OF REFERENCES

- 1 Tse, S., Cheung, C. & So, S. in *Organic Electronics: Materials, Processing, Devices and Applications* (ed F. So) Ch. 3, 61-109 (CRC Press, 2009).
- 2 Bässler, H. Charge Transport in Disordered Organic Photoconductors a Monte Carlo Simulation Study. *physica status solidi (b)* **175**, 15-56, doi:10.1002/pssb.2221750102 (1993).
- 3 Nagase, T. & Naito, H. Localized-state distributions in molecularly doped polymers determined from time-of-flight transient photocurrent. *Journal of applied physics* **88**, 252-259, doi:10.1063/1.373649 (2000).
- 4 Salaneck, W. R., Seki, K., Kahn, A. & Pireaux, J. J. *Conjugated Polymer and Molecular Interfaces: Science and Technology for Photonic and Optoelectronic Application*. (Marcel Dekker Inc., 2002).
- 5 Tang, C. & VanSlyke, S. Organic electroluminescent diodes. *Applied Physics Letters* **51**, 913-915 (1987).
- 6 Hofmann, S., Thomschke, M., Lüssem, B. & Leo, K. Top-emitting organic light-emitting diodes. *Optics Express* **19**, A1250-A1264 (2011).
- 7 Ikaia, M., Tokitob, S., Sakamoto, Y., Suzuki, T. & Taga, Y. Highly efficient phosphorescence from organic light-emitting devices with an exciton-block layer. *Applied Physics Letters* **79**, 156-158 (2001).
- 8 Sasabe, H. *et al.* High-efficiency blue and white organic light-emitting devices incorporating a blue iridium carbene complex. *Advanced Materials* **22**, 5003-5007 (2010).
- 9 Lee, T. W. *et al.* High-efficiency stacked white organic light-emitting diodes. *Applied Physics Letters* **92**, 043301 (2008).
- 10 Seidler, N. *et al.* Influence of the hole blocking layer on blue phosphorescent organic light-emitting devices using 3, 6-di (9-carbazolyl)-9-(2-ethylhexyl) carbazole as host material. *Applied Physics Letters* **96**, 093304 (2010).
- 11 Wang, Q., Deng, Z. & Ma, D. Highly efficient inverted top-emitting organic light-emitting diodes using a lead monoxide electron injection layer. *Optics Express* **17**, 17269-17278 (2009).
- 12 Chen, C. W., Lin, C. L. & Wu, C. C. An effective cathode structure for inverted top-emitting organic light-emitting devices. *Applied Physics Letters* **85**, 2469-2471, doi:10.1063/1.1798392 (2004).

- 13 Lee, H., Park, I., Kwak, J., Yoon, D. Y. & Lee, C. Improvement of electron injection in inverted bottom-emission blue phosphorescent organic light emitting diodes using zinc oxide nanoparticles. *Applied Physics Letters* **96**, 153306 (2010).
- 14 Yun, C. *et al.* Electron injection via pentacene thin films for efficient inverted organic light-emitting diodes. *Applied Physics Letters* **95**, 053301 (2009).
- 15 Zhou, X. *et al.* Low-voltage inverted transparent vacuum deposited organic light-emitting diodes using electrical doping. *Applied Physics Letters* **81**, 922-924, doi:10.1063/1.1496502 (2002).
- 16 Krebs, F. C., Tromholt, T. & Jørgensen, M. Upscaling of polymer solar cell fabrication using full roll-to-roll processing. *Nanoscale* **2**, 873-886 (2010).
- 17 PolyIC. *Laboratory Printing Machine*, <<http://old.poly-id.com/press-images.php>> (March 22, 2006).
- 18 LGBlog. *LG ushers in a new era of viewing pleasure with "ultimate display" OLED TV*, <<http://www.lgblog.co.uk/2012/05/oled/>> (2012).
- 19 Reineke, S. *et al.* White organic light-emitting diodes with fluorescent tube efficiency. *Nature* **459**, 234-238 (2009).
- 20 Ho, P. K. H. *et al.* Molecular-scale interface engineering for polymer light-emitting diodes. *Nature* **404**, 481-484 (2000).
- 21 Van Slyke, S., Chen, C. & Tang, C. Organic electroluminescent devices with improved stability. *Applied Physics Letters* **69**, 2160 (1996).
- 22 Arias, A., Granström, M., Petritsch, K. & Friend, R. Organic photodiodes using polymeric anodes. *Synthetic metals* **102**, 953-954 (1999).
- 23 Kim, W. *et al.* Molecular organic light-emitting diodes using highly conducting polymers as anodes. *Applied Physics Letters* **80**, 3844-3846 (2002).
- 24 Choulis, S. A., Choong, V. E., Patwardhan, A., Mathai, M. K. & So, F. Interface modification to improve hole-injection properties in organic electronic devices. *Advanced Functional Materials* **16**, 1075 (2006).
- 25 Choudhury, K. R. *et al.* Highly Efficient Hole Injection Using Polymeric Anode Materials for Small-Molecule Organic Light-Emitting Diodes. *Advanced Functional Materials* **19**, 491-496 (2009).

- 26 Tokito, S., Noda, K. & Taga, Y. Metal oxides as a hole-injecting layer for an organic electroluminescent device. *Journal of Physics D: Applied Physics* **29**, 2750 (1996).
- 27 Ding, H., Gao, Y., Small, C., Subbiah, J. & So, F. Energy level evolution of air and oxygen exposed molybdenum trioxide films. *Applied Physics Letters* **96**, 243307 (2010).
- 28 Kröger, M. *et al.* Role of the deep-lying electronic states of MoO₃ in the enhancement of hole-injection in organic thin films. *Applied Physics Letters* **95**, 123301 (2009).
- 29 Park, S. M., Kim, Y. H., Yi, Y., Oh, H. Y. & Won Kim, J. Insertion of an organic interlayer for hole current enhancement in inverted organic light emitting devices. *Applied Physics Letters* **97**, 063308-063308-063303 (2010).
- 30 Kim, Y. K., Kim, J. W. & Park, Y. Energy level alignment at a charge generation interface between 4, 4-bis (N-phenyl-1-naphthylamino) biphenyl and 1, 4, 5, 8, 9, 11-hexaazatriphenylene-hexacarbonitrile. *Applied Physics Letters* **94**, 063305 (2009).
- 31 Zhou, X. *et al.* Enhanced Hole Injection into Amorphous Hole-Transport Layers of Organic Light-Emitting Diodes Using Controlled p-Type Doping. *Advanced Functional Materials* **11**, 310-314 (2001).
- 32 Gao, W. & Kahn, A. Electronic structure and current injection in zinc phthalocyanine doped with tetrafluorotetracyanoquinodimethane: Interface versus bulk effects. *Organic Electronics* **3**, 53-63 (2002).
- 33 Pfeiffer, M., Forrest, S. R., Leo, K. & Thompson, M. E. Electrophosphorescent pin organic light-emitting devices for very-high-efficiency flat-panel displays. *Advanced Materials* **14**, 1633-1636 (2002).
- 34 Chang, C. C., Hsieh, M. T., Chen, J. F., Hwang, S. W. & Chen, C. H. Highly power efficient organic light-emitting diodes with a p-doping layer. *Applied Physics Letters* **89**, 253504 (2006).
- 35 Kröger, M. *et al.* P-type doping of organic wide band gap materials by transition metal oxides: A case-study on Molybdenum trioxide. *Organic Electronics* **10**, 932-938 (2009).
- 36 Ma, J. *et al.* Highly power efficient organic light-emitting diodes based on Cs₂CO₃ n-doped and MoO₃ p-doped carrier transport layers. *Semiconductor science and technology* **24**, 035009 (2009).

- 37 Drechsel, J., Pfeiffer, M., Zhou, X., Nollau, A. & Leo, K. Organic Bipolar diodes by p-doping of amorphous wide-gap semiconductors: CV and impedance spectroscopy. *Synthetic Metals* **127**, 201-205 (2002).
- 38 Poplavskyy, D., Su, W. & So, F. Bipolar charge transport, injection, and trapping studies in a model green-emitting polyfluorene copolymer. *Journal of applied physics* **98**, 014501-014501-014511 (2005).
- 39 Cheung, C., Song, W. & So, S. Role of air exposure in the improvement of injection efficiency of transition metal oxide/organic contact. *Organic Electronics* **11**, 89-94 (2010).
- 40 Han, T. H. et al. Extremely efficient flexible organic light-emitting diodes with modified graphene anode. *Nature Photonics* **6**, 105-110 (2012).
- 41 Kabra, D., Lu, L. P., Song, M. H., Snaith, H. J. & Friend, R. H. Efficient Single-Layer Polymer Light-Emitting Diodes. *Advanced Materials* **22**, 3194-3198 (2010).
- 42 Adachi, C., Nagai, K. & Tamoto, N. Molecular design of hole transport materials for obtaining high durability in organic electroluminescent diodes. *Applied Physics Letters* **66**, 2679 (1995).
- 43 Tse, S., Tsang, S. & So, S. Polymeric conducting anode for small organic transporting molecules in dark injection experiments. *Journal of applied physics* **100**, 063708-063708-063705 (2006).
- 44 Cheung, C., Tsung, K., Kwok, K. & So, S. Using thin film transistors to quantify carrier transport properties of amorphous organic semiconductors. *Applied Physics Letters* **93**, 083307-083307-083303 (2008).
- 45 Murgatroyd, P. Theory of space-charge-limited current enhanced by Frenkel effect. *Journal of Physics D: Applied Physics* **3**, 151 (1970).
- 46 Ishii, H., Sugiyama, K., Ito, E. & Seki, K. Energy Level Alignment and Interfacial Electronic Structures at Organic/Metal and Organic/Organic Interfaces. *Advanced Materials* **11**, 605-625 (1999).
- 47 Kahn, A., Koch, N. & Gao, W. Electronic structure and electrical properties of interfaces between metals and π-conjugated molecular films. *Journal of Polymer Science Part B: Polymer Physics* **41**, 2529-2548 (2003).
- 48 Abkowitz, M., Facci, J. & Stolka, M. Behavior of an ideal injecting contact on a trap-free polymer. *Applied Physics Letters* **63**, 1892 (1993).

- 49 Campbell, A. J. *et al.* Transient and steady-state space-charge-limited currents in polyfluorene copolymer diode structures with ohmic hole injecting contacts. *Applied Physics Letters* **76**, 1734 (2000).
- 50 Campbell, I., Smith, D., Neef, C. & Ferraris, J. Consistent time-of-flight mobility measurements and polymer light-emitting diode current–voltage characteristics. *Applied Physics Letters* **74**, 2809 (1999).
- 51 Lampert, M. A. & Mark, P. *Current injection in solids*. (Academic Press, 1970).
- 52 Kao, K. C. & Hwang, W. *Electrical transport in solids: With particular reference to organic semiconductors*. (Pergamon, Oxford, 1981).
- 53 Tsang, S., Tse, S., Tong, K. & So, S. PEDOT: PSS polymeric conducting anode for admittance spectroscopy. *Organic Electronics* **7**, 474-479 (2006).
- 54 Parthasarathy, G., Shen, C., Kahn, A. & Forrest, S. Lithium doping of semiconducting organic charge transport materials. *Journal of applied physics* **89**, 4986-4992 (2001).
- 55 Hsu, C. M. & Wu, W. T. Improved characteristics of organic light-emitting devices by surface modification of nickel-doped indium tin oxide anode. *Applied Physics Letters* **85**, 840-842 (2004).
- 56 Han, S., Yuan, Y. & Lu, Z. H. Highly efficient organic light-emitting diodes with metal/fullerene anode. *Journal of applied physics* **100**, 074504 (2006).
- 57 Hayashi, N., Ishii, H., Ouchi, Y. & Seki, K. Examination of band bending at buckminsterfullerene (C_{60})/metal interfaces by the Kelvin probe method. *Journal of Applied Physics* **92**, 3784 (2002).
- 58 Helander, M., Wang, Z. & Lu, Z. in *Proc. of SPIE*. (ed F. So) 70510Z.
- 59 Kasap, S. O. *Principles of Electronic Materials and Devices*. 3rd edn, (McGraw-Hill, 2006).
- 60 Small, C. E., Tsang, S. W., Kido, J., So, S. K. & So, F. Origin of Enhanced Hole Injection in Inverted Organic Devices with Electron Accepting Interlayer. *Advanced Functional Materials* **22**, 3261-3266 (2012).
- 61 Wienkes, L., Blackwell, C. & Kakalios, J. Electronic transport in doped mixed-phase hydrogenated amorphous/nanocrystalline silicon thin films. *Applied Physics Letters* **100**, 072105 (2012).

- 62 Todorov, T. K. *et al.* Beyond 11% efficiency: Characteristics of state-of-the-art Cu₂ZnSn(S,Se)₄ solar cells. *Advanced Energy Materials*, doi:10.1002/aenm.201200348 (2012).
- 63 Wada, T. *et al.* High-efficiency CIGS solar cells with modified CIGS surface. *Solar Energy Materials and Solar Cells* **67**, 305-310 (2001).
- 64 Ramanathan, K. *et al.* Properties of 19.2% efficiency ZnO/CdS/CuInGaSe₂ thin-film solar cells. *Progress in Photovoltaics: Research and Applications* **11**, 225-230 (2003).
- 65 Forrest, S. Ultrathin organic films grown by organic molecular beam deposition and related techniques. *Chemical Reviews* **97**, 1793 (1997).
- 66 Steinberger, S. *et al.* Vacuum-processed small molecule solar cells based on terminal acceptor-substituted low-band gap oligothiophenes. *Chemical Communications* **47**, 1982-1984 (2011).
- 67 Burroughes, J. *et al.* Light-emitting diodes based on conjugated polymers. *Nature* **347**, 539-541 (1990).
- 68 Drury, C., Mutsaers, C., Hart, C., Matters, M. & de Leeuw, D. Low-cost all-polymer integrated circuits. *Applied Physics Letters* **73**, 108 (1998).
- 69 Hebner, T., Wu, C., Marcy, D., Lu, M. & Sturm, J. Ink-jet printing of doped polymers for organic light emitting devices. *Applied Physics Letters* **72**, 519-521 (1998).
- 70 Braun, D. & Heeger, A. Visible light emission from semiconducting polymer diodes. *Applied Physics Letters* **58**, 1982-1984 (1991).
- 71 Cheng, Y. J., Yang, S. H. & Hsu, C. S. Synthesis of conjugated polymers for organic solar cell applications. *Chemical Reviews* **109**, 5868-5923 (2009).
- 72 Liang, Y. & Yu, L. Development of semiconducting polymers for solar energy harvesting. *Polymer Reviews* **50**, 454-473 (2010).
- 73 Deibel, C. *et al.* Energetics of excited states in the conjugated polymer poly (3-hexylthiophene). *Physical Review B* **81**, 085202 (2010).
- 74 Zhu, X. Y., Yang, Q. & Muntwiler, M. Charge-transfer excitons at organic semiconductor surfaces and interfaces. *Accounts of chemical research* **42**, 1779-1787 (2009).
- 75 Chamberlain, G., Cooney, P. & Dennison, S. Photovoltaic properties of merocyanine solid-state photocells. *Nature* **289**, 45-47 (1981).

- 76 Loutfy, R., Sharp, J., Hsiao, C. & Ho, R. Phthalocyanine organic solar cells: Indium/x-metal free phthalocyanine Schottky barriers. *Journal of applied physics* **52**, 5218 (1981).
- 77 Rajaputra, S., Vallurupalli, S. & Singh, V. P. Copper phthalocyanine based Schottky diode solar cells. *Journal of Materials Science: Materials in Electronics* **18**, 1147-1150 (2007).
- 78 Tang, C. Two-layer organic photovoltaic cell. *Applied Physics Letters* **48**, 183 (1986).
- 79 Yu, G., Gao, J., Hummelen, J., Wudl, F. & Heeger, A. Polymer Photovoltaic Cells: Enhanced Efficiencies via a Network of Internal Donor-Acceptor Heterojunctions. *Science* **270**, 1789-1791 (1995).
- 80 Hiramoto, M., Fujiwara, H. & Yokoyama, M. Three-layered organic solar cell with a photoactive interlayer of codeposited pigments. *Applied Physics Letters* **58**, 1062-1064 (1991).
- 81 Halls, J. *et al.* Efficient Photodiodes from Interpenetrating Polymer Networks. *Nature* **376**, 498-500 (1995).
- 82 He, Z. *et al.* Enhanced power-conversion efficiency in polymer solar cells using an inverted device structure. *Nature Photonics* **6**, 593-597 (2012).
- 83 Günes, S., Neugebauer, H. & Sariciftci, N. S. Conjugated Polymer-Based Organic Solar Cells. *Chemical Reviews* **107**, 1324-1338 (2007).
- 84 Hoppe, H., Sariciftci, N. & Meissner, D. Optical constants of conjugated polymer/fullerene based bulk-heterojunction organic solar cells. *Molecular Crystals and Liquid Crystals* **385**, 113-119 (2002).
- 85 Sze, S. M. & Ng, K. K. *Physics of semiconductor devices*. 3rd edn, (Wiley-interscience, 2006).
- 86 Shrotriya, V. *et al.* Accurate measurement and characterization of organic solar cells. *Advanced Functional Materials* **16**, 2016-2023 (2006).
- 87 ASTM Standard E1021, Standard Test Method for Measuring Spectral Response for Photovoltaic Cells.
- 88 Fitzner, R. *et al.* Interrelation between crystal packing and small-molecule organic solar cell performance. *Advanced Materials* **24**, 675-680 (2012).

- 89 Fitzner, R. *et al.* Dicyanovinyl–substituted oligothiophenes: Structure-property relationships and application in vacuum-processed small molecule organic solar cells. *Advanced Functional Materials* **21**, 897-910 (2011).
- 90 Blouin, N., Michaud, A. & Leclerc, M. A low-bandgap poly (2,7-carbazole) derivative for use in high-performance solar cells. *Advanced Materials* **19**, 2295-2300 (2007).
- 91 Hummelen, J. C. *et al.* Preparation and characterization of fulleroid and methanofullerene derivatives. *The Journal of Organic Chemistry* **60**, 532-538 (1995).
- 92 Li, G., Zhu, R. & Yang, Y. Polymer solar cells. *Nature Photonics* **6**, 153-161 (2012).
- 93 Padinger, F., Rittberger, R. S. & Sariciftci, N. S. Effects of postproduction treatment on plastic solar cells. *Advanced Functional Materials* **13**, 85-88 (2003).
- 94 Ma, W., Yang, C., Gong, X., Lee, K. & Heeger, A. J. Thermally stable, efficient polymer solar cells with nanoscale control of the interpenetrating network morphology. *Advanced Functional Materials* **15**, 1617-1622 (2005).
- 95 Scharber, M. C. *et al.* Design rules for donors in bulk-heterojunction solar cells—Towards 10% energy-conversion efficiency. *Advanced Materials* **18**, 789-794 (2006).
- 96 Havinga, E., Ten Hoeve, W. & Wynberg, H. Alternate donor-acceptor small-band-gap semiconducting polymers; Polysquaraines and polycroconaines. *Synthetic metals* **55**, 299-306 (1993).
- 97 Zhang, Q. T. & Tour, J. M. Low optical bandgap polythiophenes by an alternating donor/acceptor repeat unit strategy. *Journal of the American Chemical Society* **119**, 5065-5066 (1997).
- 98 Peet, J. *et al.* Efficiency enhancement in low-bandgap polymer solar cells by processing with alkane dithiols. *Nature Materials* **6**, 497-500 (2007).
- 99 Liang, Y. *et al.* Development of new semiconducting polymers for high performance solar cells. *Journal of the American Chemical Society* **131**, 56-57 (2008).
- 100 Zhang, Y. *et al.* Conjugated polymers based on C, Si and N-bridged dithiophene and thienopyrroledione units: synthesis, field-effect transistors and bulk heterojunction polymer solar cells. *Journal of Materials Chemistry* **21**, 3895-3902 (2011).

- 101 Amb, C. M. *et al.* Dithienogermole as a fused electron donor in bulk heterojunction solar cells. *Journal of the American Chemical Society* **133**, 10062-10065 (2011).
- 102 Zhu, Y., Xu, X., Zhang, L., Chen, J. & Cao, Y. High efficiency inverted polymeric bulk-heterojunction solar cells with hydrophilic conjugated polymers as cathode interlayer on ITO. *Solar Energy Materials and Solar Cells* **97**, 83-88 (2012).
- 103 He, Z. *et al.* Largely enhanced efficiency with a pfn/al bilayer cathode in high efficiency bulk heterojunction photovoltaic cells with a low bandgap polycarbazole donor. *Advanced Materials* **23**, 3086-3089 (2011).
- 104 Choi, H. *et al.* Combination of titanium oxide and a conjugated polyelectrolyte for high-performance inverted-type organic optoelectronic devices. *Advanced Materials* **23**, 2759-2763 (2011).
- 105 Krebs, F. C. Fabrication and processing of polymer solar cells: a review of printing and coating techniques. *Solar Energy Materials and Solar Cells* **93**, 394-412 (2009).
- 106 Van Mullekom, H., Vekemans, J., Havinga, E. & Meijer, E. Developments in the chemistry and band gap engineering of donor-acceptor substituted conjugated polymers. *Materials science & engineering. R, Reports* **32**, 1-40 (2001).
- 107 Shaheen, S. E., White, M. S., Olson, D. C., Kopidakis, N., Ginley, D. S. *Inverted bulk-heterojunction plastic solar cells*, <<http://spie.org/x14269.xml>> (2007).
- 108 Li, G., Chu, C. W., Shrotriya, V., Huang, J. & Yanga, Y. Efficient inverted polymer solar cells. *Applied Physics Letters* **88**, 253503 (2006).
- 109 Chen, L. M., Hong, Z., Li, G. & Yang, Y. Recent progress in polymer solar cells: manipulation of polymer:fullerene morphology and the formation of efficient inverted polymer solar cells. *Advanced Materials* **21**, 1434-1449 (2009).
- 110 Chen, H. Y. *et al.* Polymer solar cells with enhanced open-circuit voltage and efficiency. *Nature Photonics* **3**, 649-653 (2009).
- 111 Hou, J. *et al.* Synthesis of a low band gap polymer and its application in highly efficient polymer solar cells. *Journal of the American Chemical Society* **131**, 15586-15587 (2009).
- 112 Hou, J., Chen, H. Y., Zhang, S., Li, G. & Yang, Y. Synthesis, characterization, and photovoltaic properties of a low band gap polymer based on silole-containing polythiophenes and 2, 1, 3-benzothiadiazole. *Journal of the American Chemical Society* **130**, 16144-16145 (2008).

- 113 Li, Z. *et al.* Alternating copolymers of cyclopenta [2, 1-b; 3, 4-b'] dithiophene and thieno [3, 4-c] pyrrole-4, 6-dione for high-performance polymer solar cells. *Advanced Functional Materials* **21**, 3331-3336 (2011).
- 114 Krebs, F. C. All solution roll-to-roll processed polymer solar cells free from indium-tin-oxide and vacuum coating steps. *Organic Electronics* **10**, 761-768 (2009).
- 115 Krebs, F. C. Polymer solar cell modules prepared using roll-to-roll methods: knife-over-edge coating, slot-die coating and screen printing. *Solar Energy Materials and Solar Cells* **93**, 465-475 (2009).
- 116 Krebs, F. C., Gevorgyan, S. A. & Alstrup, J. A roll-to-roll process to flexible polymer solar cells: model studies, manufacture and operational stability studies. *Journal of Materials Chemistry* **19**, 5442-5451 (2009).
- 117 Park, S. H. *et al.* Bulk heterojunction solar cells with internal quantum efficiency approaching 100&percnt. *Nature Photonics* **3**, 297-302 (2009).
- 118 Yip, H. L., Hau, S. K., Baek, N. S., Ma, H. & Jen, A. K. Y. Polymer Solar Cells That Use Self-Assembled-Monolayer-Modified ZnO/Metals as Cathodes. *Advanced Materials* **20**, 2376-2382 (2008).
- 119 Beek, W. J. E., Wienk, M. M., Kemerink, M., Yang, X. & Janssen, R. A. J. Hybrid zinc oxide conjugated polymer bulk heterojunction solar cells. *The Journal of Physical Chemistry B* **109**, 9505-9516 (2005).
- 120 Hau, S. K. *et al.* Air-stable inverted flexible polymer solar cells using zinc oxide nanoparticles as an electron selective layer. *Applied Physics Letters* **92**, 253301-253303 (2008).
- 121 Guo, L. *et al.* Highly monodisperse polymer-capped ZnO nanoparticles: Preparation and optical properties. *Applied Physics Letters* **76**, 2901-2903 (2000).
- 122 Mahamuni, S. *et al.* ZnO nanoparticles embedded in polymeric matrices. *Nanostructured materials* **7**, 659-666 (1996).
- 123 Cavalieri, J. J., Skinner, D. E., Colombo Jr, D. P. & Bowman, R. M. Femtosecond study of the size-dependent charge carrier dynamics in ZnO nanocluster solutions. *The Journal of chemical physics* **103**, 5378 (1995).
- 124 Sakohara, S., Ishida, M. & Anderson, M. A. Visible luminescence and surface properties of nanosized ZnO colloids prepared by hydrolyzing zinc acetate. *The Journal of Physical Chemistry B* **102**, 10169-10175 (1998).

- 125 Monticone, S., Tufeu, R. & Kanaev, A. Complex nature of the UV and visible fluorescence of colloidal ZnO nanoparticles. *The Journal of Physical Chemistry B* **102**, 2854-2862 (1998).
- 126 Guo, L. *et al.* Synthesis and characterization of poly (vinylpyrrolidone)-modified zinc oxide nanoparticles. *Chemistry of Materials* **12**, 2268-2274 (2000).
- 127 Du, T. & Illegbusi, O. Synthesis and morphological characterization on PVP/ZnO nano hybrid films. *Journal of materials science* **39**, 6105-6109 (2004).
- 128 Du, T., Song, H. & Illegbusi, O. J. Sol-gel derived ZnO/PVP nanocomposite thin film for superoxide radical sensor. *Materials Science and Engineering: C* **27**, 414-420 (2007).
- 129 Singla, M., Shafeeq M, M. & Kumar, M. Optical characterization of ZnO nanoparticles capped with various surfactants. *Journal of Luminescence* **129**, 434-438 (2009).
- 130 Tang, H. *et al.* Gas sensing behavior of polyvinylpyrrolidone-modified ZnO nanoparticles for trimethylamine. *Sensors and Actuators B: Chemical* **113**, 324-328 (2006).
- 131 Chu, T. Y. *et al.* Bulk heterojunction solar cells using thieno [3, 4-c] pyrrole-4, 6-dione and dithieno [3, 2-b: 2', 3'-d] silole copolymer with a power conversion efficiency of 7.3%. *Journal of the American Chemical Society* **133**, 4250-4253 (2011).
- 132 Subbiah, J., Hartel, M. & So, F. MoO₃/poly (9, 9-diptylfluorene-co-N-[4-(3-methylpropyl)]-diphenylamine) double-interlayer effect on polymer solar cells. *Applied Physics Letters* **96**, 063303 (2010).
- 133 Subbiah, J. *et al.* Combined effects of MoO₃ interlayer and PC₇₀BM on polymer photovoltaic device performance. *Organic Electronics* **11**, 955-958 (2010).
- 134 Kim, D. Y. *et al.* The effect of molybdenum oxide interlayer on organic photovoltaic cells. *Applied Physics Letters* **95**, 093304-093304-093303 (2009).
- 135 Ding, H., Gao, Y., Kim, D. Y., Subbiah, J. & So, F. Energy level evolution of molybdenum trioxide interlayer between indium tin oxide and organic semiconductor. *Applied Physics Letters* **96**, 073304-073304-073303 (2010).
- 136 Meyer, J., Khalandovsky, R., Görrn, P. & Kahn, A. MoO₃ films spin-coated from a nanoparticle suspension for efficient hole-injection in organic electronics. *Advanced Materials* **23**, 70-73 (2011).

- 137 Sun, Y., Seo, J. H., Takacs, C. J., Seifter, J. & Heeger, A. J. Inverted polymer solar cells integrated with a low-temperature-annealed sol-gel-derived ZnO film as an electron transport layer. *Advanced Materials* **23**, 1679-1683 (2011).
- 138 Zhang, Y. *et al.* X-ray photoelectron spectroscopy study of ZnO films grown by metal-organic chemical vapor deposition. *Journal of crystal growth* **252**, 180-183 (2003).
- 139 Lilliedal, M. R., Medford, A. J., Madsen, M. V., Norrman, K. & Krebs, F. C. The effect of post-processing treatments on inflection points in current–voltage curves of roll-to-roll processed polymer photovoltaics. *Solar Energy Materials and Solar Cells* **94**, 2018-2031 (2010).
- 140 Aliaga, C. *et al.* Sum frequency generation and catalytic reaction studies of the removal of organic capping agents from Pt nanoparticles by UV-ozone treatment. *The Journal of Physical Chemistry C* **113**, 6150-6155 (2009).
- 141 Park, J. Y., Aliaga, C., Renzas, J. R., Lee, H. & Somorjai, G. A. The role of organic capping layers of platinum nanoparticles in catalytic activity of co oxidation. *Catalysis letters* **129**, 1-6 (2009).
- 142 Small, C. E. *et al.* High-efficiency inverted dithienogermmole-thienopyrrolodione-based polymer solar cells. *Nature Photonics* **6**, 115-120 (2012).
- 143 Hoth, C. N., Choulis, S. A., Schilinsky, P. & Brabec, C. J. High photovoltaic performance of inkjet printed polymer: fullerene blends. *Advanced Materials* **19**, 3973-3978 (2007).
- 144 Chen, S. *et al.* Inverted polymer solar cells with reduced interface recombination. *Advanced Energy Materials* **2**, 1333-1337 (2012).
- 145 Krebs, F. C. Roll-to-roll fabrication of monolithic large-area polymer solar cells free from indium-tin-oxide. *Solar Energy Materials and Solar Cells* **93**, 1636-1641 (2009).
- 146 Kim, J. Y. *et al.* Efficient tandem polymer solar cells fabricated by all-solution processing. *Science* **317**, 222-225 (2007).
- 147 Chen, S. *et al.* Photo-carrier recombination in polymer solar cells based on P3HT and silole-based copolymer. *Advanced Energy Materials* **1**, 963-969 (2011).
- 148 Moulé, A. J., Bonekamp, J. B. & Meerholz, K. The effect of active layer thickness and composition on the performance of bulk-heterojunction solar cells. *Journal of applied physics* **100**, 094503 (2006).

- 149 Mihailetti, V. D. *et al.* Origin of the enhanced performance in poly (3-hexylthiophene):[6, 6]-phenyl c-butyric acid methyl ester solar cells upon slow drying of the active layer. *Applied Physics Letters* **89**, 012107 (2006).
- 150 Lenes, M., Koster, L., Mihailetti, V. & Blom, P. Thickness dependence of the efficiency of polymer:fullerene bulk heterojunction solar cells. *Applied Physics Letters* **88**, 243502 (2006).
- 151 Shrotriya, V., Yao, Y., Li, G. & Yang, Y. Effect of self-organization in polymer/fullerene bulk heterojunctions on solar cell performance. *Applied Physics Letters* **89**, 063505 (2006).
- 152 Li, G. *et al.* "Solvent Annealing" effect in polymer solar cells based on poly (3-hexylthiophene) and methanofullerenes. *Advanced Functional Materials* **17**, 1636-1644 (2007).
- 153 Thompson, B. C. & Fréchet, J. M. J. Polymer–fullerene composite solar cells. *Angewandte chemie international edition* **47**, 58-77 (2007).
- 154 Blom, P. W. M., Mihailetti, V. D., Koster, L. J. A. & Markov, D. E. Device physics of polymer:fullerene bulk heterojunction solar cells. *Advanced Materials* **19**, 1551-1566 (2007).
- 155 Lee, J. K. *et al.* Processing additives for improved efficiency from bulk heterojunction solar cells. *Journal of the American Chemical Society* **130**, 3619-3623 (2008).
- 156 Moon, J. S., Jo, J. & Heeger, A. J. Nanomorphology of PCDTBT:PC₇₀BM Bulk Heterojunction Solar Cells. *Advanced Energy Materials* **2**, 304-308 (2012).
- 157 Mihailetti, V., Wildeman, J. & Blom, P. Space-charge limited photocurrent. *Physical review letters* **94**, 126602 (2005).
- 158 Mühlbacher, D. *et al.* High photovoltaic performance of a low-bandgap polymer. *Advanced Materials* **18**, 2884-2889 (2006).
- 159 Hoppe, H., Arnold, N., Sariciftci, N. & Meissner, D. Modeling the optical absorption within conjugated polymer/fullerene-based bulk-heterojunction organic solar cells. *Solar Energy Materials and Solar Cells* **80**, 105-113 (2003).
- 160 Goodman, A. M. & Rose, A. Double extraction of uniformly generated electron-hole pairs from insulators with noninjecting contacts. *Journal of applied physics* **42**, 2823 (1971).

- 161 Liu, L. & Li, G. Investigation of recombination loss in organic solar cells by simulating intensity-dependent current–voltage measurements. *Solar Energy Materials and Solar Cells* **95**, 2557-2563 (2011).
- 162 Street, R., Schoendorf, M., Roy, A. & Lee, J. Interface state recombination in organic solar cells. *Physical Review B* **81**, 205307 (2010).
- 163 Choudhury, K. R. *et al.* Understanding the performance and loss-mechanisms in donor–acceptor polymer based solar cells: Photocurrent generation, charge separation and carrier transport. *Solar Energy Materials and Solar Cells* **95**, 2502-2510 (2011).
- 164 Lenes, M., Morana, M., Brabec, C. J. & Blom, P. W. M. Recombination-limited photocurrents in low bandgap polymer/fullerene solar cells. *Advanced Functional Materials* **19**, 1106-1111 (2009).
- 165 Sokel, R. & Hughes, R. Numerical analysis of transient photoconductivity in insulators. *Journal of applied physics* **53**, 7414 (1982).
- 166 Law, M. *et al.* Determining the internal quantum efficiency of PbSe nanocrystal solar cells with the aid of an optical model. *Nano letters* **8**, 3904-3910 (2008).

BIOGRAPHICAL SKETCH

Cephas Small was born in 1979 in Brooklyn, NY as the youngest of four, with two older sisters and an older brother. He grew up in Uniondale, NY, a small suburban town on Long Island. Throughout elementary school, junior high school and high school, Cephas was heavily involved in activities involving creativity, self-expression, and problem solving, such as music, math & science clubs, and sports. His first love was music, learning to play various styles of music on the saxophone and participating in music competitions. After graduation from high school, he received a music scholarship from Northeastern University, where he majored in chemical engineering based on the advice of his favorite math teacher in high school.

At Northeastern University, Cephas pursued his academic interests, continued playing the saxophone as part of his scholarship requirements, and served as a student leader with the National Society of Black Engineers (NSBE) on the chapter and regional levels. As he approached graduation, his mentors encouraged him to pursue graduate school since he excelled in coursework involving hands-on design work. At the same time, through his involvements with NSBE, he met research faculty at Norfolk State University and he was encouraged to apply to the university's graduate program. Cephas was accepted to the historic black college and began his master's degree thesis work after graduating from Northeastern.

At Norfolk State University, he learned how to conduct research under the tutelage of Dr. Mikhail Noginov at the university's Center for Materials Research. During his time at Norfolk State, Cephas realized that he wanted to conduct device-related research for his doctorate studies since the majority of his research work at that time was focused on materials characterization. After receiving his Master of Science, he joined the Materials

Science and Engineering Department at the University of Florida in the fall of 2006. He was granted the opportunity to work with Professor Franky So in his Organic Electronic Materials and Devices Laboratory. There, he learned the operating principles for various organic electronic and optoelectronic devices. Under the direction of Dr. Franky So, he conducted high-impact research work in the area of organic electronics.

Cephas received his doctorate in the fall of 2012. He intends to continue his research work on the development of novel material and device design for organic electronics.